Conformations of isolated macromolecules in solution and on the surface.

David Shirvanyants

A dissertation submitted to the faculty of the University of North Carolina at Chapel Hill in partial fulfillment of the requirements for the degree of Doctor of Philosophy in the Department of Chemistry.

Chapel Hill

2007

Approved by:

Professor Sergei Sheiko

Professor Michael Rubinstein

Professor Garegin A. Papoian

Professor Lee G. Pedersen

Professor Edward T. Samulski

Abstract

David Shirvanyants

Conformations and dynamics of macromolecules in solution and on the surface.

(Under the direction of Sergei Sheiko and Michael Rubinstein)

This dissertation studies different aspects of conformational properties of polymers. Two specific topics include (i) the deviations of single macromolecule conformations in the θ-solution from the classical description, and (ii) conformations, order and flow of molecular brushes on solid surfaces.

In solution we studied the deviations of single macromolecule conformations at the θ-conditions from the predictions of classical theories. The previously unknown long range correlations in the conformations of linear polymers in a θ-solvent were found using analytical calculations and molecular dynamics simulations. Long range power law decay of the bond vector correlation function $\langle \cos\phi \rangle \sim s^{-3/2}$ dominate the standard exponential decay $\langle \cos\phi \rangle = e^{-s/l_p}$, where ϕ is the angle between the two bonds, s is their separation along the chain contour and l_p is the persistence length. These long-range correlations lead to significant deviations of polymer size from ideal with mean square end-to-end distance $\langle R^2 \rangle - b^2 N \sim \sqrt{N}$, where N is the number of Kuhn segments of size b. These findings are explained by a fine interplay of polymer connectivity and the non-zero range of monomer interactions. Moreover, this effect is not specific for dilute θ-solutions and exists in semidilute solutions and melts of polymers. Our theory is in good agreement with the experimental data on Flory characteristic ratio, as well as with results of computer simulations.

On surfaces, brush-like macromolecules were visualized by the atomic force microscopy (AFM). In order to quantitatively analyze conformations of visualized molecules we developed the corresponding algorithms and software. This software enables detection of the molecular contour, measurement of molecule size, area, orientational and nematic order parameters, etc. In addition, the automated procedure of molecular detection reduced the time and improved the quality of analysis of image series. Using our method we have studied the molecular weight and polydispersity of linear and multi-arm molecular brushes, the spontaneous curvature of grafted molecules, which is caused by competition of conformational entropy of side chains and elasticity of backbone, behavior of brushes in a matrix of linear polymer, the effect of structure of multi-armed brushes on their 2d orientational order, the dynamics and conformational transitions of individual molecules in the precursor layer of spreading droplet, the spontaneous scission of grafted molecules with long side-chains.

To my parents, Grigory and Lusik, who are the reason for my existence,

and to my friend Valeria, for her optimism and cheering me up.

Table of Contents

List of Figures

List of Tables

Chapter 1

Introduction

Polymers are versatile materials, often encountered in our daily life and widely used in construction, packaging, coating and many other branches of industry. Most applications of polymers depend on their physical properties, which in turn depend on the chemical composition, molecular structure, and on the spatial arrangement of the repeating units, that is on polymer conformations. Polymer conformations determine viscosity of solutions and melts, interfacial behavior, and electro-optical properties. Polymer conformation is one of the most fundamental and long studied subjects in polymer physics [1, 2]. It is well known that conformations of a polymer are determined by the intrachain monomer interactions, as was first described by Paul Flory [2, 3]. Depending on the monomer chemical structure, type of solvent, and temperature, monomers attract or repel each other. In the good solvent, repulsive forces dominate, resulting in swelling of polymer chains. The opposite case of mostly attractive interactions corresponds to the poor solvent, where polymer chains collapse into globules. In the intermediate state, the repulsive and attractive interactions compensate each other leading to effectively unperturbed conformations. These special type of polymer solutions are called θ-solutions. The latter are often used in polymer science as a reference point, when reporting relative change of polymer size with changing temperature and solvent quality, and when comparing size changes in dif-

ferent polymers. Despite the fundamental and practical significance of the θ-point, behavior of a polymer in a θ-solution is still poorly understood.

Following the analogy with theory of gases one may assume that because of compensation of attractive and repulsive parts of monomer interactions, a polymer in a θ-solution behaves as if there were no interactions at all, that is, as an *ideal* polymer. Even though this is not correct, conformations of a polymer in a θ-soluton are often described as *quasi-ideal*, that is the state where the conformation of a real polymer can be treated as ideal for all practical purposes. In Chapter 2, we show that this classical approach results in inaccurate predictions of polymer size and structure, because it neglects the effect of polymer connectivity on monomer interactions. Polymer connectivity induces the long range correlations along the chain, which are completely absent from the ideal chain as well as from the classical descriptions of polymer in the θ-state. Thus, we demonstrate that the ideal chain can not be used to model polymers in θ-solvents. We have found that the mean square size of the chain in a θ-solvent has a large correction $\sim \sqrt{N}$ to the linear term.

If monomers were not connected, the compensation of their interactions would lead to an ideal solution of monomers. But, monomers are connected and we have proven that their connectivity causes the qualitatively different behavior of polymers in θ-solutions.

Another type of polymer system, where conformation plays an important role includes polymers on a surface. The behavior of adsorbed polymers poses many challenges for analytical and numerical studies as compared to bulk systems. Theories for polymers in two-dimensional space do not work well because of the complicated nature of monomer surface interactions and specific arrangement of monomeric units. Computer simulations are often complicated by the need to explicitly introduce the atomic surface and the slower equilibration process induced by strong confinement of macromolecules. Applications of standard experimental techniques, such as X-ray scattering, or ellipsometry are also limited because of small amount of material in the layer. However, the surface allows the direct visualization of indi-

vidual molecules, which is hardly possible in the bulk. It is therefore reasonable to address the analysis of visualized macromolecules on a surface obtained by means of scanning probe microscopy.

An outstanding method for studies on the nanometer scale is the Atomic Force Microscopy (AFM). It can be used for visualization of surface morphology, probing physical properties, and maskless nanolithography. Visualization by AFM is the most significant area of applications due to its high spatial resolution, which for soft polymers ranges over 1-10 nm. In this range of length scales, materials are full of intriguing electronic, magnetic, and optical properties promising new advances in lithography, data storage, photonics, and molecular electronics. Furthermore, the imaging conditions do not require any sample modification or special environment such as those needed for electron microscopy. As such, native structures can be visualized in their natural medium, which is especially vital in biology. Not only is AFM effective at small length scales, it is also able to visualize larger structures such as crystallites, micelles, and blends making it possible to establish direct correlations between the molecular structure and macroscopic properties. Along with visualization of static structures, AFM is able to monitor various processes such as crystallization and conformational transitions enabling studies of dynamic properties of polymeric materials.

The microscopic images provide excellent visual representations of nanometer sized objects. However, microscopic images need to be analysed in a consistent manner for the following statistical analysis, classification and comparison. This visual form of experimental results necessitates the development of a digital image analyses methods suitable for microscopic images. Chapter 3 describes the newly developed method of automated image analysis and presents its application for studies of various properties of polymers on surfaces. We have investigated individual properties such as molecular weight, length, flexibility and mobility, as well as collective properties, such as translational and orientational order parameters, mixing behavior, etc. The additional challenges include detection and characterization of individual

molecules, accounting for the image discreteness and low resolution, and multiple image analysis for polymer dynamics studies.

We have used molecular brushes as a convenient model polymers that have well controlled length and stiffness to produce clear images upon visualization. The new method of image analysis has then been applied to molecular brushes.

The developed software was first applied to characterize molecular dimensions. Thus we have measured the length of macromolecules and their number density on the surface, and by knowing the mass concentration we have been able to accurately estimate the molecular weight.

The ability to measure molecular dimensions was applied to analyze the extension of the classical Flory theory of mixing to planar melts. Using our method we have studied the binary mixtures of molecular brushes and linear polymers. We have found that swelling of molecular brushes in the melt of linear chains can be described by an equivalent linear chain made of N_A/N monomers, where N_A is the backbone degree of polymerization, and N is the side chain degree of polymerization. A generalized Flory theory of mixing has been suggested, based on the analysis of our observations.

The next step in our studies of polymers on the surface was the analysis of more complex systems of multiarm molecular brushes. For these systems we have calculated the polydispersity and studied the ordering on the surface. We have found that multiarm molecular brushes undergo the sharp conformational transition from an extended to compact state. This transition narrows the molecular size distribution and induces orientational order.

A most unusual and stunning phenomena was observed during the adsorption of molecular brushes with very long side chains. It turns out that the adsorption of side chains can induce tension in the backbone, strong enough to break the covalent bonds. The backbone scission occurs spontaneously upon the adsorption. We demonstrate that the tension is equally distibuted along the backbone, excluding short end segments, and it depends on the length of side chains

and on the strength of adsorption, characterized by the surface tension.

It is also very interesting to observe the dynamic behavior of molecular brushes. We have watched the molecular motion in the precursor layer of the droplet spreading on graphite, and measured the coefficients of polymer diffusion relative to the surface and to the precursor film. Comparing these coefficients we have discovered that the main mechanism of mass transport in the precursor layer is the molecular motion induced by the plug flow of the polymer, and that the contribution of thermally driven diffusion is minor.

Spreading on a highly oriented graphite surface introduces another interesting effect. Our study demonstrates that molecular brushes form long-range ordered structures, aligning themselves along the preferential directions. The spreading induced flow significantly improves ordering, by far exceeding the effect of random thermal motion. The stability of these ordered structures is supported by the epitaxial adsorption of a large number of side chains.

Chapter 2

Long range correlations in a polymer chain due to its connectivity

2.1 Introduction

Polymer chains can have different conformations depending of the interaction between their monomers. If interactions are predominately repulsive, as in the case of good solvent solutions, polymers swell, while if their interactions are attractive, as in the case of poor solvent, chains are collapsed. Between these two cases there is a special condition, called θ-point, in which the average pairwise interaction between monomers is zero and the chain is almost ideal. Similar compensation of attractive and repulsive parts of monomeric interactions occurs in polymer melts and concentrated solutions. In semidilute solutions the pairwise interactions vanish on length scales larger then the correlation length ξ due to the screening of excluded volume by surrounding chains. Polymers without pairwise interactions, as in θ-solvent and melts, are traditionally described by the ideal chain model [3–14].

In an ideal chain there are no interactions between monomers that are far apart along the chain. Interactions of monomers close to each other along the chain (due to chain stiffness or

local steric hindrance) lead to exponentially decaying correlations in directions of vectors $\mathbf{a}_i$ and $\mathbf{a}_j$ of bonds i and j separated by the distance $s = a|i-j|$ along the chain

$$h(s) = \frac{1}{a^2}\left\langle \mathbf{a}_i \mathbf{a}_j \right\rangle \sim e^{-s/l_p} \tag{2.1}$$

where l_p is the persistence length and a is the bond length. Rapid decay of bond vector correlations leads to the random walk statistics of the chain on length scales larger than the persistence segment length l_p. The concept of the persistence length is widely used for characterization of the polymer flexibility [15–19]. Single stranded DNA ($l_p \approx 2nm$) is an example of a flexible chain, and double strained DNA ($l_p \approx 50nm$) is a common example of a semiflexible polymer.

The assumption of ideality of chains in melts and concentrated solutions was recently demonstrated to be incorrect [20]. Using both computer simulations and theoretical estimates it was shown that bond vector correlation function (Eq (2.1)) in melts and semidilute solutions decays as a power law

$$h(s) \sim s^{-3/2}, \tag{2.2}$$

This unexpectedly slow decay of correlations was explained by the effect of correlation hole [21], which leads to relative compression of the chain with respect to its ideal state.

Notice, that the correlation hole effect is the prominent feature of the melt or concentrated solution of polymer chains and is absent for chains in θ-solutions. Since the interaction between monomers at θ-point is compensated by their interaction with molecules of the solvent, one can naively expect to observe ideal-like behavior of such chains. In this chapter we demonstrate that polymers in θ-solvents are not ideal and exhibit the same power law decay of the bond correlation function (Eq (2.2)). We will show that the ideal behavior is destroyed due to chain connectivity even for zero net interactions between monomers that are far away from each other along the chain. Such monomers do interact when they approach each other in space, but it is usually assumed that attractive and repulsive parts of the interaction compensate each

other leading to zero effective second virial coefficient. The main result of this chapter is that connectivity of chain monomers leads to additional correlations in their relative position in space causing additional interaction between these monomers as compared to the case of unconnected monomers. In the latter case the effect of hard core is canceled by attractive well at the compensation point. The connectivity of monomers in the chain results in a slight shift of the probability of the two monomers to be within the range of the attractive well of the interaction potential. The magnitude of this shift depends on the distance between the two monomers along the chain contour. This probability shift leads to a nonzero effective interaction of two monomers belonging to the same chain.

Another manifestation of the new effect is the large correction term $\sim \sqrt{N}$ to the expected in θ-solvent linear dependence of the mean square polymer chain size R^2 on its degree of polymerization N. This change of polymer size can be observed experimentally by measuring the rate of approach of the Flory characteristic ratio C_n to its limiting value C_∞ with increasing molecular weight M.

We will show that this new effective connectivity-induced interaction results in the power law decay of the bond vector correlation function for all quasi-ideal chains, including polymers in θ-solvents, melts and concentrated solutions. This effect was not taken into account in classical polymer models. It does not exist in models where chain elasticity is balanced by the excluded volume interactions of unconnected monomers, as in Flory theory. The effect of long-range correlations is also absent in the model with δ-function interaction potential that neglects the spatial separation of attractive and repulsive parts of monomeric interactions. Thus there are two necessary conditions for the existence of the new effect, described in the present chapter: monomer connectivity along the chain and nonzero range of interaction potential. Our analysis provides unified description of non-ideality of θ-solutions, melts and semidilute solutions at distances larger than correlation length. In the present chapter we focus on the change in monomeric interactions caused by entropic elasticity of the loop between the two

monomers in contact. This effect leads to corrections of chain size and induces long range correlations of chain segment orientations.

It is well known that conformations of a polymer chain at a θ-point are not ideal [13, 14, 22, 23]. The earlier studies discussed the renormalization of pairwise monomeric interactions caused by three (and higher) body contacts. It can be shown [14] that this short-range renormalization leads to the shift of the effective θ-temperature relative to the Flory's θ-temperature of the "gas of monomers". The corrections to the polymer size at the new shifted θ-temperature renormalize the effective Kuhn length. The next order non-linear corrections [14] are on the order of $\sim y/(1+y\log N)$, where y is proportional to the third virial coefficient [14]. The bond vector correlation function due to this correction $\sim \frac{\log^2 N}{N^2(1+y\log N)^2}$ decays faster and is therefore less important than our new prediction $\sim N^{-3/2}$ due to connectivity-induced correlations. The logarithmic correction to the chain size decays slower than our connectivity-induced correction $\sim N^{-1/2}$ and therefore may dominate for very long chains.

In the following sections we discuss the origin and the consequences of the new long range correlations phenomena. Sections 2.2.1–2.2.4 discuss the case of flexible chains $b \approx a$, where b is the Kuhn segment, and a is the bond length. In section 2.2.1 we start with the simpler model of of a telechelic chain, where two interacting monomers connected by the ideal chain. Then, in section 2.2.2 we extend the obtained results to the case of real chains, all monomers of which interact with each other. In section 2.2.3 we discuss the change of the effective intrachain monomeric interactions due to the chain connectivity. In section 2.2.4 we compare the new analytical predictions with the results of our computer simulations. In section 2.2.5 we further generalize our theory to the case of semiflexible chains with Kuhn length $b \gg a$. Section 2.2.6 summarizes our analysis of the long range correlations in polymer due to the chain connectivity. In section 2.3 we calculate the new molecular weight dependence of the Flory characteristic ratio. In section 2.4 we study the polymer swelling ratio as a function of temperature and solvent quality. In section 2.5 we summarize our analysis of the new connectivity effect and

long range correlations in polymers.

2.2 Bond vector correlation function

2.2.1 Telechelic model

In the ideal chain model there are no long range correlations in orientation of polymer segments. Such correlations appear as a result of interactions between chain monomers. In order to study the effect of interactions on the chain segment orientations we first consider the telechelic chain model consisting of a Gaussian chain of N Kuhn monomers, with only two end monomers interacting with each other via a short-range potential $U(r)$, depending only on the distance between these monomers (the end-to-end vector $\mathbf{r}$ of the chain)

$$\mathbf{r} = \sum_{i=1}^{N} \mathbf{a}_i. \tag{2.3}$$

Here $\mathbf{a}_i$ are bond vectors with average length a equal to its Kuhn length $a = b$. This model will be generalized in section 2.2.2 in order to take into account interaction of all monomers of the real chain.

In the simplified telechelic chain model the correlation function $h_L(s)$ of the two bond vectors i and j

$$h_L(s) = \frac{1}{a^2} \left\langle \mathbf{a}(s_i)\mathbf{a}(s_j) \right\rangle \tag{2.4}$$

does not depend on their positions s_i and s_j along the chain contour ($h_L(s) = h_L$), nor on the distance along the chain $s = a|i-j|$ between them, since the probability of chain conformation depends only on the sum of all bond vectors $\mathbf{a}(s_i)$, that is on the end-to-end vector, Eq (2.3). We calculate the correlation function h_L in two steps:

First, we average the scalar product $\mathbf{a}(s_i)\mathbf{a}(s_j)$ over all fluctuations of bond vectors for given

end-to-end vector **r** (see Appendix 2.A for details)

$$H_L(r) = \frac{1}{a^2}\,\langle \mathbf{a}(s_i)\mathbf{a}(s_j)\rangle\big|_r = \frac{r^2 - bL}{L^2}. \tag{2.5}$$

where L is the chain contour length and b is the Kuhn length. According to this expression the two bond vectors are not correlated only when r is equal to the root-mean-square end-to-end distance of this chain, bL. They have opposite preferential orientation (with $H_L(r) < 0$) if the chain is compressed, $r^2 < bL$, and the same orientation (along the end-to-end vector **r**, with $H_L(r) > 0$) for stretched chain, $r^2 > bL$.

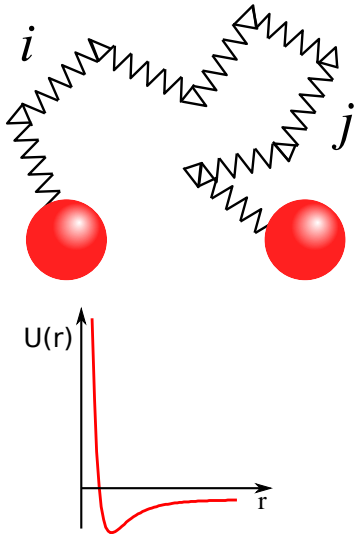

Figure 2.1: Telechelic chain model

Second, we average the result, $H_L(r)$ (see Eq (2.5)), over different end-to-end distances r with the monomer contact probability distribution to obtain h_L Eq (2.4) (see Appendix 2.B)

$$h_L = \frac{1}{a^2}\langle \mathbf{a}_i \mathbf{a}_j \rangle = \left(\frac{3}{2\pi}\right)^{3/2} \left(\frac{B}{b^{1/2}L^{5/2}} + \frac{5}{2}\frac{A}{b^{3/2}L^{7/2}} + \cdots \right), \tag{2.6}$$

where B is the second virial coefficient

$$B = -\int f(r) d^3 r, \tag{2.7}$$

the coefficient A is

$$A = \int f(r)\, r^2 d^3 r. \tag{2.8}$$

and $f(r)$ is the Mayer f-function:

$$f(r) = e^{-U(r)/k_B T} - 1. \tag{2.9}$$

Note that, as expected, the bond vector correlation function does not depend on location of the bond vectors along this telechelic chain nor on their separation s along the chain (number of bonds between them), but only depends on the contour length L between two interacting monomers of the chain.

In classical models of polymers [10] the bond vector correlation function h_L includes only the second virial coefficient B term:

$$h_L = \left(\frac{3}{2\pi}\right)^{3/2} \frac{B}{b^{1/2}L^{5/2}}, \tag{2.10}$$

Therefore, classical theories predict the absence of the long range correlations of polymer segments orientations in θ-solution.

The most important conclusion from this simple model of telechelic chain is that at the θ-point (with zero second virial coefficient $B = 0$) the correlation between bond vectors decays as a power of the curvilinear distance L along the polymer contour between two interacting monomers $\langle \mathbf{a}(s_i)\mathbf{a}(s_j)\rangle \sim AL^{-7/2}$ in the telechelic chain.

2.2.2 Polymer with all interacting monomers

A more realistic description of a polymer is a chain, with all $N+1$ monomers interacting with each other. The bond vector correlation function $h(i,j) = \frac{1}{a^2}\langle \mathbf{a}(s_i)\mathbf{a}(s_j)\rangle$ of two bonds, separated by the distance $s = a\,|i-j|$ along the chain can be found by taking the sum of contributions of all loops formed by pairs n and m of interacting monomers with $s_n < s_i < s_j < s_m$ which contain bond vectors $\mathbf{a}(s_i)$ and $\mathbf{a}(s_j)$:

$$h(i,j) = \sum_{n<i} \sum_{m>j, i<j} h_{m-n}, \qquad n < i < j < m \leq N = L/b \tag{2.11}$$

Substituting the function H_L from Eq (2.6) and replacing the summation in Eq (2.11) by the integration, we obtain

$$h(i,j) \simeq \left(\frac{3}{2\pi}\right)^{3/2} \left[Bg_{1/2}(i,j) + \frac{5}{2} Ag_{3/2}(i,j) + \cdots \right], \tag{2.12}$$

where

$$g_k(i,j) \equiv \int_0^{s_i} ds_n \int_{s_j}^{L} \frac{1}{b^k (s_m - s_n)^{k+2}} ds_m = \frac{1}{k(k+1)b^k} \left[\frac{1}{(s_j - s_i)^k} - \frac{1}{s_j^k} - \frac{1}{(L-s_i)^k} + \frac{1}{L^k} \right]. \tag{2.13}$$

We see, that the bond vector correlations decay as a power law of the distance $s = |s_j - s_i| = a|j-i|$ along the chain between bonds i and j. For internal bonds (that is, when $1 \ll i < j \ll N$) of a sufficiently long chain ($N \gg 1$) at θ-condition ($B = 0$), we find power law decay of the correlation function with the exponent $k = 3/2$

$$h(i,j) = \frac{1}{a^2}\langle \mathbf{a}_i \mathbf{a}_j \rangle = h(s) \sim s^{-3/2} \qquad (\theta\text{-solvent}) \tag{2.14a}$$

(as long as $A \neq 0$). If one of these bonds is at the chain end ($s_i - \varepsilon = 0$) we have

$$h(0,j) = \frac{1}{a^2}\langle \mathbf{a}(0)\mathbf{a}(s_j) \rangle \sim (s_j - \varepsilon)^{-3/2} - s_j^{-3/2} \sim s_j^{-5/2} \qquad (\text{end monomer, } \theta\text{-solvent}). \tag{2.14b}$$

If both bonds are at the opposite chain ends we recover the result of the previous subsection $h(0,L) = \frac{1}{a^2}\langle \mathbf{a}(0)\mathbf{a}(L) \rangle \sim L^{-7/2}$. In good solvent ($B > 0$) the bond vector correlation function decays with exponent $k = 1/2$

$$h(s) \sim s^{-1/2} \qquad (\text{good solvent}). \tag{2.14c}$$

Notice, that expansion coefficients B and A in Eq (2.12) depend on the shape of interaction potential. Although it is possible to design the special potential $U(r)$ in order to have $B = A = 0$, the higher order term would still be non-zero leading to power law decay with a higher exponent.

2.2.3 Connectivity induced modification of monomeric interactions

An alternative way of deriving the bond vector correlation function $h(s)$ for a polymer in a good solvent is from the mean square distance between monomers i and j

$$\langle r^2 \rangle = a^2 \left\langle \sum_{k,l=i}^{j} \mathbf{a}_k \mathbf{a}_l \right\rangle = \sum_{k,l=i}^{j} h\left(b|i-j|\right) \simeq 2 \int_{ia}^{ja} ds_1 \int_0^{s_1} h\left(s_1 - s_2\right) ds_2, \tag{2.15}$$

Summation over bond vectors k and l was replaced by integration over chain contour coordinates s_1 and s_2 in the last part of Eq (2.15). Taking two derivatives of the mean square end-to-end vector (Eq (2.15)) with respect to contour length between monomers $s = a|i-j|$, we find

$$h\left(s\right) \simeq 2 \frac{d^2 \langle r^2 \rangle}{ds^2}. \tag{2.16}$$

The size of a polymer in the vicinity of the θ-point is given by the expression [10, 24, 25]

$$\langle r^2 \rangle = bs \left(1 + \frac{4}{3} \frac{s^{1/2}}{b^{1/2}} \frac{B}{b^3} + \ldots \right) \tag{2.17}$$

where b is the Kuhn monomer size. For simplicity assume it equal to bond length for flexible chains ($b = a$). We will consider semiflexible chains with $b > a$ in section 2.2.5. Substituting expression (2.17) into Eq. (2.16) we get the bond vector correlation function

$$h\left(s\right) \simeq \frac{B}{b^{5/2}} \frac{1}{s^{1/2}}. \tag{2.18}$$

in agreement with the results of the previous subsection (Eq (2.14c)). Thus, no long range correlations are expected at the θ-point ($B = 0$), according to the classical approach.

In order to study correlations at the θ-conditions one should take into account that in addition to the direct monomeric interactions, described by the potential $U(r)$, there are indirect elastic interactions that propagate along the chain. The total effective interaction potential of two monomers separated by the distance r is $U_{tot}(r) = U(r) + U_s(r)$, where $U_s(r)$ is the spring-like potential due to the chain section between these monomers

$$U_s(r) = \frac{3k_BT}{2sb}r^2. \tag{2.19}$$

Mayer f-function reflects the difference between statistical weights (Boltzmann factors) of states with interactions and without them ($U(r) = 0$). Since the $U_s(r)$ is the only effective potential between monomers at large distances r, when $U(r) = 0$, the effective Mayer function of these monomers connected into a chain is

$$f_s(r) = e^{-U_{tot}(r)/k_BT} - e^{-U_s(r)/k_BT} \tag{2.20}$$

Substituting this equation into Eq (2.7) we find the effective virial coefficient $B(s)$, which depends on the separation s of the interacting monomers along the chain contour. At large $s \gg b$ one can expand this function in powers of $1/s$

$$\begin{aligned} B(s) &= -\int f_s(r)d^3r \simeq -\int \left(1 - \frac{3r^2}{2sb} + \cdots\right)\left(e^{-U(r)/k_BT} - 1\right)d^3r = \\ &= -\int \left(e^{-U(r)/k_BT} - 1\right)d^3r + \frac{3}{2sb}\int r^2\left(e^{-U(r)/k_BT} - 1\right)d^3r = \\ &= -\int f(r)d^3r + \frac{3}{2sb}\int r^2 f(r)d^3r = B + \frac{3A}{2sb} + \cdots \end{aligned} \tag{2.21}$$

where Mayer f-function $f(r)$ of unconnected monomers is defined in Eq (2.9), the second virial coefficient B is given by Eq (2.7), and the coefficient A is defined in Eq (2.8). Eq (2.21) was

derived assuming that chain is flexible ($l_p \lesssim a$). A more general case of semiflexible chains with persistence length $l_p \gtrsim a$ will be discussed in Section 2.2.5. Although $B = 0$ in the θ-solvent, the effective second virial coefficient $B(s)$ does not vanish at the θ-condition. Substituting this expression into Eq (2.10), and summing contributions from all pairs of monomers (see Eq (2.11)) we get*

$$h(s) \simeq \frac{B}{b^{5/2}} \frac{1}{s^{1/2}} + \frac{3}{2} \frac{A}{b^{7/2}} \frac{1}{s^{3/2}}. \tag{2.22}$$

which is equivalent to Eq (2.12) for $0 \ll s_i < s_j \ll L$.

Note, that here we consider only the two-body interactions, as the effect under study is stronger than the contribution of multibody interactions. Also, note that since $B(s)$ depends on the separation s between monomers, it vanishes at different temperatures for different s. In general it is impossible to suppress the long range correlations (that is to have both $B = 0$ and $A = 0$), except in certain special cases as described in Appendix 2.C.

2.2.4 Computer simulations

To test our analytical predictions by computer simulations we employ the coarse-grained continuum bead-spring model of polymer chains. A polymer in this model consists of $N+1$ soft-sphere monomers, interacting with each other via the truncated and shifted Lennard-Jones (LJ) potential

$$U_{LJ}(r) = \begin{cases} 4\varepsilon \left[\left(\frac{\sigma}{r}\right)^{12} - \left(\frac{\sigma}{r}\right)^{6} \right] - 4\varepsilon \left[\left(\frac{\sigma}{r_c}\right)^{12} - \left(\frac{\sigma}{r_c}\right)^{6} \right] & r < r_c \\ 0 & r > r_c \end{cases} \tag{2.23}$$

*Note, that the effective $B(s)$ can not be substituted for B in Eq (2.17). In order to obtain the correct polymer size $\langle r^2 \rangle$ one needs to substitute the $h(s)$ from Eq (2.22) into Eq (2.16) and perform another summation over all pairs of monomers.

where r is the distance between monomers and r_c is the cutoff radius (we use $r_c = 2.5\sigma$ for all simulations). Chain connectivity is modeled by the finitely extensible nonlinear elastic (FENE) interaction potential between adjacent monomers (in addition to the LJ potential)

$$U_{FENE}(r) = -\frac{1}{2} k_{FENE} R_0^2 \ln\left[1 - \frac{r^2}{\sigma^2 R_0^2}\right] \tag{2.24}$$

where k_{FENE} is the spring constant and R_0 is the maximum extension of the bond, at which the interaction energy becomes infinite. In this work we choose $R_0 = 2\sigma$ and $k_{FENE} = 10\varepsilon/\sigma^2$, which minimizes the N-dependence of the θ-temperature [26]. New conformations are generated using the standard method of constant temperature (NVT ensemble) molecular dynamics. Initial configurations were created as random self-avoiding walks, and then equilibrated for at least 10 τ_R, where τ_R is the longest relaxation time, determined from the decay of the chain end-to-end distance autocorrelation function.

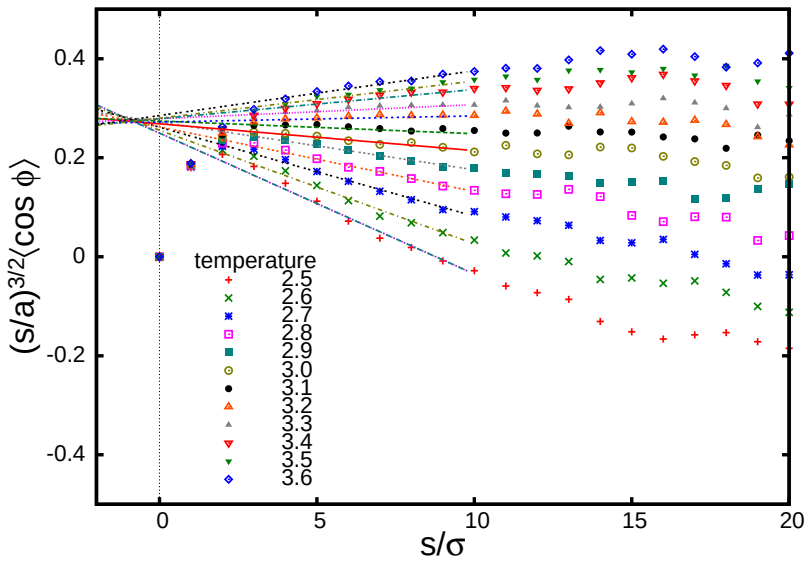

Figure 2.2: Bond vector correlations of a polymer chain at different temperatures. Lines are linear fits for the initial linear segments of the plots. Temperature is given in the units of $k_B T/\varepsilon$.

In fig. 2.2 we present the bond vector correlation function

$$\langle \cos\phi \rangle = \frac{1}{a^2} \langle \mathbf{a}(s_i)\mathbf{a}(s_{i+n}) \rangle = \frac{1}{N-n} \sum_{i=1}^{N-n} h(i, i+n) \tag{2.25}$$

averaged over all pairs of monomers separated by segments of length s and multiplied by the number of monomers, s/a, between the two bonds to the power $3/2$. The average in Eq (2.25) is dominated by the internal chain sections with $h(i,j) \approx B|s_j - s_i|^{-1/2} b^{-5/2} + \frac{5}{2} A|s_j - s_i|^{-3/2} b^{-7/2}$, therefore we expect that $(s/a)^{3/2} \langle \cos\phi \rangle \sim \frac{5}{2} A + Bsb$ should have linear dependence on the curvilinear distance s between two bonds. The temperature dependence of $A(T)$ can be represented* as $A(T) = A(\theta) - s_0 b B(T)$ with a numerical constant $|s_0/a| \sim 1$. This gives

$$\left(\frac{s}{a}\right)^{3/2} \langle \cos\phi \rangle \sim A(\theta) + B(T)\,(s - s_0)\,b \tag{2.26}$$

Fitting the linear sections of the $(s/a)^{3/2} \langle \cos\phi \rangle$ curves we notice that lines for different temperatures cross at one point with $s_0/a \simeq -0.86$, as expected from our analysis.

2.2.5 Semiflexible chains

In this section we will discuss the long-range correlation effect in semiflexible chains with persistence length l_p larger than bond length $a \lesssim l_p \ll L$. So far we considered flexible polymers with $l_p \lesssim a$ and Gaussian probability of contact between all pairs of monomers. However, the probability of monomeric contacts for semiflexible chains with $l_p \gtrsim 1$ is strongly reduced at monomeric separations shorter than $\sim 5 l_p$ [27–29]. The reduction of contact probability suppresses the effect of the long-range correlations, and short chain segments behave as elastic rods with exponential decay of correlations (Eq (2.1)). To account for this fact we need to include the small s contact probability in the effective Mayer f-function of connected monomers

*Note that within the first-order approximation both B and A are linear in $1/T$ when $T \gg 0$.

Eq (2.20):

$$f_p(r,s) = \zeta(s,r) f(r,s), \tag{2.27}$$

where $\zeta(s,r)$ describes the deviation of contact probability between i and j monomers from the Gaussian approximation. The asymptotic limits of $\zeta(s,r=0)$ are evidently $\lim_{s\to 0}\zeta(s) = 0$ and $\lim_{s\to\infty}\zeta(s) = 1$. For small $r/s \to 0$ we can expand the new monomer contact probability function and expect that $h(s) \approx \zeta(s)h_0(s)$, where $h_0(s)$ denotes the bond vector correlation function of flexible chains, as given by Eq (2.22).

The complete bond-vector correlation function for semiflexible chains can be represented as the sum of short-range and long-range contributions:

$$\langle \cos\phi(s) \rangle = e^{-s/l_p} + c_\phi \zeta(s) h_0(s) \tag{2.28}$$

where c_ϕ is the normalization coefficient.

The approximate form of the "stiffness function" $\zeta(s)$ can be obtained by considering the formation of a loop in a semiflexible chain of length s. The bending energy in this case is [30]

$$E(s) = k_B T \frac{l_p}{2} \int_0^s \kappa(s')^2 ds'. \tag{2.29}$$

where $\kappa(s)$ is the curvature (inverse of the radius of the circle that describes the bend).

In order to test our idea about the nature of the crossover (Eq (2.28)) from exponential to power law decay of the bond vector correlation function, we define $\zeta(s)$ as the Boltzmann weight of the loop of length s:

$$\zeta(s) = \exp\left(-\frac{E(s)}{k_B T}\right) = \exp\left(-\frac{k_l l_p}{s}\right) \tag{2.30}$$

where k_l is the numerical constant to be found from our simulation results*.

*The function $\zeta(s)$ is expected to have an l_p-dependent prefactor. However, as the analytical form of this

The chain stiffness in our simulations is introduced through the bending potential

$$U(\phi) = u_\phi(1-\cos\phi) \tag{2.31}$$

where ϕ is the angle between the neighboring bonds i and $i+1$, and u_ϕ is the stiffness of the bending potential. The persistence length of such chains depends on u_ϕ and for large $u_\phi \gg k_BT$ becomes proportional to it: $\lim_{u_\phi\to\infty} l_p = \sigma u_\phi/k_BT$.

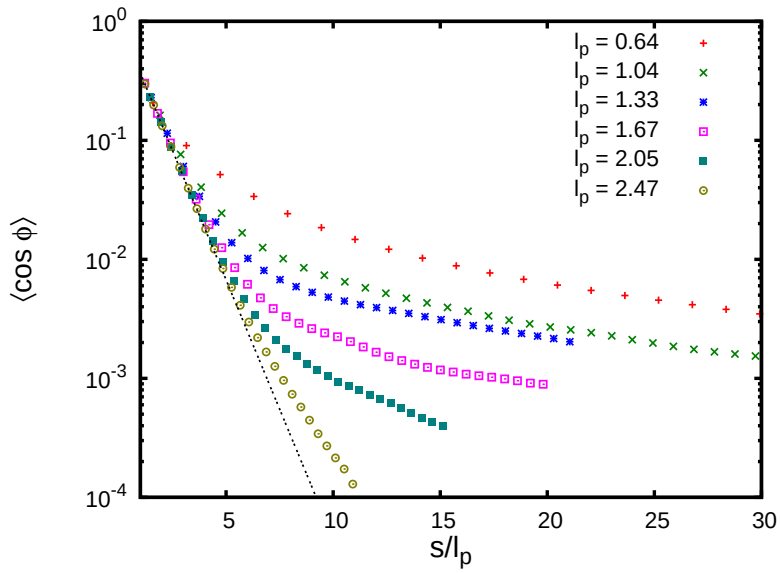

Figure 2.3: Bond vector correlation function of polymer chains with different stiffness. Points represent the simulation results for $N = 199$ and $T = 3.1\varepsilon/k_B$. Horizontal axis is scaled by the corresponding persistence length l_p, dotted line shows the exponential function e^{-s/l_p}.

The magnitude of the long-range correlation effect decays with increasing stiffness. This can be explained by the decrease of the probability to form a loop between the interacting monomers. The growing value of the persistence length l_p leads to an overall decrease of polymer concentration c^* inside the volume $\langle r^2\rangle^{3/2} \sim (sl_p)^{3/2}$ occupied by the segment of length s, and the probability of pair contacts decays correspondingly $c^* \sim \frac{d^3}{\langle R^2\rangle^{3/2}} \sim \frac{d^3}{(sl_p)^{3/2}}$.

prefactor is unknown, we assume that it can be absorbed into the definition of k_l. We did not succeed to fit our data using the theoretical predictions for loop closure probability published in the review [29] and in the works cited therein, possibly because of the relatively small l_p in our simulations.

The magnitude of the long-range correlations effect is proportional to the probability of contact between the two monomers (estimated as the ratio of the monomer interaction volume d^3 to the pervaded volume of the segment $(sl_p)^{3/2}$).

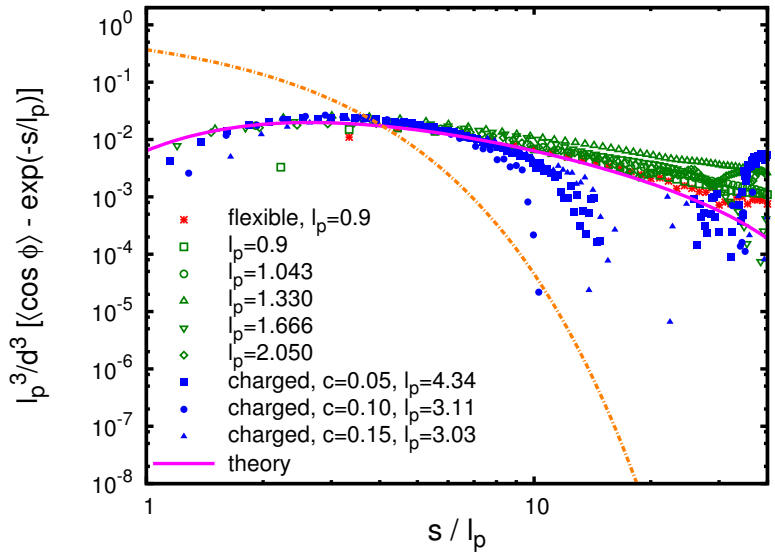

Figure 2.4: The residual non-exponential decay of the bond vector correlation function. The dashed and solid lines mark the exponential and non-exponential components of the bond vector correlation function (the first and the second terms in Eq (2.28)), respectively. The coefficients $c_\phi \cdot A = 1.84 \pm 0.04$ and $k_l = 4.3 \pm 0.07$ were determined by fitting simulation data to theoretical prediction Eq (2.32). Persistence length l_p is given in units of σ, and concentration is units of σ^{-3}.

Fig. 2.3 shows the decay of the bond vector correlation function for semiflexible chains with different l_p. The coefficient of the Lennard-Jones potential (Eq (2.23)) was set to $\varepsilon = k_BT/3.1$, because from the linear fits in Fig.2.2 we have found that the effective second virial coefficient is the smallest $|B| \approx 0$ for $\varepsilon = k_BT/3.1$ (the solid line in Fig.2.2 corresponding to $\varepsilon = k_BT/3.1$ has the smallest slope). The persistence length l_p was determined from the exponentially decaying section of the $\langle\cos\phi(s)\rangle$ at $a \leq s \leq l_p$. Using these values of l_p we extract the long-range component of the $\langle\cos\phi(s)\rangle$ and plot it using the reduced coordinate axes in Fig. 2.4. The horizontal axis is scaled by persistence length l_p, and vertical axis is scaled by l_p^3/d^3. The rescaling of the vertical axis reflects the expected dependence of the

monomer contact probability on the persistence length $d^3/(sl_p)^{3/2} = (d/l_p)^3(l_p/s)^{3/2}$. Thus for a given value of s/l_p the factor $(l_p/d)^3$ is expected to collapse the data. For the short-ranged LJ potential the interaction radius is about the size of the monomer $d/\sigma \sim 1$. The extracted exponential decay component of the $\langle\cos\phi\rangle(s)$ is shown in (Fig. 2.4) by the dashed line e^{-s/l_p}, and the theoretical expectation for the long-range decay Eq (2.28)

$$h(s) - \exp(s/l_p) = c_\phi \zeta(s) h_0(s) = c_\phi e^{-\frac{k_l l_p}{s}} \left(\frac{3}{2\pi}\right)^{3/2} \cdot \frac{5}{2} \frac{A}{b^{7/2} s^{3/2}} \tag{2.32}$$

is shown by the solid line. The coefficients obtained by fitting the numerical data are $c_\phi \cdot A = 1.84 \pm 0.04$ and $k_l = 4.3 \pm 0.07$. The data for the flexible chain are shown on the same plot for the guidance purposes, to illustrate the universal nature of the long-range correlations in polymers. Since the regular definition of the persistence length (see Eq (2.1)) is inapplicable for flexible chains, the numerical data were scaled using the empirical value of $l_p = 0.9\sigma$ required to collapse them with the results for the semiflexible chains.

The long range intramolecular correlations in a dilute solution of charged polymers are the natural consequence of the long range electrostatic interactions. In semidilute polyelectrolyte solutions these interactions are screened by charges of neighboring chains and by counterions. To compare the behavior of charged polymers with our previous findings we discuss the coarse-grained model, in which the semidilute polyelectrolyte solution is considered as the melt of chains, consisting of correlation volumes (blobs). Each such blob of size $\xi \approx f^{-1/3} b^{-1/3} c^{-1/2} l_B^{-1/6}$ is neutral and consists of $g \approx f^{-1} b^{-1} l_B^{-1/2} c^{-1/2}$ monomers [31, 32] (where f is the fraction of charged monomers, l_B is the Bjerrum length and solvent is θ-like for uncharged backbone). The chain inside the correlation volume is a stretched array of electrostatic blobs. Charged polymers in semidilute solutions become flexible only at the scales larger than correlation length ξ, and have the persistence length of order of correlation length $l_p \sim \xi$ [16].

The results of the molecular dynamics simulation* for the bond vector correlation function of polyelectrolytes chains in semidilute solutions are shown in Fig. 2.4 with solid symbols. This function also exhibits long-range correlation. The corresponding curves can be collapsed with our results for neutral semiflexible chains by associating the range d of interactions with correlation length ξ leading to the scaling factor $l_p^3/d^3 \approx l_p^3/\xi^3$. For the solutions of concentrations $c = 0.05\sigma^{-3}$, $0.10\sigma^{-3}$ and $0.15\sigma^{-3}$ we have found the values of the cube of the ratio of persistence length to correlation length l_p^3/ξ^3 to be 1.1 ± 0.1, 1.2 ± 0.1 and 1.3 ± 0.1, correspondingly. The ratio l_p^3/ξ^3 increases with concentration, which is in agreement with the predictions made in ref. [16].

Significant deviation from the exponential decay of the bond vector correlation function begins at monomer separations of $s \approx 4 \div 5 l_p$, as can be seen in the Fig. 2.4. The magnitude of the correlations falls as $\sim 0.01 l_p^3$ at this crossover point. This decreasing magnitude of the effect makes observations of the non-exponential decay of the bond vector correlation function in polymers with large persistence length, such as polyelectrolytes increasingly more difficult.

2.2.6 Bond correlation function: Summary

In order to emphasize the two ingredients necessary for the power law decay of the bond-vector correlations let us examine another approach that includes monomer connectivity, such as the perturbation theory [11, 25], based on the Edwards model of polymer chain [4]. Although Edwards model includes monomer connectivity, the interactions between monomers are approximated by the δ-function † potential [4, 7, 10]

$$f(r) = -B\delta(\mathbf{r}). \tag{2.33}$$

*Details of this simulation are given in Ref. [33]

†Here $\delta(\mathbf{r})$ is the 3-d Dirac δ-function, $\delta(\mathbf{r}) = \frac{\delta(r)}{4\pi r^2}$

Due to the zero-range of the δ–function potential, the effect of connectivity on the monomer interactions vanishes ($A = \int r^2 f(r) d^3 r = 0$) and $B(s) = B$ (Eq (2.21)).

In order to account for the long-range renormalization of the monomeric interactions and thus correctly describe the macromolecular conformation, a polymer model has to meet two conditions. (i) The model must consider the fact that monomeric units are connected. (ii) The model must take into account the finite (non-zero) range $d > 0$ of the monomeric interactions.

Note that the Flory class of polymer models violates the first condition (ignores the monomer connectivity), while the Edwards class of models violates the second condition (finite range of interactions) and therefore both predict no long-range bond-vector correlations at the θ-point.

2.3 Polymer size

Polymer chain at the θ-condition is usually used as the reference state in the analysis of polymer conformations [34–41]. The dependence of the mean square end-to-end distance of the polymer at the θ-temperature on the number n of bonds in it is described by the characteristic Flory ratio

$$C_n = \frac{R^2}{l_0^2 n} \tag{2.34}$$

where $l_0^2 n$ is the end-to-end distance of the corresponding freely-jointed chain [42]. The ideal chain model predicts that the characteristic ratio quickly approaches its asymptotic value C_∞ with increasing n as $C_\infty - C_n \sim n^{-1}$ [2, 43]. Long range correlations in the polymer chain described in the present chapter lead to much weaker dependence, $C_\infty - C_n \sim n^{-1/2} \sim N^{-1/2}$, where N is number of Kuhn segments of length b.

The polymer size in a θ-solution can be found from Eqs (2.15) and (2.22):

$$R_\theta^2(N) = b^2 N - \frac{3}{2} b^{-5} A \sqrt{N} \tag{2.35}$$

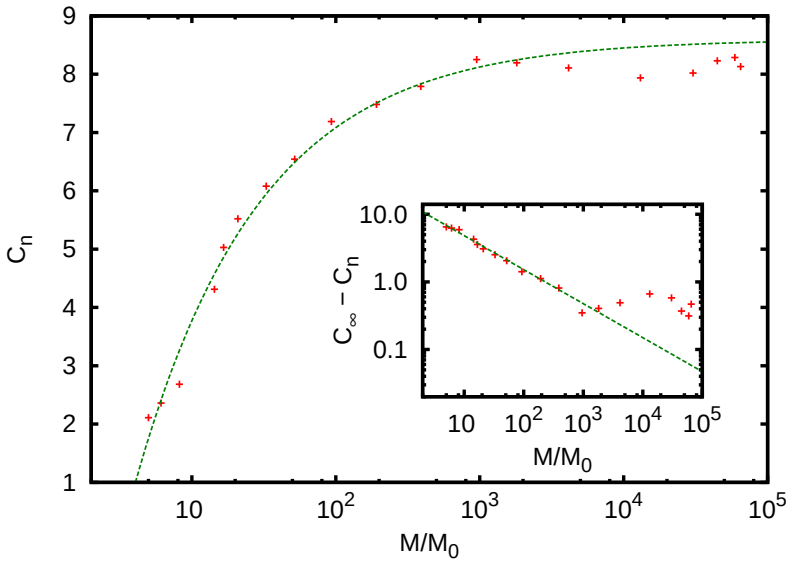

Figure 2.5: Flory characteristic ratio for polystyrene in cyclohexane at 34.5°C (θ-solution) [44]. For polystyrene the monomer length $l_0 \approx 1.54$Å and its mass per bond is $M_0 = 52 g/mol$.

where $L = Nb$. Similar $\sim \sqrt{N}$ deviation from the ideal scaling $R_g^2(N) \sim N$ is derived in Appendix 2.D from the bond vector correlation function.

The characteristic Flory ratio, C_n, of a linear chain can be expressed in terms of a mean square radius of gyration of a polymer at the θ-point:

$$C_n = \frac{6R_g^2}{l_0^2 (M/M_0)} \tag{2.36}$$

where M_0 is the molar mass per bond. From Eq (2.35) we obtain the expression for the characteristic ratio which is a linear function of $N^{-1/2} \sim M^{-1/2}$, where C_∞ is defined as $C_\infty = \lim_{n\to\infty} C_n$

$$C_\infty - C_n \sim \frac{3}{2}\frac{A}{b^5\sqrt{N}} \tag{2.37}$$

The comparison of our prediction of the molecular weight dependence of the characteristic Flory ratio C_n with experimental data for polystyrene in a θ-solution [44] is shown in Fig. 2.5. The characteristic ratio increases with the degree of polymerization and saturates for large

molecules. To analyze the rate of this saturation we plot the difference of C_n from the limiting value C_∞. The log-log plot of this difference is presented in the inset in Fig. 2.5. The least-square fit of the data to the power law gives $C_\infty - C_n = (32.0 \pm 2.2)(M/M_0)^{-0.54\pm0.03}$. The measured exponent is in excellent agreement with the value of $-1/2$ predicted by our theory confirming the validity of Eq (2.35). Similar $N^{-1/2}$ dependence has been also obtained in Ref. [22] for the inner chain segments using the self-consistent mean-field approach.

2.4 Swelling ratio

Excluded volume interactions between monomers lead to either swelling or collapse of polymer chains relative to their ideal states [10,24]. For the classical models of a polymer chain with N Kuhn segments of length b the equation for the mean square swelling ratio $\alpha^2 = 6R_g^2/Nb^2$ can be written as

$$\alpha^2 = c_0 + \frac{c_1 z}{\alpha^3} + \frac{C}{\alpha^6} \tag{2.38}$$

where interaction parameter z is defined [10] as $z = \left(\frac{3}{2\pi b^2}\right)^{3/2} N^{1/2} B$.

Dimensionless coefficients c_0 and c_1 are model-specific and C is proportional to the third virial coefficient (renormalized by the 4-th and higher order virial coefficients).

Swelling factor in Eq (2.38) is defined relative to the size of the ideal chain. Since this size is not known neither experimentally nor numerically, we define the swelling ratio β relative to the θ-state, that is the state with $z = 0$:

$$\beta = R_g/R_g^\theta = \alpha/\alpha_\theta, \tag{2.39}$$

where α_θ is defined by equation (2.38) with $B = 0$:

$$\alpha_\theta^2 = c_0 + \frac{C}{\alpha_\theta^6} \tag{2.40}$$

The interaction parameter z depends on the intramolecular second virial coefficient B. We will use the known temperature dependence [8] of this coefficient to analyze the computer simulation results and redefine the interaction parameter as

$$z = c_2 \tau N^{1/2} b^3 \tag{2.41}$$

where c_2 is the numerical coefficient and the reduced temperature τ is defined as

$$\tau = \begin{cases} (T - T_\theta)/T_\theta & \text{at} \qquad T < T_\theta \\ (T - T_\theta)/T & \text{at} \qquad T > T_\theta \end{cases} \tag{2.42}$$

Here we use different expressions for τ depending upon whether the temperature is above or below the θ-temperature $T_\theta \approx 3.1$. The reason for this choice is that τ may be thought of as a normalized interaction parameter which varies from -1 in poor solvent conditions ($T \to 0$), through 0 at $T = T_\theta$ where the chain is neither swollen nor collapsed ($\beta = 1$), to 1 in good solvent conditions ($T \to \infty$). Eq (2.42) guaranties that the limiting behavior of τ is achieved while not changing the form of τ at temperatures close to T_θ.

To obtain the explicit form of $z(\beta)$ we subtract Eq (2.38) from (2.40) to exclude c_0 and then substitute $\alpha = \alpha_\theta \beta$ from Eq (2.39):

$$z = A_1 \beta^5 - (A_1 - A_3)\, \beta^3 - A_3 \beta^{-3} \tag{2.43}$$

This equation depends on two dimensionless coefficients, $A_1 = \alpha_\theta^5 / c_1$ and $A_3 = C / \left(c_1 \alpha_\theta^3\right)$. The best fit of the simulated swelling data is shown in fig. 2.6 is shown by the open circles with $A_1 = 9.02$ and $A_3 = 0.46$.

The fit by classical equation (Eq (2.43)) deviates significantly in the region of moderately poor solvent, at $|z| \lesssim 1$. These deviations are related to the fact that classical theories do not

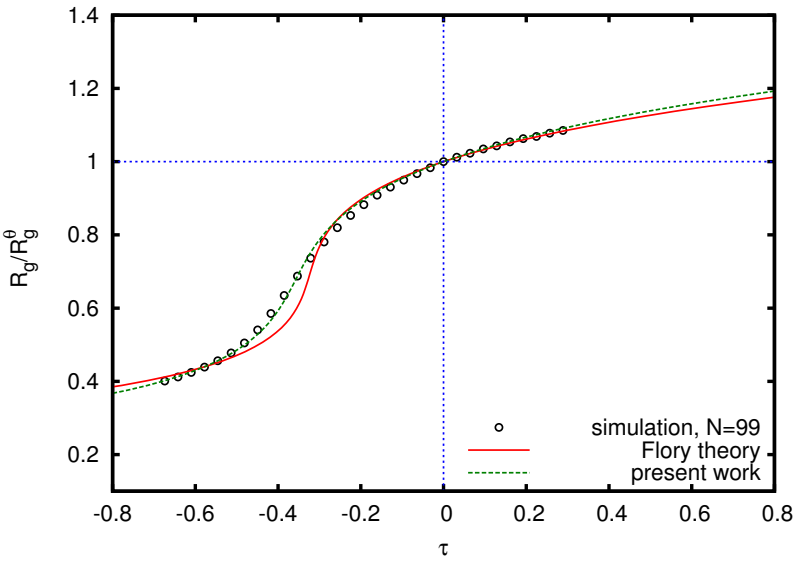

Figure 2.6: Swelling ratio of simulated polymer chain consisting of 100 monomers. Lines show the best fit of simulation data by Eq (2.43) (solid line) and Eq (2.45) (dashed line).

account for the effect of monomer connectivity on the monomeric interactions, being based on assumptions either of mean-field model of cloud of unconnected monomers or of the Edwards model of infinitely thin chain with $d/b \to 0$. The ratio d/b is not negligibly small for real chains. The thickness for most flexible hydrocarbon polymers is comparable to the Kuhn segment length, $d/b \sim 0.2 \div 0.3$. Connectivity of monomers with finite interaction range d into a chain leads to a new term A'/α^4 in addition to three terms in Eq (2.43) (as shown in Appendix 2.E)

$$\alpha^2 = c_0 + \frac{c_1 z}{\alpha^3} + \frac{A'}{\alpha^4} + \frac{C}{\alpha^6}. \tag{2.44}$$

The corresponding expression for fitting the simulation data can be obtained similarly to Eq (2.43)

$$z = A_1\beta^5 - (A_1 - A_2 - A_3)\,\beta^3 + A_2\beta^{-1} - A_3\beta^{-3} \tag{2.45}$$

where $A_2 = \frac{A'}{c_1}\alpha_\theta$. The best fit of numerical data to this equation is shown in Fig. 2.6 (dashed line) with $A_1 = 7.27$, $A_2 = 0.85$ and $A_3 = 0.30$. As can be seen from the comparison of the

curves in fig.2.6, the additional term (A'/α^4) in Eq (2.44) is important in moderately poor solvents, and gives only weak corrections in the asymptotic regimes at $|z| \gg 1$.

2.5 Conclusions

We have analyzed the conformations of linear macromolecules in θ-solution and shown that they are non-universal. Chain size and correlation of chain segments on all scales up to the size of the whole chain depend on the details of the intermonomeric potential. We have shown that polymer at θ-point does not have ideal-like conformation and is characterized by the long-range correlations. Correlation of chain segment orientations $\langle \mathbf{a}_i \mathbf{a}_j \rangle$ decay as power law, except for semiflexible polymers, in which case power law decay can be masked by the initial exponential decay on length scales smaller than the length of several persistence segments. The deviations of the dependence of mean square chain size on the polymerization degree from the ideal law $R^2(N) - b^2 N \sim \sqrt{N}$ are much larger than N^{-1} correction predicted by the classical theories. We explain this non-universal behavior by the effect of monomer connectivity and non-zero range of interactions. Classical description of the θ-state of a polymer chain can be recovered in the limit of point-type monomeric interactions (characterized by the delta-function form of the Mayer f-function $f(r) = k_B T B \delta(r)$).

The similar long-range correlations have been observed in the polymer melt [20] and explained by the effective compression of polymer coils due to the correlation hole effect. However, this argument ignores the fact that this compression-inducing *intermolecular* interactions are compensated by the *intramolecular* interactions, that would otherwise swell the macromolecule. We believe, that the origin of the observed power law correlations in polymer melt is the same as in the θ-solution, i.e. the shift of the monomeric Mayer f-function due to the finite interaction range and chain connectivity. The case of melts is additionally complicated in comparison to the θ-solution by the presence of non-zero second virial coefficient [21]

$B(s) \sim s^{-1}$. This two-body interaction alone can introduce the long range correlations with a $s^{-3/2}$ dependence, similar to the connectivity effect (see Eq (2.22)), but with an opposite sign. The two effects may partially cancel or screen each other, depending on the magnitude of the coefficients B and A, determined by the chemical structure of monomers.

2.6 Acknowledgments

We would like to acknowledge financial support of National Science Foundation under grants CHE-0616925 and CTS-0609087, National Institutes of Health under grant 1-R01-HL0775486A and NASA under agreement NCC-1-02037.

2.A Bond vector correlations for fixed end-to-end vector

Consider a flexible chain with N bonds of average bond length a equal to Kuhn length b and with fixed end-to-end vector $\mathbf{r}$. The bond vector correlation function $H_L(r)$ for fixed r can be found by averaging the square of both sides of Eq. (2.3) over the fluctuations of bond vectors $\{\mathbf{a}_i\}$:

$$r^2 = N\left\langle \mathbf{a}_i^2 \right\rangle + N(N-1)\, a^2 H_L(r) \tag{2.46}$$

In the case of a Gaussian chain the mean square length of the bond,

$$\left\langle \mathbf{a}_i^2 \right\rangle = \left\langle \mathbf{a}_i \right\rangle^2 + \left\langle \delta\mathbf{a}_i^2 \right\rangle, \tag{2.47}$$

depends on the length of the end-to-end vector $\mathbf{r}$ and may differ from a^2 when chain is extended or compressed relative to its mean square size b^2N. The average $\langle \mathbf{a}_i \rangle$ can be found by averaging Eq (2.3) over the fluctuations of bond vectors $\mathbf{a}_i$ for a given $\mathbf{r}$:

$$\langle \mathbf{a}_i \rangle = \mathbf{r}/N. \tag{2.48}$$

In contrast to the average, $\langle \mathbf{a}_i \rangle$, the amplitude of fluctuations of the bond vector $\delta\mathbf{a}_i = \mathbf{a}_i - \langle \mathbf{a}_i \rangle$ of Gaussian chain does not depend on $\mathbf{r}$.

Fixing the chain ends at a constant distance decreases the number of degrees of freedom of this chain from N to $N-1$ and thus reduces the average bond fluctuations by the factor of $(N-1)/N$:

$$\left\langle \delta\mathbf{a}_i^2 \right\rangle = \frac{N-1}{N} a^2 \tag{2.49}$$

Substituting Eqs (2.49) and (2.48) in (2.47), we find from Eq (2.46) the final expression (Eq (2.5)) for the bond vector correlation function $\langle \mathbf{a}_i \mathbf{a}_j \rangle$.

2.B Average bond vector correlation function of telechelic chain

To calculate bond vector correlation function h_L we average $H_L(r)$ (Eq (2.5)) over all end-to-end distances r with the probability $\mathcal{P}(r)$ of chain conformation with a given end-to-end distance r:

$$H_L \equiv \int \mathcal{P}(r) H_L(r) d^3r = \frac{\int H_L(r) Q_N(r) f(r) d^3r}{1 + \int Q_N(r) f(r) d^3r}. \tag{2.50}$$

where

$$\mathcal{P}(r) = \frac{Q_N(r) e^{-U(r)/k_BT}}{\int Q_N(r') e^{-U(r')/k_BT} d^3r'}, \tag{2.51}$$

and $f(r)$ is the Mayer f-function (Eq (2.9)). Here $Q_N(r)$ is the probability distribution to find ends of Gaussian chain at a given distance r from each other

$$Q_N(r) = \left(\frac{3}{2\pi bL}\right)^{3/2} \exp\left(-\frac{3r^2}{2bL}\right), \tag{2.52}$$

$e^{-U(r)/T}$ is the corresponding Boltzmann weight, b is the Kuhn length and L is the contour length of the polymer.

Since $f(r)$ vanishes at large r the main contribution to this function comes from loop conformations with chain ends spatially close to each other $r \ll b^2 N$. Expanding the functions $Q_N(r)$ (2.52) in Eq (2.50) in powers of $1/N$ we obtain Eq (2.6).

2.C Ideal-like chains

In the section 2.2.2 we have shown the existence of the long-range correlations in polymer chains at the θ-point ($B = 0$). A natural question is, whether there are cases in which such correlations vanish and the macromolecule behaves as an ideal chain. As follows from Eq (2.22) the bond vector correlation function $H(i, j)$ vanishes when all coefficients in Eq (2.12) are equal to zero. We begin by attempting to construct a monomeric interaction potential with vanishing first two moments of Mayer f-function

$$B \sim \int f(r) d^3 r = 0 \qquad \text{and} \qquad A \sim \int r^2 f(r) d^3 r = 0 \tag{2.53}$$

The following potential with Lennard-Jones like asymptotic behavior ($U_i(r) \sim r^{-6}$ at $r \to \infty$) satisfies these conditions (2.53):

$$U_i(r) = K_B T \log \left[1 + \varepsilon \frac{\sigma^6 (5\sigma^4 - 10\sigma^2 r^2 + r^4)}{(\sigma^2 + r^2)^5} \right] \tag{2.54}$$

with positive constants ε and σ. Potential U_i (Eq (2.54)) has a minimum at r_0 ($U_i(r_0) < 0$), similarly to the Lennard-Jones potential U_{LJ}, but it also has a maximum at $r_1 > r_0$ ($U_i(r_1) > 0$). Without this second maximum all higher moments of $f(r)$ would be greater than B. The presence of a maximum is a necessary but not sufficient condition, yet this reasoning gives us certain insight on how to design a potential of an "ideal" chain*. Evidently, in order to

*The true ideal chain has no interactions at all, of course. This is why we put "ideal" in quotation for a chain with interactions, but with no long range bond vector correlations.

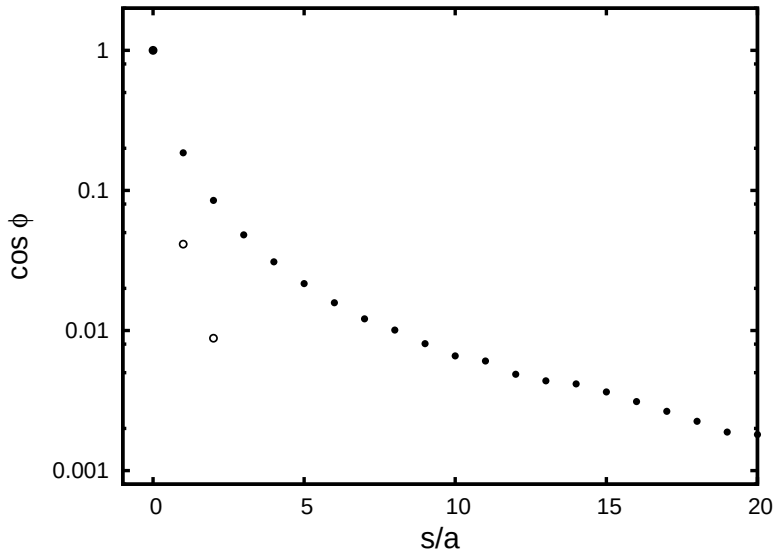

Figure 2.7: Bond vector correlation function of simulated polymer chain with monomers interacting via LJ potential (Eq (2.23), solid circles) and via special quasi-ideal potential (Eq (2.54), open circles).

prepare an "ideal" chain with $h(i,j) = 0$ the potential $U(r)$ has to be a damped oscillatory function.

We have used potential $U_i(r)$ (Eq (2.54)) instead of the regular Lennard-Jones potential to simulate polymer chains of length $N = 99$ as described in section 2.2.4. In Fig. 2.7 we compare the two bond vector correlation functions obtained from the computer simulation of polymer chains with monomers interacting via (I) regular LJ-potential (Eq (2.23), solid circles), and (II) special quasi-ideal chain potential (Eq (2.54), open circles). In the second case correlations decay much faster, in accordance with Eqs (2.53) and (2.12). We expect that correlation decay in this case is dominated by the first non-zero term $\sim s^{-6}$, but to confirm this dependence a longer simulation is required because $\langle \cos\phi \rangle$ quickly decays and in our simulation $\langle \cos\phi \rangle$ is dominated by random noise already at $s \sim 5a$.

2.D Radius of gyration

The knowledge of the bond vector correlation function allows one to calculate the radius of gyration

$$R_g^2 = \frac{1}{N^2} \sum_{n=1}^{N} \sum_{m=n+1}^{N} \left\langle R_{nm}^2 \right\rangle . \tag{2.55}$$

where the mean square distance between monomers n and m is

$$\left\langle R_{nm}^2 \right\rangle = a^2 \sum_{i=n}^{m} \sum_{j=n}^{m} h(i,j) . \tag{2.56}$$

The function $H(i,j)$ depends only on a single argument $s = a|j-i|$ (2.12) for the internal monomers i and j. Replacing the sums in Eq (2.55) by the integrals, we get

$$R_g^2 \simeq \frac{b^2 N}{6} + \frac{1}{3L^2} \int_{s_{\min}}^{L} (L-s)^3 h(s)\, ds, \tag{2.57}$$

where we have introduced the cut-off $s_{\min} \simeq b$. Substituting Eq (2.12) with $B = 0$ into Eq (2.57) we find

$$R_g^2 \simeq \frac{b_R^2 N}{6} - \lambda \frac{A}{b^3} \sqrt{N} \tag{2.58}$$

where the renormalized bond length b_R^2 depends on the cut-off $s_{\min}$ and the numerical constant $\lambda \simeq 0.47$. The $N^{-1/2}$ correction gives a stronger deviation from the limiting size $\lim_{N\to\infty} R_g^2$ than $1/N$ correction, as expected in the classical polymer chain models, (such as freely rotating model or worm-like model) with exponentially decaying correlations (Eq (2.1)).

2.E Swelling curve

The effective Hamiltonian of the chain with monomers interacting with the effective potential $f(\mathbf{x}-\mathbf{x}') = 1-\exp\left(-U(\mathbf{x}-\mathbf{x}')/k_BT\right)$ is

$$\frac{H}{K_BT} = \frac{3}{2b^2}\int_0^N \dot{x}^2 ds + \frac{1}{2}\iint_0^N ds_1 ds_2 f(\mathbf{x}(s_1)-\mathbf{x}(s_2)) + \tag{2.59}$$

$$\frac{C}{6}\iiint_0^N ds_1 ds_2 ds_3 \delta(\mathbf{x}(s_1)-\mathbf{x}(s_2))\,\delta(\mathbf{x}(s_2)-\mathbf{x}(s_3)). \tag{2.60}$$

where $\dot{x} = \frac{dx}{ds}$. For the sake of simplicity in this appendix the variable s is the dimensionless contour length measured in the units of bond length a. The mean square end-to-end distance:

$$R^2 = \left\langle [\mathbf{x}(N)-\mathbf{x}(0)]^2 \right\rangle_H. \tag{2.61}$$

can be calculated using the perturbation theory:

$$H = H_0 + H_{int} \tag{2.62}$$

where

$$\frac{H_0}{k_BT} = \frac{3}{2a^2}\int \dot{x}^2 ds \tag{2.63}$$

and

$$H_{int}k_BT = \frac{1}{2}\int \frac{d^3\mathbf{k}}{(2\pi)^3}\tilde{f}_{\mathbf{k}}\iint ds_1 ds_2 e^{i\mathbf{k}(\mathbf{x}(s_1)-\mathbf{x}(s_2))} - \frac{3}{2}\left(\frac{1}{a^2}-\frac{1}{b^2}\right)\int \dot{x}^2 ds + \tag{2.64}$$

$$C\int_0^N ds_1 \int_0^{s_1} ds_2 \int_0^{s_2} ds_3 \int \frac{d^3\mathbf{k}_1}{(2\pi)^3}\int \frac{d^3\mathbf{k}_2}{(2\pi)^3} e^{i\mathbf{k}_1[\mathbf{x}(s_1)-\mathbf{x}(s_3)]+i\mathbf{k}_2[\mathbf{x}(s_2)-\mathbf{x}(s_3)]} \tag{2.65}$$

Here we introduce the Fourier component $\tilde{f}_{\mathbf{k}}$ of the potential $f(\mathbf{x})$:

$$\tilde{f}_{\mathbf{k}} = \int d^3\mathbf{x} e^{-i\mathbf{k}\mathbf{x}} f(x) = 4\pi \int_0^\infty dx x^2 \frac{\sin(kx)}{kx} f(x) \tag{2.66}$$

In the first order in H_{int} we get

$$R^2 = R_0^2 + \delta R^2, \tag{2.67}$$

where

$$R_0^2 = a^2 N \tag{2.68}$$

and the first order contribution to mean square end-to-end distance due to interactions is

$$\delta R^2 = \left\langle [\mathbf{x}(N) - \mathbf{x}(0)]^2 H_{int} \right\rangle_{H_0} - \left\langle [\mathbf{x}(N) - \mathbf{x}(0)]^2 \right\rangle_{H_0} \langle H_{int} \rangle_{H_0}. \tag{2.69}$$

To find a we impose the condition, that R_0^2 gives the best result for R^2, that is, $\delta R^2 = 0$, or

$$\left\langle [\mathbf{x}(N) - \mathbf{x}(0)]^2 H_{int} \right\rangle_{H_0} = \left\langle [\mathbf{x}(N) - \mathbf{x}(0)]^2 \right\rangle_{H_0} \langle H_{int} \rangle_{H_0} \tag{2.70}$$

In order to calculate the integrals we first consider

$$J(\mathbf{h}) \equiv \left\langle e^{i \int \mathbf{h}(s)\mathbf{x}(s) ds} \right\rangle_{H_0} \tag{2.71}$$

with

$$\mathbf{h}(s) = \mathbf{h}[\delta(s-N) - \delta(s)] + \mathbf{k}[\delta(s-s_1) - \delta(s-s_2)] \tag{2.72}$$

and get (for $0 < s_1, s_2 < N$):

$$J(\mathbf{h}) = \exp\left[-\frac{1}{6}\mathbf{h}^2 a^2 N - \frac{1}{6} a^2 \mathbf{k}^2 |s_1 - s_2| + \frac{1}{3} a^2 \mathbf{h}\mathbf{k}(s_2 - s_1) \right] \tag{2.73}$$

Differentiating it with respect to **h** we get

$$\left\langle [\mathbf{x}(N)-\mathbf{x}(0)]^2 e^{i\mathbf{k}(\mathbf{x}(s_1)-\mathbf{x}(s_2))}\right\rangle_{H_0}$$
$$= \left[a^2 N - \frac{1}{9}a^4\mathbf{k}^2(s_2-s_1)^2\right]\exp\left(-\frac{1}{6}a^2\mathbf{k}^2|s_1-s_2|\right) \tag{2.74}$$

The second integral can be written as

$$\frac{\left\langle [\mathbf{x}(N)-\mathbf{x}(0)]^2 \exp\left[-\frac{3\varepsilon}{2a^2}\int \dot{x}^2 ds\right]\right\rangle_{H_0}}{\left\langle \exp\left[-\frac{3\varepsilon}{2a^2}\int \dot{x}^2 ds\right]\right\rangle_{H_0}} = \frac{a^2}{1+\varepsilon}N \tag{2.75}$$

Differentiating it with respect to ε at $\varepsilon = 0$ we find

$$\left\langle [\mathbf{x}(N)-\mathbf{x}(0)]^2 \frac{3}{2a^2}\int \dot{x}^2 ds\right\rangle_{H_0} - \left\langle [\mathbf{x}(N)-\mathbf{x}(0)]^2\right\rangle_{H_0}\left\langle \frac{3}{2a^2}\int \dot{x}^2 ds\right\rangle_{H_0} = a^2 N. \tag{2.76}$$

Using the two integrals above, we rewrite the condition (2.70) in the form

$$\frac{1}{2}\int \frac{d^3\mathbf{k}}{(2\pi)^3}\tilde{f}_{\mathbf{k}}\iint ds_1 ds_2 \frac{1}{9}a^4\mathbf{k}^2(s_2-s_1)^2\exp\left(-\frac{1}{6}a^2\mathbf{k}^2|s_1-s_2|\right)$$
$$= \frac{3}{2}\left(\frac{1}{b^2}-\frac{1}{a^2}\right)a^4 N \tag{2.77}$$

Calculating integrals over s_2 and s_1 with the aid of equality

$$\int_0^N ds_1 \int_0^{s_1} ds_2 (s_1-s_2)^2 e^{-z(s_1-s_2)}$$
$$= N^4 \frac{2z^2-6+e^{-z^2}\left(6+z^4+4z\right)}{z^8} \equiv N^4 F\left(z^2\right) \tag{2.78}$$

with $z^2 = \frac{1}{6}a^2\mathbf{k}^2 N$ we find

$$\frac{1}{9}\int \frac{d^3\mathbf{k}}{(2\pi)^3}\mathbf{k}^2 \tilde{f}_{\mathbf{k}} F\left(z^2\right) = \frac{3}{2}\left(\frac{a^2}{b^2}-1\right)N. \tag{2.79}$$

Substituting $\tilde{f}_{\mathbf{k}} = \tilde{f}_0 + \left(\tilde{f}_{\mathbf{k}} - \tilde{f}_0\right)$ we obtain

$$\tilde{f}_0 \frac{N^{3/2}}{\pi^{3/2}}\frac{\sqrt{6}}{a^3} + \frac{1}{9}\int \frac{d^3\mathbf{k}}{(2\pi)^3}\mathbf{k}^2\left(\tilde{f}_{\mathbf{k}} - \tilde{f}_0\right)F\left(z^2\right) = \frac{3}{2}\left(\frac{a^2}{b^2}-1\right)N. \tag{2.80}$$

Substituting Eq (2.66) we get

$$\tilde{f}_0 \frac{N^{3/2}}{\pi^{3/2}}\frac{\sqrt{6}}{a^3} - \frac{2}{9}\frac{N^4}{\pi}\int_0^\infty dx x^2 f(x)\int_0^\infty k^4 dk\left[1-\frac{\sin(kx)}{kx}\right]F\left(z^2\right) = \frac{3}{2}\left(\frac{a^2}{b^2}-1\right)N. \tag{2.81}$$

Changing variable of integration, $k \to z = \sqrt{cN} = a\sqrt{N}k/\sqrt{6}$, we get

$$\tilde{f}_0 \frac{N^{3/2}}{\pi^{3/2}}\frac{\sqrt{6}}{a^3} - \frac{N^{3/2}}{\pi}\frac{8\sqrt{6}}{a^3}\int_0^\infty dx x^2 f(x) J\left(\frac{\sqrt{6}x}{a\sqrt{N}}\right) = \frac{3}{2}\left(\frac{a^2}{b^2}-1\right)N, \tag{2.82}$$

where

$$J(u) \equiv \int_0^\infty z^4 dz\left[1-\frac{\sin(uz)}{uz}\right]F\left(z^2\right). \tag{2.83}$$

We find that $J(u\to\infty) = \frac{1}{2}\sqrt{\pi}$ and at small u (large N) we obtain

$$J(u) = \frac{1}{2}\pi u - \frac{5}{8}\sqrt{\pi}u^2 + \frac{1}{8}\pi u^3 + \ldots \tag{2.84}$$

Introducing $\alpha \equiv a/b$ we end with (at large $N \gg 1$)

$$\alpha^2 = 1 + \frac{z'}{\alpha^3} + \frac{A'}{\alpha^4} - \frac{A}{\alpha^5 b^5\sqrt{N}} \tag{2.85}$$

with

$$z' = \frac{2\sqrt{6}}{3\pi^{3/2}b^3}\tilde{f}_0\sqrt{N} \tag{2.86}$$

and

$$A' = -\frac{16}{b^4}\int_0^\infty dx x^3 f(x), \qquad A = -\frac{20\sqrt{6}}{\pi^{1/2}}\int_0^\infty dx x^4 f(x). \tag{2.87}$$

Notice, that $\tilde{f}_0$ is just the second virial coefficient. The last term $\sim A$ can be dropped at $N \gg 1$ not very close to θ point.

Chapter 3

Polymer molecules on surface

3.1 Image analysis

Scanning force microscopy is an amazing technique that allows direct visualization of molecular size objects, as opposed to indirect methods such as ion scattering, ellipsometry, etc. However, this visual form of experimental output turns the routine of systematic analysis of observed data into a challenging task. Individual and collective properties of microscopic objects that appear on an image need to be measured and analyzed (e.g. averaged and compared). This problem brings us into the broad and versatile discipline of digital image analysis.

Digital image analysis (DIA) as the name states is the computer based technology. Its applications at present include photography, printing, satellite image processing, medical image processing, face detection, feature detection, face identification, car traffic detection and microscope image processing. The main topic of our interest here will be the last one, microscope image processing. Our goal here is the fast and reliable method capable to detect imaged molecules and to measure their characteristics.

The general task of DIA, that is detection and quantification of objects and picture elements in an arbitrary digital image is enormously complicated. So far the only universal instrument

capable of doing that is the human brain, which in its turn has its own limitations. Therefore, to achieve our goal we need to make use of specific properties of our molecular images obtained by atomic force microscopy. This procedure can also be applied to other types of images that share certain characteristics with AFM molecular images.

3.2 Molecular images

Molecular image is visual representation of 2-dimensional array of data measured with sampling device of scanning microscope as it traverses across the sample surface. Here and in the following we will discuss the analysis of linear molecules, but the method is applicable to any linear object, such as cylindrical micelles or arms of branched molecules. The algorithm of molecule detection and quantification that we utilize here can be roughly divided into three stages. In the first stage the candidate areas containing objects are isolated on a substrate. In the second stage the molecule contour is searched, including both the perimeter and central line. Finally, various parameters of the molecule are computed, such as its length, area, curvature, etc. These procedures are described in details below.

3.2.1 Isolating molecules from substrate

The smallest possible section of an image is called picture element, or *pixel*. Pixel is characterized by its position and color. Pixel color represents a certain physical property of corresponding point on the sample surface, e.g. height, charge, hardness or adhesion strength. To simplify the discussion in the following text we will refer to the amplitude of the measured property as the *virtual height*, or simply the *height*, h, of the pixel.

We employ the height discrimination as the simplest way of separating molecule images from the substrate. To identify the molecules we first look up isles of pixels that have height exceeding certain *threshold*, h_0. The preliminary filtering by isle area can be performed at

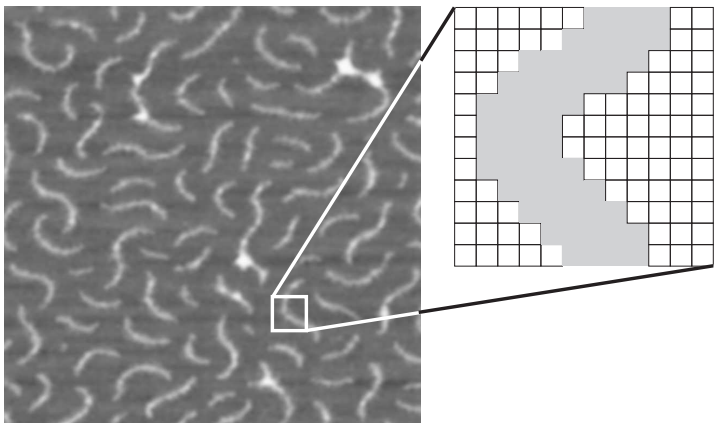

Figure 3.1: Molecule image after separation from substrate. Pixels belonging to the molecule are shown in gray.

this stage. Isles of area below the given lower limit or above the upper limit are deleted from the collection. This procedure removes trash pixels appearing due to noise or dust, and sorts out overlapping molecules, whose area is well above the average. Fig.3.1 shows the resulting image of the molecule after the separation procedure, with pixels belonging to the molecule shown in gray.

3.2.2 Detecting the contour

Contour detection is the most sophisticated and computationally intensive step in our image analysis procedure. The results of contour detection include molecule perimeter (outline) and its central line. Central line is needed in order to calculate molecule length, curvature and orientation. Molecule perimeter is the length of contact line of adsorbed molecule and also can be used to characterize the molecule shape (e.g. by the ratio of outline length to central line length).

One of the possible methods of constructing the molecule central line is the iteration of thinning procedure [45]. Thinning is done by stripping off pixels from the edge until a 1-pixel thick line remains, that consists of 4-connected or 8-connected pixels*. Thinning method can

*Pixel is 4(8)-connected to the other pixel when it is one of its 4(8) nearest neighbors on a square lattice.

handle branched molecules as well as linear ones. The main drawbacks of this are its sensitivity to edge defects, and the necessity to correct for the molecule ends to avoid shortening.

We have developed another method to identify the molecule central line, based on the concepts of the graph theory [46]. We treat all pixels of the molecule as graph vertices. Graph vertices corresponding to spatially neighboring pixels are connected by edges. The weight of an edge that connects two vertices located at $\mathbf{v}_i = \{x_i, y_i\}$ and $\mathbf{v}_j = \{x_j, y_j\}$ is defined as

$$l_{ij} = d_{ij} \cdot W(\mathbf{v}_i, \mathbf{v}_j) \tag{3.1}$$

where d is the Euclidean distance between the corresponding pixels. The weight function $W(\mathbf{v}_i, \mathbf{v}_j)$ is used to adjust the length of topological trajectories along the vertices.

Our molecular graph is connected, that is every vertex can be reached from any other vertex by walking along the edges. The sequence of vertices that will be visited in the course of this walk forms the *path* connecting the given pair of vertices. We use the fact that central line connects the two most remote points of the molecule, that is its ends. The protocol for the automated search of the central line can be set up as follows.

1. Choose a seed vertex $\mathbf{v}_0$* on the molecular graph, and find shortest paths†. to all other vertices. Since the weights of all edges are non-negative we can employ the Dijkstra algorithm [47, 48].

2. Select the longest of these paths and use the vertex $\mathbf{v}_1$ at its other end as the starting point for next step.

3. Find the shortest paths from the vertex $\mathbf{v}_1$ to all vertices. The longest of these paths now represents the central line.

*The choice of a seed vertex is arbitrary, we used the vertex at the highest point in molecule.

†The problem of determination of the shortest path between two vertices has many important practical applications, e.g. in transportation or internet traffic routing.

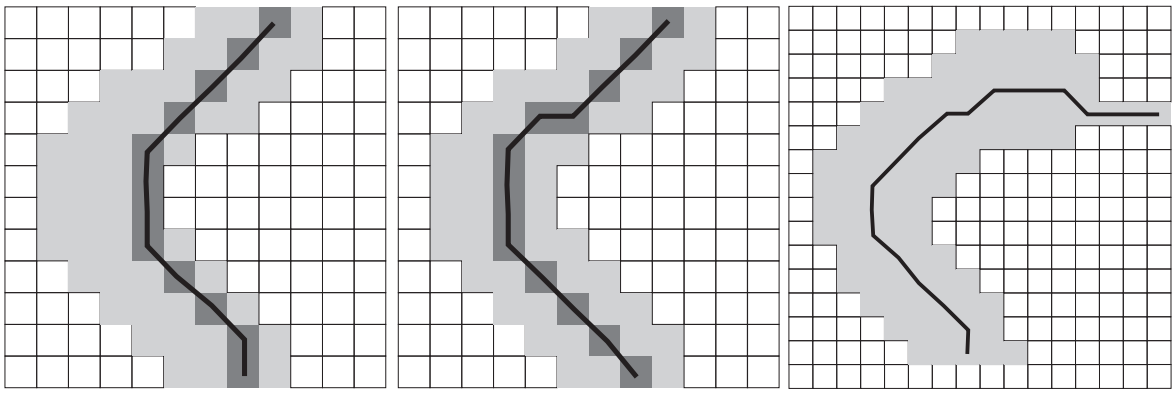

Figure 3.2: (a). The shortest path between the molecule ends when edge weight corresponds to its euclidean length. (b). The shortest path between the ends with the edge weight adjusted according to the distance from the border. (c). The result of ”tentacle” defects at molecule ends on the obtained central line.

The trajectory of the resulting line depends strongly on the choice of the weight function $W(\mathbf{v}_\mathrm{i},\mathbf{v}_\mathrm{j})$. Fig. 3.2a shows an example of the shortest path between the farthest points of molecule for the case of uniform $W(\mathbf{v}_\mathrm{i},\mathbf{v}_\mathrm{j}) = const$. To give the preference to trajectories that do not approach the molecule boundary we assign higher weight to the boundary vertices than to the central ones:

$$W(\mathbf{v}_\mathrm{i},\mathbf{v}_\mathrm{j}) = d_\mathrm{max} - \sqrt{d_\mathrm{b}(\mathbf{v}_\mathrm{i})d_\mathrm{b}(\mathbf{v}_\mathrm{j})}$$

where $d_\mathrm{b}(\mathbf{v})$ is the shortest distance from the given vertex $\mathbf{v}$ to the boundary, and d_max is the constant added to insure that $W(\mathbf{v}_\mathrm{i},\mathbf{v}_\mathrm{j})$ is non-negative. Now that the length of graphs edges increases in the viscinity of molecule boundary, the trajectory of central line tends to avoid the molecule borders (Fig. 3.2b).

The procedure described here gives satisfactory results in most practical cases. Its main point of failure is the presence of certain defects shaped as thin ”tentacles” and protruding from the molecule ends (Fig. 3.2c). The edges belonging to these ”tentacles” have high weight and for the path seeking algorithm they seem to lead to more distant vertices than at the actual molecule ends. However, these defects can be easily removed by the slight preliminary blurring of the image.

3.2.3 Calculation of length and curvature

A number of discretized line length estimation protocols has been suggested [49]. The simplest way is to compute the sum of Euclidean distances between the pixels. However, according to certain studies [50] this method tends to underestimate the length. A more accurate methods are based on Freeman estimator, Kulpa estimator or the corner count estimator [50], but the statistical and semiempirical nature of the estimators has lead us to the application of splines [51]. The polynomial spline is constructed using pixels of the discretized line as knot points. Length of the spline is a more accurate and better reproducible estimate of molecular length, as it is less affected by the change of image resolution.

3.3 Molecular brushes on the surface

3.3.1 Measuring molecular weight by atomic force microscopy

Accurate characterization of molecular weight distribution is very important since many physical properties of polymers depend on the chain dimensions. The characterization is straightforward for low molecular weight polymers with a simple chemical structure, e.g., linear chain homopolymers without ionic and associating groups. However, experimentalists face severe difficulties when studying large molecules possessing a complex architecture, heterogeneous chemical composition, charged moieties, and/or surface active groups. Here, we propose to use a combination of two well-known techniques, i.e., Atomic Force Microscopy (AFM) and Langmuir-Blodget (LB) technique, to determine the number average molecular weight and the molecular weight distribution. This approach does not require any prior information about the chemical composition and the architecture of macromolecules. The only necessary condition for the practical application of this method is visualization of individual molecules [52].

Methods

The method includes several steps. First, one should prepare a stock solution of a known concentration c. Second, a certain amount (volume V) of the solution is spread over the water surface in a Langmuir trough to form a monolayer of adsorbed molecules. In the third step, the monolayer is compressed laterally to a certain area S_{LB} at which a dense monolayer forms. Step four is the transfer of the monolayer onto a solid substrate for AFM studies. One should also measure the transfer ratio Tsthe ratio of the change in area of the water supported monolayer during the transfer onto a solid substrate to the area of the substrate. Finally, step five, the transferred monolayers are scanned by AFM for visualization of individual molecules.

From the concentration, volume, and transfer area SLB one can calculate the mass per unit

area as

$$m_{LB} = c \cdot V / S_{LB} \tag{3.2}$$

One should note that the film transfer could be performed at any area S_{LB}, provided that the monolayer is dense and the molecules can be clearly resolved. Visualization of individual molecules by AFM enables their counting within the micrograph area S_{AFM} to determine the number of molecules per unit area n_{AFM}

$$n_{AFM} = N / S_{AFM} \tag{3.3}$$

The error associated with the molecular density decreases as $1/\sqrt{N}$. In this work, we counted approximately 3000 molecules for each sample to obtain a relative standard deviation of 4%.

From the mass and molecular densities, one can calculate the number average molecular weight M_n using the following equation

$$M_n = \frac{m_{LB}}{n_{AFM}} \frac{T}{m_{am}} \tag{3.4}$$

where T is the transfer ratio and m_{am} is the atomic mass unit $m_{am} = 1.6605 \times 10^{-24} g$. The transfer ratio corrects for the difference between the mass density of the water supported monolayer and the mass density of the transferred film.

In addition, AFM images give length distribution of the visualized molecules. The length fraction of molecules with length L can be calculated as

$$w_L = L / L_n n_L \tag{3.5}$$

where L_n is the number average length for an ensemble of counted molecules and n_L is the number fraction of molecules with length L. Assuming that the molecular weight is propor-

tional to the contour length ($M \approx L$) the length distribution should be identical to the molecular weight distribution from GPC (weight fraction w_M versus molecular weight M).

Materials and characterization

A PBA brushes with different lengths of the side chains was prepared by grafting of n-butyl acrylate from a poly(2-(2-bromopropionyloxy) ethyl methacrylate) (pBPEM) macroinitiator as described elsewhere [53, 54]. The number average degree of polymerization of the backbone is $N_n = 567 \pm 35$. The degree of polymerization of PBA side chains of the two samples is 20 and 51 (details of MALLS-GPC and SLS characterization is in ref. [53]). AFM images were collected using a Multimode IIIa Atomic Force Microscope (Veeco Metrology Group) in tapping mode. To ensure accurate counting of visualized molecules, several images were collected from the same sample but in different areas, using different scan sizes and scan directions. For every sample about 3000 molecules were counted. The counting was performed using a custom software program for analysis of digital images. The program is designed to identify the molecular contour, and to determine the contour length, the end-to-end distance, and the curvature distribution.

Results

Figure 3.3 shows an AFM image of sample with shortest side chains ($n_n = 20$) on mica. The image demonstrates the uniform coverage of the substrate, which enables accurate counting of molecules. However, the image also reveals two issues, which may affect the quantitative analysis: (i) crossing of molecules and (ii) partial visualization of molecules at the image borders. Because the image analysis program automatically captures all kinds of individual species, it considers both the crosses and the molecular fragments as molecules, i.e., two crossed molecules are counted as one and partially imaged molecules are counted as whole molecules.

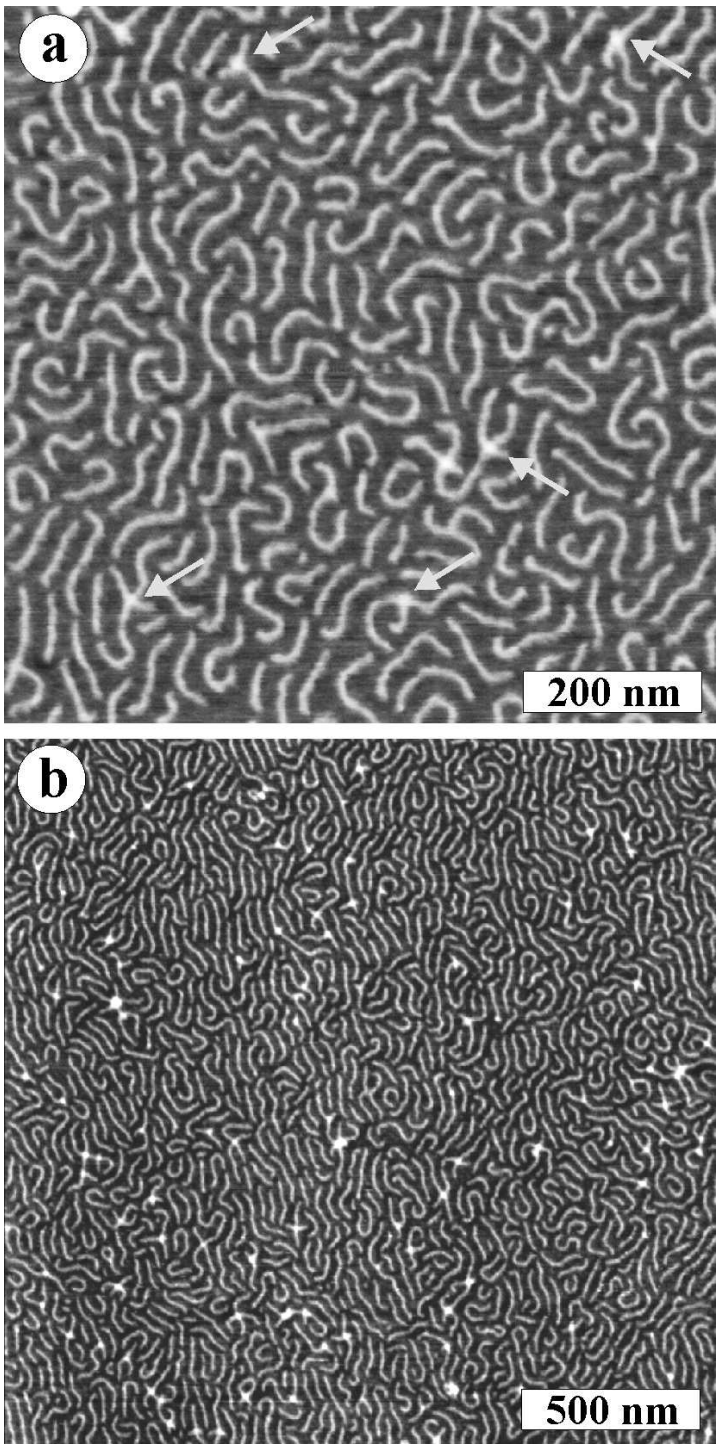

Figure 3.3: Individual molecules of polymer 1 were clearly resolved by tapping mode AFM. The higher resolution image (a) demonstrates details of the molecular conformation including crossing molecules indicated by arrows. The larger scale image (b) demonstrates the uniform coverage of the substrate.

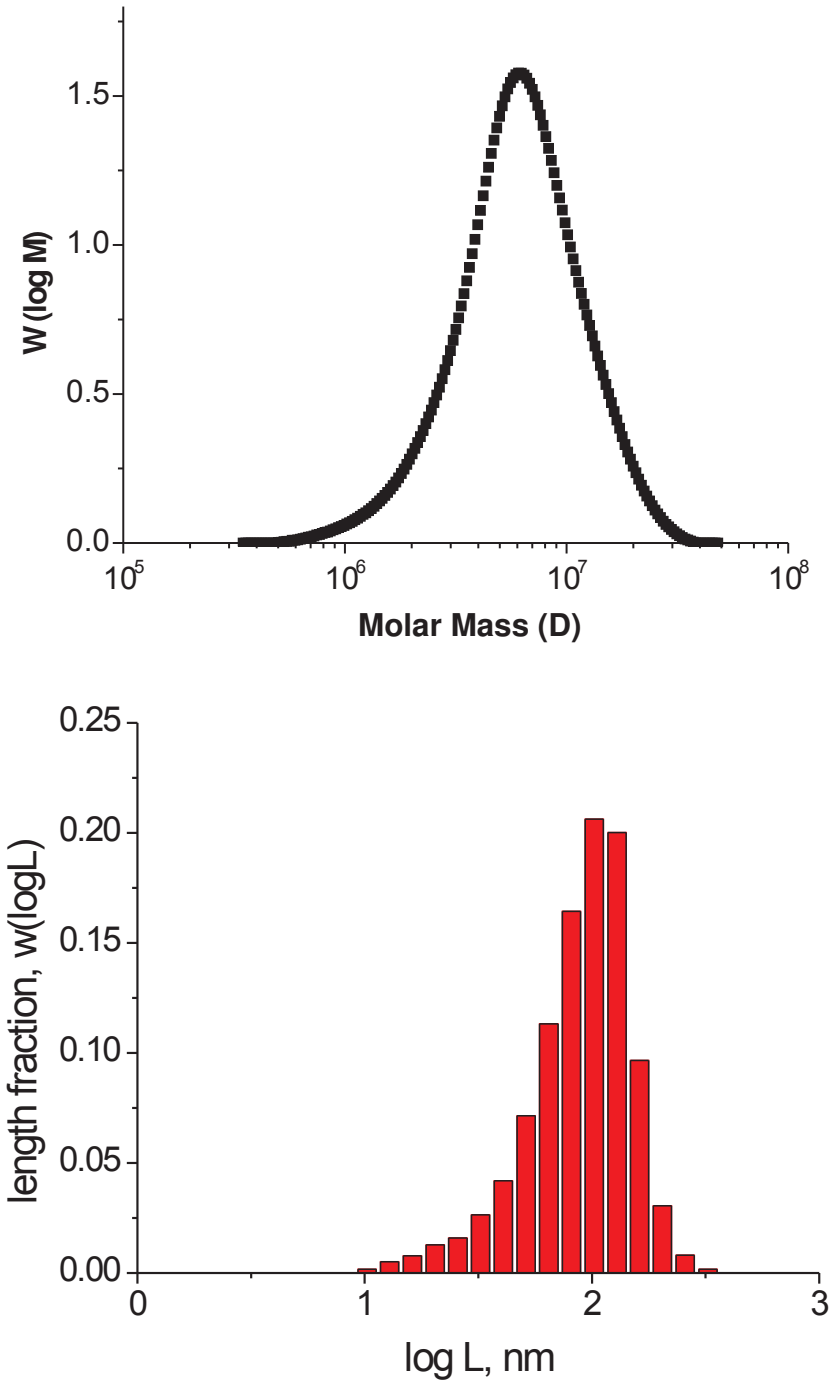

Figure 3.4: (top) MALLS-GPC diagram presents molecular weight distribution of Sample 2. (bottom) The molecular length distribution (eq. 3.5) was measured by AFM for an ensemble of 3060 molecules.

Table 3.1: Molecular Weights of PBA Cylindrical Brushes Determined by SLS, MALLS-GPC and the AFM-LB Methods

	SLS	MALLS-GPC		AFM	
N_n	M_n,[a] 10^6	M_n,[b] 10^6	M_w/M_n[c]	M_n,[d] 10^6	L_n,[e] nm	L_w/L_n[f]
20	1.4	1.6	1.54	1.5 ± 0.15	108 ± 6	1.33
51	3.9	4.7	1.46	4.0 ± 0.35	113 ± 5	1.20

[a] The number average molecular weight was calculated from the weight average molecular weight determined by SLS using the polydispersity index M_w/M_n from GPC. [b] Number average molecular weight of brush molecules determined by MALLS-GPC. [c] Polydispersity index of the molecular weight measured by MALLS-GPC. [d] Number average molecular weight determined by the AFM-LB approach (eq 3.4). [e] Number average length measured for an ensemble of 300 molecules with a statistical deviation of 5 nm. [f] Polydispersity index of the molecular length obtained from AFM images.

Therefore, crossed molecules will overestimate the M_n, whereas the partially imaged border molecules increase the number of molecules per unit area, i.e., underestimate the M_n. The problem of crossings was resolved by increasing the number of counted species by the number of crosses. This approach can be applied to relatively short molecules that do not cross themselves to form complex topologies such as cycles, knots, and networks. As to the border molecules, the total number of molecules was recalculated as $n_{AFM} = n - n_p + n_b$, where n is the number of individual molecular species visualized by AFM, n_p is the number of partially imaged molecules, and nb is the number of equivalent border molecules of complete length. The number of the equivalent molecules was determined as $n_b = \sum_i L_{b,i}/L_n$, where $L_{b,i}$ is the length of the partially imaged molecules and L_n is the number average length of the complete molecules. The L_n value was determined separately as $L_n = \sum_i L_i/N$, where L_i is the length of complete molecules.

After the above corrections, the molecular density of the LB films was calculated. For example, the sample with $n_n = 51$ gave $n_{AFM} = 124 \pm 5 \text{molecules}/\mu m^2$. Using eq.3.4 one could calculate the number average molecular weight $M_n = (4.0 \pm 0.4) \times 10^6$. The error in M_n can be reduced by counting more molecules. The molecular weights obtained from the AFM-LB method were compared to SLS and MALLS-GPC data obtained for the same polymers.

Table 3.1 demonstrates remarkably good agreement between the methods. The agreement is indeed remarkable because the AFM-LB and SLS/GPC measurements were carried out independently and are based on different principles.

In addition to the number average molecular weight, the AFM-LB method allows characterization of the molecular weight distribution. The latter can be derived from the molecular length distribution assuming that the molecular weight is directly proportional to the length, i.e., $M \sim L$. This assumption is often reasonable, especially in this work where the ATRP synthesis yields brushes with a uniform structure along the backbone. This property was confirmed by GPC analysis of the side chains detached from the backbone [55]. A general procedure for statistical analysis of the contour length is well established for different types of linear molecules [56–61]. Figure 3.4 shows molecular weight and molecular length distributions determined for Sample 2 by MALLS-GPC and AFM, respectively. In both diagrams, the Y-axes correspond to weight fraction. One can see that the distributions obtained by the different methods are very similar. Note that in both cases the distributions cover three decades of the molecular sizes. It would also be instructive to notice that the GPC distribution of cylindrical brushes is virtually identical to the distribution of the macroinitiator $M_n = 1.5 \times 10^5$, $M_w/M_n = 1.4$ used for preparation of the brush molecules. This observation is consistent with the above assumption of the uniform composition of the brushes along the backbone. Table 3.1 presents the polydispersity indexes obtained by GPC and AFM. The GPC values are somewhat larger than those from AFM. The difference can be attributed either to the intrinsic broadening of elution curves in GPC or to undercounting of small fractions of very small and very large molecules in AFM images. The undercounting issue becomes relevant for samples with broader distributions. Their analysis would require scanning of larger areas with more molecules to improve statistical representation of minority fractions. This and other discrepancies between the molecular weights in Table 3.1 need further investigation.

Conclusion

The combination of AFM and LB techniques allowed accurate determination of the number average molecular weight and molecular weight distribution. The method relies on visualization of individual molecules which enables their counting. The AFM-LB data demonstrated remarkably good agreement with results obtained by the MALLS-GPC technique. Although the application of the method was demonstrated for brush molecules, it can be applied for other kinds of visualizable species.

3.3.2 A Flory Theorem for Structurally Asymmetric Mixtures

Polymer solutions are unique physical systems in which the interactions between macromolecules become screened as polymer concentration increases. Therefore, in polymeric melts, where the interactions are completely screened, macromolecules behave as almost ideal chains obeying a random walk statistics. The ideality of polymer chains in a melt was first established over fifty years ago by Flory [3] and become later known as the Flory theorem [42, 62]. There is a very interesting consequence of the Flory theorem, which is related to the swelling behavior of polymer chains in a polydispersed melt. A "guest" molecule with the degree of polymerization N_A embedded into a melt of chemically identical polymer chains with the degree of polymerization N_B starts swelling when its degree of polymerization is sufficiently large such that $N_A > N_B^{2/(4-d)}$, where d is the space dimensionality. For 3-D ($d = 3$) and 2-D ($d = 2$) mixtures, shorter macromolecules tend to penetrate and swell a guest macromolecule when $N_A > N_B^2$ and $N_A > N_B$, respectively. Experimental studies on the binary polymer mixtures confirmed swelling of longer test chains in 3-D [63–66] and 2-D [59] melts of shorter chains as predicted theoretically.

The recent developments in the area of the nanocomposite materials pose new challenges in determining factors controlling stability and conformation of polymeric mixtures that con-

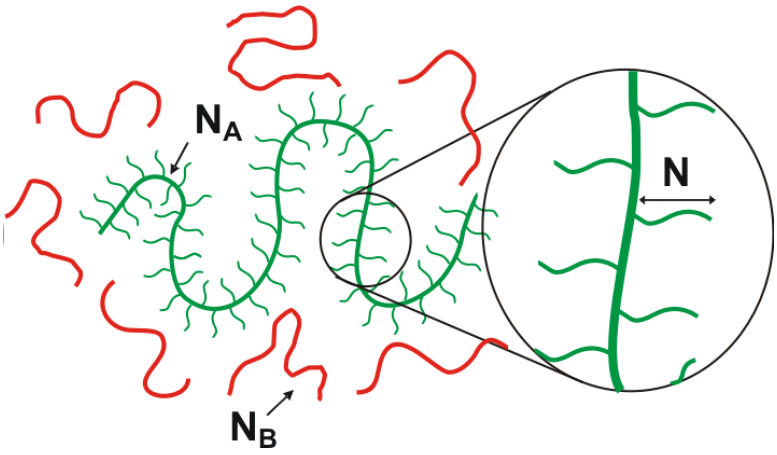

Figure 3.5: Schematics of a brush-like macromolecule embedded in a melt of linear chains with a degree of polymerization N_B. Brush's backbone and side chains have the degrees of polymerization N_A and N, respectively.

tain molecular species with different architectures [67–69]. Mixtures of linear polymers with dendrimers, branch polymers, nanoparticles, carbon nanotubes, and clay platelets are used to create new generation of nanocomposite materials. Since the structures of these molecules are significantly different from those of linear polymer chains, this makes applicability of the classical Flory theorem to these mixtures questionable. In this section, we show that one can modify the Flory approach to describe mixtures of structurally and geometrically different species. We use atomic force microscopy (AFM) to visualize individual macromolecules in thin films [19, 70, 71] and monitor conformations of well-defined brush-like macromolecules with the backbone degree of polymerization N_A and the side chain degree of polymerization N embedded into a monolayer of linear chains of the degree of polymerization N_B (Fig. 3.5). The experiments clearly show that molecular brushes swell as the degree of polymerization of the surrounding linear chains, N_B, decreases. The intriguing finding of this study is that the swelling behavior depends not only on the length of the linear chains (N_B) but also on the degree of polymerization of brush's side-chains (N) that define the structural asymmetry of the mixed species. To explain these findings, the Flory theorem of polymer melts was reformulated to account for the structural asymmetry and to establish the boundaries of the swelling region.

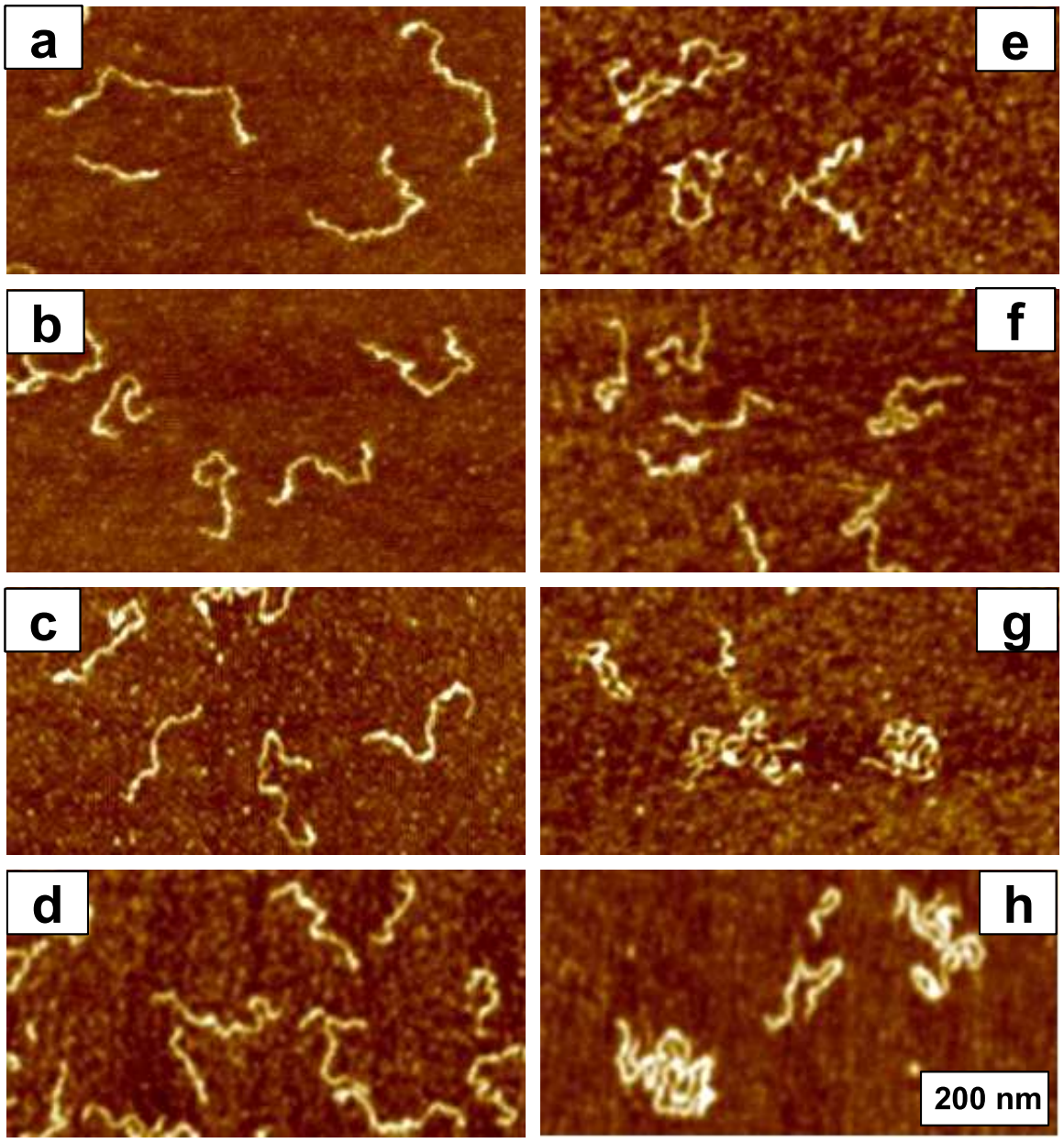

Figure 3.6: Height AFM images of individual brush molecules embedded into monolayers of linear pBA chains having different degrees of polymerization: a – N_B=11, b - N_B=24, c - N_B=102, d - N_B=214, e - N_B=322, f - N_B=602, g - N_B=1766, and h - N_B=8813.

The brush-like macromolecules used in this study consist of a long flexible backbone (N_A=1580) with densely grafted poly(*n*-butylacrylate) (pBA) side chains (N=10). These macromolecules were synthesized by atom transfer radical polymerization [72]. For the polymeric solvent/matrix to be chemically identical to the molecular brushes, we used melts of linear pBA chains. A series of well-defined linear pBA's with degree of polymerization ranging from 10 to 9000 and monomer molecular weight M_0=128 were purchased from Polymer Source Inc.

Monolayers of pBA brushes dispersed in linear pBA chains were prepared by the Langmuir-Blodgett technique. To obtain these dispersions, the brush molecules were first mixed with matrix polymers at a ratio of 10/90 wt./wt.% in chloroform, a common solvent for both the brush and linear polymers. The solution was then deposited onto the water surface of a Langmuir trough. After allowing 30 minutes for system equilibration, the water-supported monolayers were transferred onto a solid substrate (mica) at a constant pressure of 0.5 mN/m and a transfer ratio of 0.98. The transferred samples were studied by AFM aiming at visualization of conformations of a single brush molecule.

Figure 3.6 shows sequence of conformations of a worm-like molecular brushes sparsely dispersed in a matrix of linear pBA chains. The height contrast results from the partial desorption of the side chains that segregate around the brush backbone and form a ridge of approximately 1 nm in height. The side chains that remain adsorbed to the substrate are not distinguishable from the surrounding melt of linear pBA chains. Figure 3.6 shows evolution of conformational transformations of brush macromolecules with increasing the degree of the polymerization of linear chains. The guest molecules change their conformation from expanded coils in a melt of short chains (Fig. 3.6a,b) to a compact coil in a melt of longer chains (Fig. 3.6g,h). Note that in 2-D systems, the ideal coil conformation corresponds to a dense packing of a polymer chain. There is also a crossover region between the two pure regimes (Fig. 3.6c-f).

Conformation of single molecules were analyzed using a custom-designed software program which was able to identify molecular contours and directly measure the contour length,

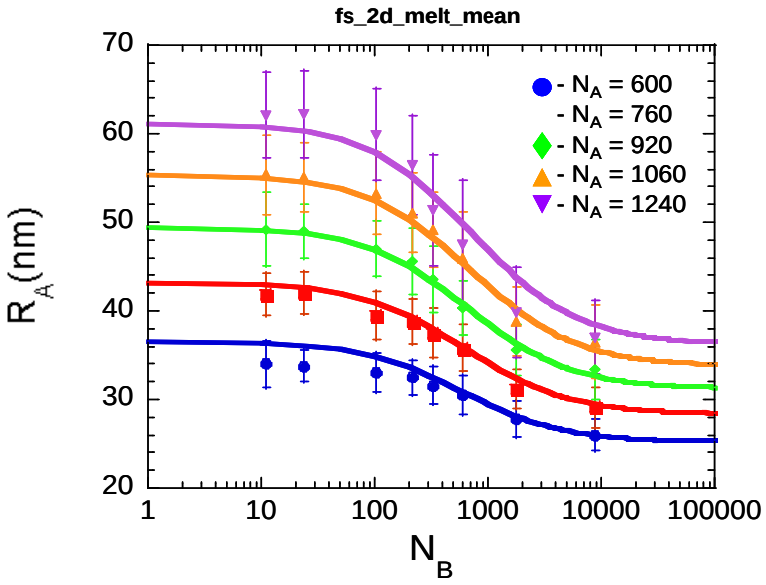

Figure 3.7: Dependence of the square root of the mean-square radius of gyration of pBA brush on the degree of polymerization of linear pBAs chains for different degrees of polymerization of the backbone (N_A). The solid lines are the best fit to the crossover equation 6 with a single set of two adjustable parameters A_1=0.31±0.01 and A_2=0.3±0.08.

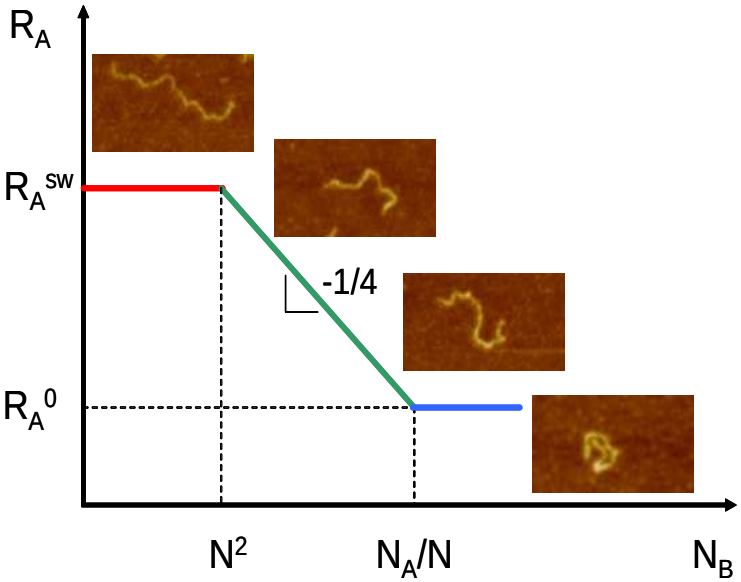

Figure 3.8: Three conformational regimes of a brush-like macromolecule embedded in a melt of linear chains with a degree of polymerization N_B. The lower boundary of swollen test chain regime, N_B=N^2, is determined by the degree of polymerization of the side chains (N), while the upper boundary of the ideal chain regime, N_B=N_A/N, also depends on the degree of polymerization of the brush's backbone (N_A).

the radius of gyration, and curvature distribution of the molecules. Clear resolution of individual molecules enabled visual fractionation of single molecules and molecular clusters. The latter were excluded from the conformational analysis. Figure 3.7 shows the root mean-square radius of gyration of the pBA brushes measured at different degrees of polymerization of the pBA linear chains. The radius of gyration was averaged for ca. 300 brush molecules with a similar contour length which gave an experimental error of about 10%. Note that the swelling stops at much longer chains ($N_B \gg 1$), unlike linear chains that are expected to continue swelling down to $N_B \cong 1$. Therefore, the location of the crossover region notably differs from those of structurally symmetric melts.

To understand the physical mechanism of the observed swelling behavior we have developed a scaling model of brush-like macromolecules in a melt of linear chains. Consider a brush-like macromolecule with the main-chain degree of polymerization N_A, the side-chain degree of polymerization N, and the monomer size b (Fig. 3.5). The adsorbed brush molecules can be envisioned as a ribbon with a width of $D \cong bN$ and a contour length of $L_0 = bN_A$. This brush molecule is dispersed in a melt of linear chains with the degree of polymerization N_B. Since we are dealing with an extremely dense brush, wherein every monomeric unit of the backbone contains one side chain, we assume that the linear chains do not interpenetrate the side chains. This assumption is based on the fact that in tightly adsorbed brushes, the penetration is sterically impossible because the adsorbed side chains represent a 1-D brush aligned perpendicular the backbone with a distance between the chains of the order of 0.5 nm.

The effect of the linear chains on the swelling behavior of molecular brushes is associated with the entropy of mixing of these chains with a brush. A test molecule occupies only the fraction of the area φR_A^2, where $\varphi = L_0 D/R_A^2 = b^2 N_A N/R_A^2$ is the volume fraction of monomers belonging to a brush inside area R_A^2, which leaves an area $(1-\varphi)R_A^2$ accessible for the liner chains. The entropic contribution to the free energy due to placement of the linear chains with

the degree of polymerization N_B over the area R_A^2 is equal to:

$$\frac{F_{mix}}{k_BT} \approx \frac{R_A^2}{b^2}\frac{(1-\varphi)}{N_B}\ln(1-\varphi) \underset{\varphi\ll 1}{\approx} -\frac{N_AN}{N_B} + \frac{b^2(N_AN)^2}{2N_BR_A^2} \tag{3.6}$$

Note that only the last term in the right hand side of Eq.(3.6) depends on the size of the brush molecule R_A. Here and below we use scaling analysis and neglect all numerical prefactors on the order of unity. The Flory free energy of a guest molecule mixed with the linear chains can be written as a sum of the free energy of mixing (Eq. (3.6)) and of the test molecule elastic free energy [42]. The elastic free energy term accounts for the change of the conformational entropy as guest macromolecule swells from the ideal size

$$R_A^0 \approx (L_pL_0)^{1/2} \approx bN_A^{1/2}N^{3/2} \tag{3.7}$$

where $L_p \cong bN^3$ is the persistence length of an adsorbed brush macromolecule, which a ribbon with a width of $D \cong bN$ [73]. Thus, the total free energy of the molecular brush dispersed in a melt of linear chains is

$$\frac{F}{k_BT} \approx \left(\frac{R_A}{R_A^0}\right)^2 + \frac{b^2(N_AN)^2}{N_BR_A^2} \tag{3.8}$$

The equilibrium probe molecule size is obtained by minimizing Eq.(3.8) with respect to the size R_A as

$$R_A \approx bN_A^{3/4}N^{5/4}N_B^{-1/4} \tag{3.9}$$

which is valid for intermediate values of the matrix chain's degrees of polymerization, N_B. For very long linear chains, the intrabrush interactions are almost completely screened. In this case, test macromolecule contracts and its size eventually approaches the ideal size $R_A \approx R_A^0$. This takes place at $N_B \approx N_A/N$. This upper boundary for the swollen brush regime is a surprising result because it points out that linear chains see a brush as a linear chain composed of N_A/N effective monomeric units. In other words, the ribbon-like brush with a width of bN and

contour length bN_A can be viewed as a chain of N_A/N monomeric units with linear size bN and having N^2 original monomers.

As the degree of polymerization of the linear chains, N_B, decreases the brush molecule swells. The brush becomes completely swollen with size

$$R_A^{sw} \approx L_p \left(\frac{bN_A}{L_p}\right)^{3/4} \approx b\,(NN_A)^{3/4} \tag{3.10}$$

at $N_B \approx N^2$ for which $R_A \approx R_A^{sw}$.

For even shorter linear chains, $N_B < N^2$, the brush is completely swollen and its equilibrium size does not depend on the degree of polymerization of the chain's forming the polymeric solvent. In Figure 3.8, we summarize different swelling regimes as function of the degree of polymerization of the solvent, N_B. It is important to point out that the interval of the intermediate linear chain's degree of polymerizations $N^2 < N_B < N_A/N$, in which a brush macromolecules swells, only exists when the number of monomers forming the brush backbone N_A is larger than N^3. The latter corresponds to the persistence length of tightly adsorbed brush macromolecule [73].

The dependence of a chain size on the system parameters in three conformational regimes depicted in Figure 4 can be approximated by a simple crossover formula

$$R_A = A_1 L_p \left(\frac{N_A}{N^3}\right)^{3/4} \left(\frac{1}{1+A_2 N_B/N^2} + \frac{N^3}{N_A}\right)^{1/4} \tag{3.11}$$

where A_1 and A_2 are numerical constants on the order of unity. These two constants are introduced to adjust the molecular size and the location of the crossover region, respectively. For long linear chains ($N_B > N_A/N$), the formula approaches the ideal size of a polymer brush $R_A^0 = A_1 b N_A^{1/2} N^{3/2}$ (see Eq. (3.7)). For melt of short linear chains ($N_B < N^2$), this expression reduces to the size of a completely swollen molecule $R_A^{sw} = A_1 b\,(NN_A)^{3/4}$. The crossover equation (Eq.(3.11)) was used to fit the experimental data using A_1 and A_2 as fitting parameters.

For different sizes of brush-like macromolecules, experimental data closely match the predicted swelling region with two adjustable parameters $A_1 = 0.31 \pm 0.01$ and $A_2 = 0.30 \pm 0.08$ (Figure 3.7). Overall, experiment and theory demonstrated excellent agreement confirming the dependence of the size of a test brush chain on the degree of polymerization of linear chains forming a two-dimensional melt. It is important to emphasize that for different brushes, both limiting values of their radius of gyration (R_A^0 and R_A^{sw}) can be accurately fitted with the same set of adjustable parameters.

One can easily generalize the presented above analysis to the case of a test macromolecule with thickness D, contour length L_0 and having a persistence length L_p immersed into a melt of the linear chains with the degree of polymerization N_B by rewriting Eqs.(3.6)-(3.8) in terms of chain parameters D, L_0, L_p and space dimensionality d. Such test chain begins to shrink when the excluded volume occupied by the host chains $b^d N_B$ becomes larger than the volume occupied by an effective monomer D^d of the guest molecule, $b^d N_B > D^d$. Above this crossover value, the matrix chains screen intrachain repulsive interactions between monomers of the test macromolecule, which is manifested by the decrease of the test molecule size with increasing degree of polymerization of the linear chains N_B as $R_A \approx \left(\frac{L_0^3 L_p D^{2d-2}}{N_B b^d}\right)^{\frac{1}{d+2}} \sim N_B^{-1/(d+2)}$. The shrinking continues until the size of the test molecule becomes comparable with its ideal size, $R_A^0 \approx (L_p L_0)^{1/2}$. This occurs when the degree of polymerization of the linear chains N_B is on the order of $L_0^{(4-d)/2} D^{2d-2}/(L_p^{d/2} b^d)$.

The generalized Flory theorem for mixtures of structurally asymmetric macromolecules can be formulated as follows: "Test macromolecules with thickness D, contour length L_0 and a persistence length L_p dispersed in a melt of linear chains with the degree of polymerization N_B will remain in their ideal (Gaussian) conformations until the degree of polymerization of the linear chains N_B exceeds $L_0^{(4-d)/2} D^{2d-2}/(L_p^{d/2} b^d)$. Shorter linear chains fill volume of the test macromolecules causing their swelling. This swelling continues until the excluded volume occupied by the linear chain $b^d N_B$ becomes comparable with the volume of the effective

monomer D^d of the test macromolecule."

3.3.3 Multiarm molecular brushes

Dense branching results in 3D molecules with a well-defined shape. The most prominent examples are spherical dendrimers [74–76], arborescent-graft polymers [77–79], monodendron-jacketed linear chains [80, 81] and cylindrical brushes [82–85]. The shape of these molecules is controlled by steric repulsion of the branches and is predetermined by the branching symmetry. An important property of branched architectures is that the molecular conformation can undergo transformations in response to changes in the environmental conditions [52]. Therefore, such molecules can be regarded as soft colloidal particles that can switch their shape, or tertiary structure. For example, cylindrical molecular brushes demonstrate a spontaneous phase transition from a cylindrical to a globular conformation with decreasing surface energy of the substrate [54]. This functional property can be used to design stimuli responsive nanometer-sized objects that could work as tiny springs or even engines, provided that a source of energy is included in the system. Recently, we have reported on the synthesis of starlike brush molecules that expanded our ability to control molecular conformation [86]. The three-arm and four-arm molecules showed a decrease in polydispersity with the number of arms. Presented here is a complete molecular analysis of multiarm brush molecules, including linear and two-arm molecules. We also studied the effect of the number of arms on the molecular weight polydispersity and on the ordering behavior of multiarm brushes adsorbed to a flat substrate.

Materials and characterization

A series of multiarm brushes with different numbers of arms was prepared by the grafting of *n*-butyl acrylate (nBA) from multiarm macroinitiators (backbones) using atom transfer radical polymerization (ATRP). The average molecular weights and molecular weight distributions

were measured by gel permeation chromatography (GPC). The details of synthesis and characterization were published elsewhere [87].

AFM images were collected using a Multimode atomic force microscope (Veeco Metrology Group) equipped with a Nanoscope IIIa control station in tapping mode. To ensure accurate counting of molecules, multiple images were collected from different areas of the same sample using different scan sizes and scan directions. The image analysis was performed using a custom software program. The program can identify the molecular contour and determine its length, end-to-end distance, contour curvature distribution, and parameters related to molecular ordering in two dimensions via reciprocal space image treatment.

Results

Figure 3.9a shows a height image of two molecules of the four-arm brushes with $n_n = 1100$ and $m_n = 41$, number-average degrees of polymerization of the backbone and the side chains, respectively. High topographic contrastwasachieved through the utilization of ultrasharp HiRes probes with a tip radius down to 1 nm. Figure 3.9b shows a transmission electron micrograph of a HiRes probe which demonstrates a forest of sharp needles grown from a regular Si tip. Since one of the needles is longer than the others, the longest needle actually probes the surface structure.

Molecular visualization provides a unique opportunity for the characterization of branched polymers. First, it gives direct evidence of their starlike architecture. Second, it allows for accurate measurements of the numberaverage molecular weight. Third, it enables length measurements of the star arms separately from the length of the whole molecule. Below we demonstrate a few applications of the molecular visualization to quantitative analysis of the molecular structure.

Using GPC with a light scattering detector, one can obtain relatively accurate information about the molecular weight distribution and the molecular dimensions in solution. However,

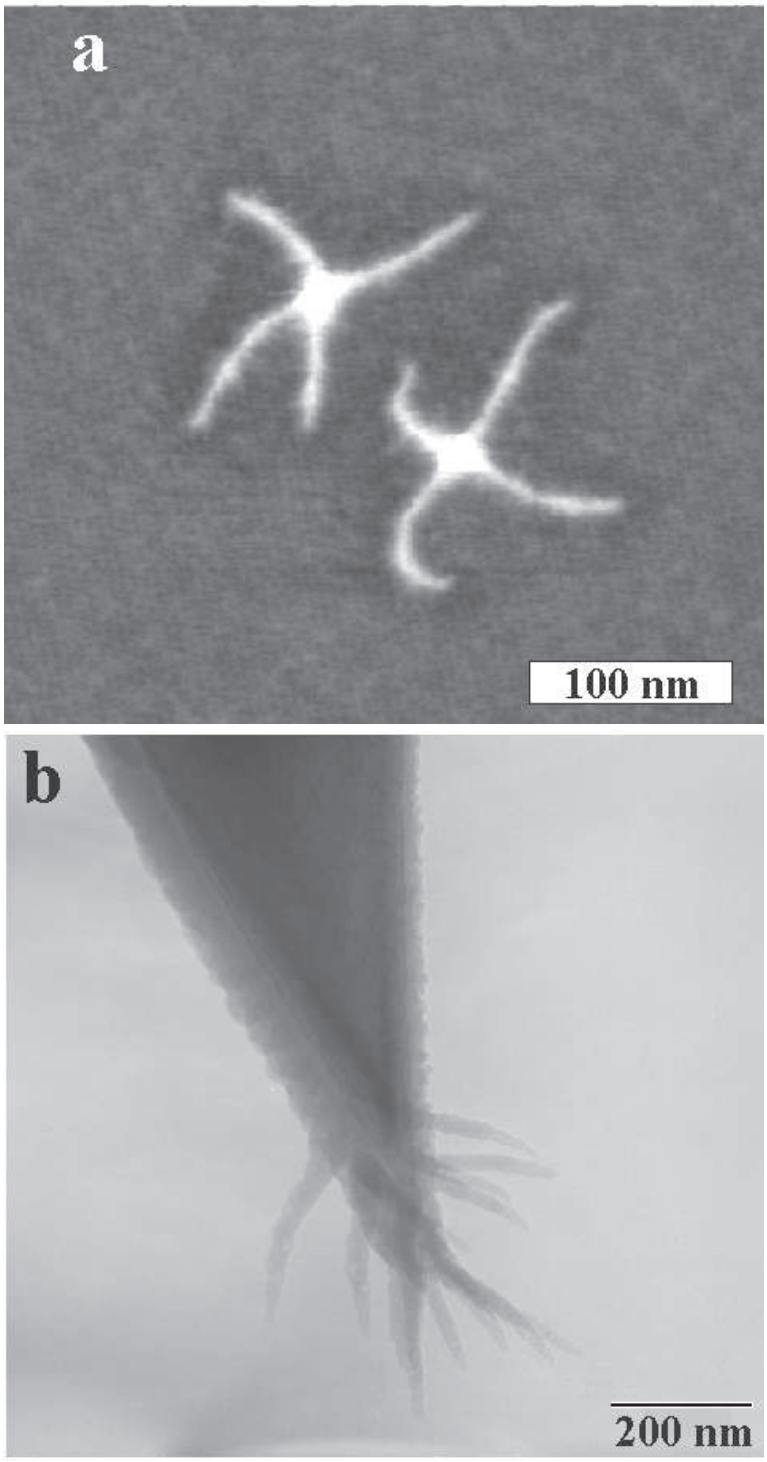

Figure 3.9: The height image (a) of single molecules of four-arm pBA brushes was obtained by tapping mode AFM using commercial HiRes probes (b). The probes were prepared by growing a forest of ultrasharp extratips with a radius down to 1 nm on top of a regular Si tip.

Table 3.2: Molecular Characterization by MALLS-GPC and AFM-LB Techniques

	macroinitiator[a]		brushes			degrees of polymerization	
samples	$M_n, 10^5$	PDI	$M_n^b, 10^6$	$M_n^c, 10^6$	PDI^b	n_n^d	m_n^e
1-arm (linear)	1.5	1.4	2.7	2.5	1.3	567	35
2-arm	1.9	1.3	1.1	1.8	1.3	720	17
3-arm	2.1	1.1	2.7	2.8	1.3	790	26
4-arm	2.8	1.1	5.5	6.0	1.3	1100	41

[a] Determined from MALLS-GPC in THF, dn/dc = 0.084. [b] Determined from MALLS-GPC in THF, dn/dc = 0.068. [c] The number-average molecular weight was determined by AFM-LB (ref [53]) from the mass per unit area ($\mu = M/S$) and the number of molecules per unit area ($\nu = N/S$) as $M_n = M/N = \mu/\nu$. [d] Number-average degree of polymerization of the macroinitiators: $n_n = M_n/M_0$, where $M_0 = 265 g/mol$ is the molar mass of BPEM. [e] Number-average degree of polymerization of the side chains: $m_n = (M_n^{brush} - M_n^{macroinitiator})/n_n m_0$, where $m_0 = 128 g/mol$ is the molar mass of BA.

themethodbecomes less accuratewhen analyzing large molecules ($qR_g > 1$) and molecules with complex architecture [88]. Recently, we have proposed a new characterization method based on a combination of the AFM and LB techniques to measure the number-average molecular weight and the molecular weight distribution of brush molecules [53]. The method is based on molecular visualization which allows counting of individual molecules and accurate measurement of the number of molecules per unit area of an LB monolayer. From the number density and the known mass per unit area, one can readily calculate the number-average molecular weight (see Experimental Section). Although the AFM measurements were done on a solid substrate, the number density is close to that on the water surface since the transfer ratio was close to unity ($T = 0.98$). For better averaging, a few hundred molecules were analyzed by measuring several AFM images (like those in Figure 3.12) from the same sample. The obtained results are summarized in Table 3.2. The method demonstrated excellent agreement with the MALLS-GPC results, even though the two techniques are based on different principles.

Along with being convenient and reliable for molecular weight determination, AFM enables accurate measurements of the molecular length. For the starlike brushes, one can measure the length of the arms separately from the length of the entire molecule. This demonstrates the

Table 3.3: Length Characterization from AFM Measurements

	individual arm		entire brush molecule			
sample	L_n (nm)[a]	PDI_L^b	L_n (nm)[a]	PDI_L^b	theor. PDI[c]	l_m^d (nm)
1-arm (linear)	130 ± 5	1.15 ± 0.08	130 ± 5	1.15 ± 0.08	1.15	0.23 ± 0.03
2-arm	69 ± 2	1.2 ± 0.2	137 ± 3	1.1 ± 0.2	1.075	0.19 ± 0.03
3-arm	55 ± 2	1.15 ± 0.08	165 ± 4	1.05 ± 0.08	1.050	0.21 ± 0.03
4-arm	64 ± 2	1.15 ± 0.08	256 ± 4	1.04 ± 0.08	1.038	0.23 ± 0.03

[a] L_n = number-average molecular length. [b] $PDI_L = L_w/L_n$ = length polydispersity index. [c] Determined from eq 3.13. [d] $l_m = L_n/N_n$ length per monomeric unit, where N_n is the number-average degree of polymerization of the backbone.

strong advantage of AFM compared to other techniques such as light scattering and viscosity measurements that give average molecular dimensions. The information about the arm-length distribution is important for gaining insight into the synthetic process by which the arms grow. Table 3.3 summarizes the obtained results. The length polydispersity index, $PDI_L = L_w/L_n$, of the arms was determined to be about 1.15 for every sample. The same PDI_L was measured for the linear molecules. This was expected because the macroinitiator, that is, the backbone, for each sample was synthesized in the same manner. Looking further at the whole molecule, the size polydispersities determined by AFM decreased with increasing functionality from 1.15 to 1.04. The lowest polydispersity was found for the four-arm brushes. This had direct effects on the ordering of the molecules, which will be discussed in the second part of the section.

The PDI_L values determined from the length distribution are lower than PDI values from the mass distribution measured by GPC (Table 3.2). The disagreement may be caused by fundamental differences in the size analysis by the MALLS-GPC and AFM-LB techniques. GPC blindly measures all species that are injected into the separation columns. The species may include a large variety of side products including a small fraction of unreacted macroinitiators, individual side chains, and cross-linked molecules. In contrast, AFM is based on real space analysis which enables selecting only the right species, that is, multiarm brush molecules that possess a characteristic shape.

Table 3.3 also demonstrates good agreement between the experimental and theoretical val-

ues of PDI. The theoretical values were calculated assuming random growth of the arms. Based on this assumption, one can readily calculate the polydispersity index of a star molecule, PDI = PDI_{star}. Indeed, if one assumes that the molecular weight distribution of arms is given by a normalized function, $\rho(M)$ (i.e., $\int_0^\infty \rho(M)dM = 1$), such that $\rho(M) = 0$ for all $M < 0$, the corresponding distribution of a star-shaped molecule containing f arms ($\rho(M)_{star}$) of arbitrary chosen lengths reads as a series of f autoconvolutions $\rho(M)_{star} = \rho(M) * \rho(M) \ldots \rho(M)$, where $\rho(M) * \rho(M) \equiv \int \rho(\mu)\rho(M-\mu)d\mu$. From the definition of PDI,

$$\mathrm{PDI} = \frac{\rho^{(2)}(M)}{(\rho^{(1)}(M))^2} \tag{3.12}$$

where $\rho^{(i)}(M)$ denotes the i-th momentof the corresponding distribution, the PDI_{star} can be calculated as

$$\mathrm{PDI}_{star} = \frac{\mathrm{PDI}_{arm}}{f} + \frac{f-1}{f} \tag{3.13}$$

For example, it is easy to show that for $f = 2$

$$\begin{aligned} \rho^{(2)}(M)_{star} &= \int \{\rho(M) * \rho(M)\} M^2 dM = \\ &= \int\int \rho(\mu)\rho(M-\mu)M^2 d\mu dM = \\ &= 2\rho^{(2)}(M) + 2(\rho^{(1)}(M))^2 \end{aligned} \tag{3.14}$$

For any arbitrary integer value of f, one obtains

$$\rho^{(2)}(M)_{star} = f\rho^{(2)}(M) + f(f-1)(\rho^{(1)}(M))^2 \tag{3.15}$$

from which eq 3.13 follows directly. The equation is also consistent with the Flory-Schulz theory for condensation polymerizations which proceed in a random fashion [89, 90]. Also

noted in Table 3.3 is the length per monomeric unit (l_m), which is a measure of the extension of the arms. Values of l_m cannot exceed 0.25 nm, which corresponds to the monomer length of a fully extended carbon chain in the all-trans conformation. All the samples have similar l_m values, meaning that the backbones are equally extended on the substrate, which further substantiates our analysis by AFM.

Conformational transition and surface ordering

AFM allows for the visualization of the conformational changes star molecules undergo upon two-dimensional compression on a Langmuir trough. As shown previously for linear brush molecules [54], the compression causes partial desorption of side chains which is followed by coiling of the otherwise extended backbone (Figure 3.10). In the case of linear brush molecules, one observes a transition from a rodlike to a globular conformation characterized by a semi-spherical shape. In this section, we show that unlike linear brushes the starlike brushes form a disklike shape with a height much smaller than its diameter (Figure 3.10b,c). Note that the side chains undergo only partial desorption. Those side chains which remain adsorbed on the substrate plane form a dense corona around the coiled part and thus control the surface arrangement of the adsorbed molecules. Below we discuss only the four-arm brush, since the behavior of the twoarm brushes is identical to that of linear molecules reported earlier [54], and the three-arm molecules behave similarly to the four-arm ones.

A monolayer of the four-arm brush was visualized by AFM at three different degrees of compression. Figure 3 shows the surface pressure-molecular area isotherm for the four-arm brush. Similar to other fluids, compression of the multiarm brushes was reversible, as expected for equilibrium spreading. However, the isotherm has characteristics that distinguish it from those of conventional liquids. The pressure onset occurred at a mean molecular area of approximately 14 000 nm^2 and rose until an area of 8000 nm^2 where the pressure reached a plateau of 22.5 mN/m. This plateau continues to about 5600 nm^2 where a second plateau at

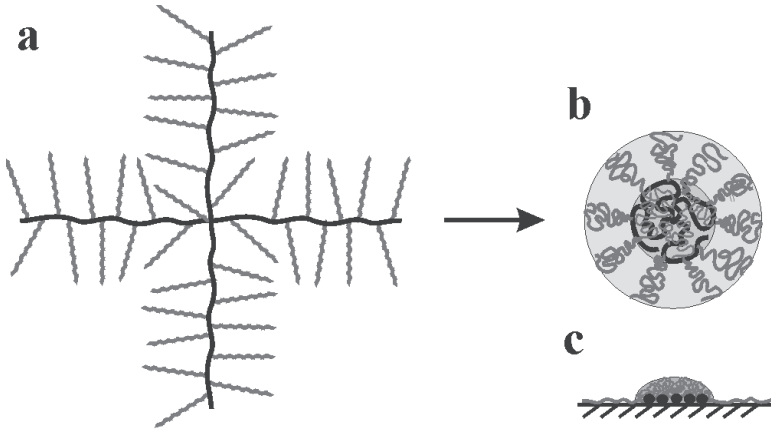

Figure 3.10: Schematic for a conformational transition of a multiarm brush molecule caused by two-dimensional compression. As opposed to the hemispherical (globular) conformation of compressed linear brush molecules (ref [54]), multiarm brushes undergo a transition from an extended conformation (a) to a disklike conformation (b,c). Parts b and c show overhead and side views of the disklike conformation where the backbone remains adsorbed to the substrate.

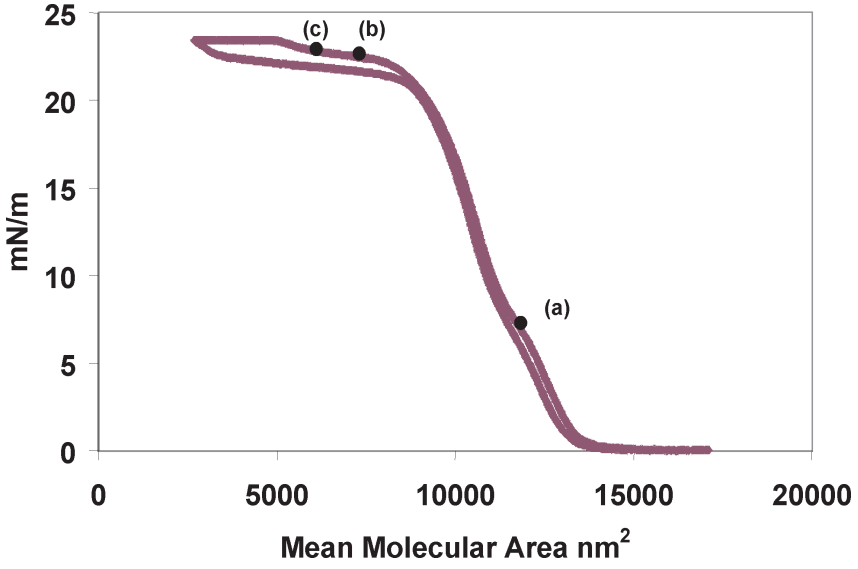

Figure 3.11: The surface pressure-molecular area isotherm for the four-arm brush was measured at $T = 23^{\circ}C$. The mean molecular area(MMA)was determined for the number-average molecular weight $M_n = 5.5 \times 10^6$ obtained by MALLS-GPC. The mean molecular area is the average area of a single brush molecule on the water surface. The points on the compression isotherm indicate compressions at which a monolayer was transferred onto mica forAFMstudies. Each point corresponds to an AFM image in Figure 3.12.

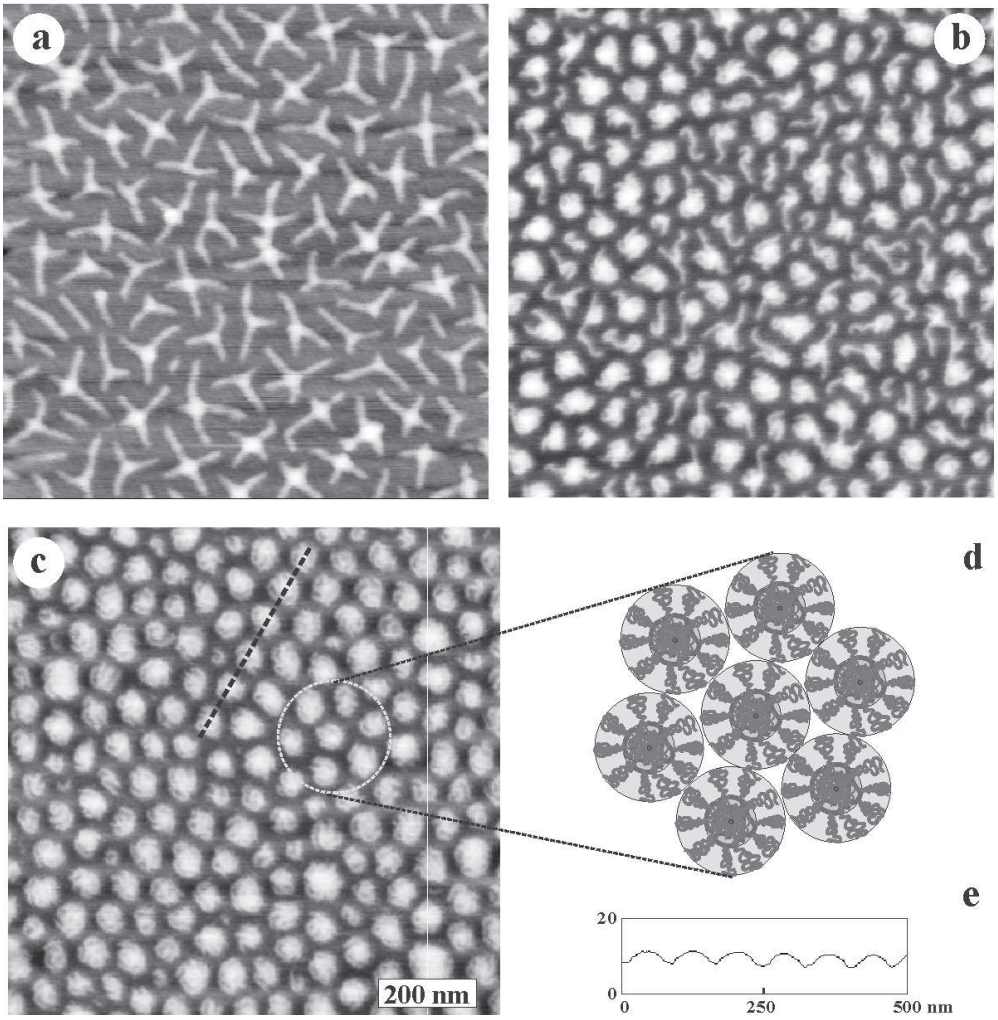

Figure 3.12: AFM observes the transition of the four-arm brush from a starlike to a disklike conformation. The transition was caused by lateral compression of monolayer films on the surface of water. The height images correspond to different degrees of compression depicted in Figure 3.11. The cartoon in part *d* shows hexagonal ordering of disklike molecules stabilized by steric repulsion of adsorbed side chains. The cross-sectional profile in part e was measured along the dashed line in part *c*.

$\pi = 23.5 mN/m$ is observed. A similar behavior was observed for linear cylindrical brushes $f = 1$ [54]. To study the conformational changes occurring upon compression, four samples were transferred onto a solid substrate, that is, mica, at different degrees of compression. Numbers on the isotherm indicate molecular areas where the samples were taken.

Figure 3.12 shows molecular conformations depicted by AFM during the transition for the

four-arm brush. At a molecular area of 12 000 nm^2 (a), all of the arms are fully extended. As the molecules were compressed to a molecular area of 7200 nm^2 (b), the arms began to shorten and the middle of the molecules heightened slightly. At this area, one observes a coexistence of extended molecules and disklike molecules, as well as some that appear to be in a transient state. At a molecular area of 6200 nm^2 (c), all molecules became disklike (Figure 3.12d) with a disk height much smaller than its diameter (Figure 3.12e).

At low pressures, starlike molecules are disordered because of the flexible nature of the arms which result in the irregular shape of adsorbed molecules. Once the molecules transform from an extended to a disklike conformation, they also gain local hexagonal order stabilized by steric repulsion of adsorbed side chains. Regions of short-range hexagonal order are clearly seen in the AFM images (see Figure 3.12d). The observed order is consistent with the lower polydispersity of the four-arm brushes. One can compare the ordering behavior of the four-arm brushes ($PDI_L = 1.04$) and linear brushes ($PDI_L = 1.15$). Figure 3.13 shows larger scale images of compressed monolayers of linear brushes in globular conformation (Figure 3.13a) and four-arm brushes in the disklike conformation (Figure 3.13b). Visual comparison of the images of the linear and four-arm compressed brushes reveals that the monolayer of the four-arm molecules is more ordered. In the insets in Figure 3.13, one can clearly see small domains with nearly perfect hexagonal order that are also evidenced by the 2D power spectral density, $P_2(s)$, where s is the 2D reciprocal space vector. The $P_2(s)$ of the four-arm brush demonstrates a well-defined 6-fold symmetry, whereas the linear brush has a less defined pattern indicating less order. The observed modulation in the scattering intensity vanishes in large samples. Figure 3.14 shows angular dependence of the radial-averaged intensity $I(\phi)$ for $1 \times 1 \mu m^2$ and $5 \times 5 \mu m^2$ AFM images. This function was calculated as

$$I(\phi) = \int P_2(s, \phi) ds \tag{3.16}$$

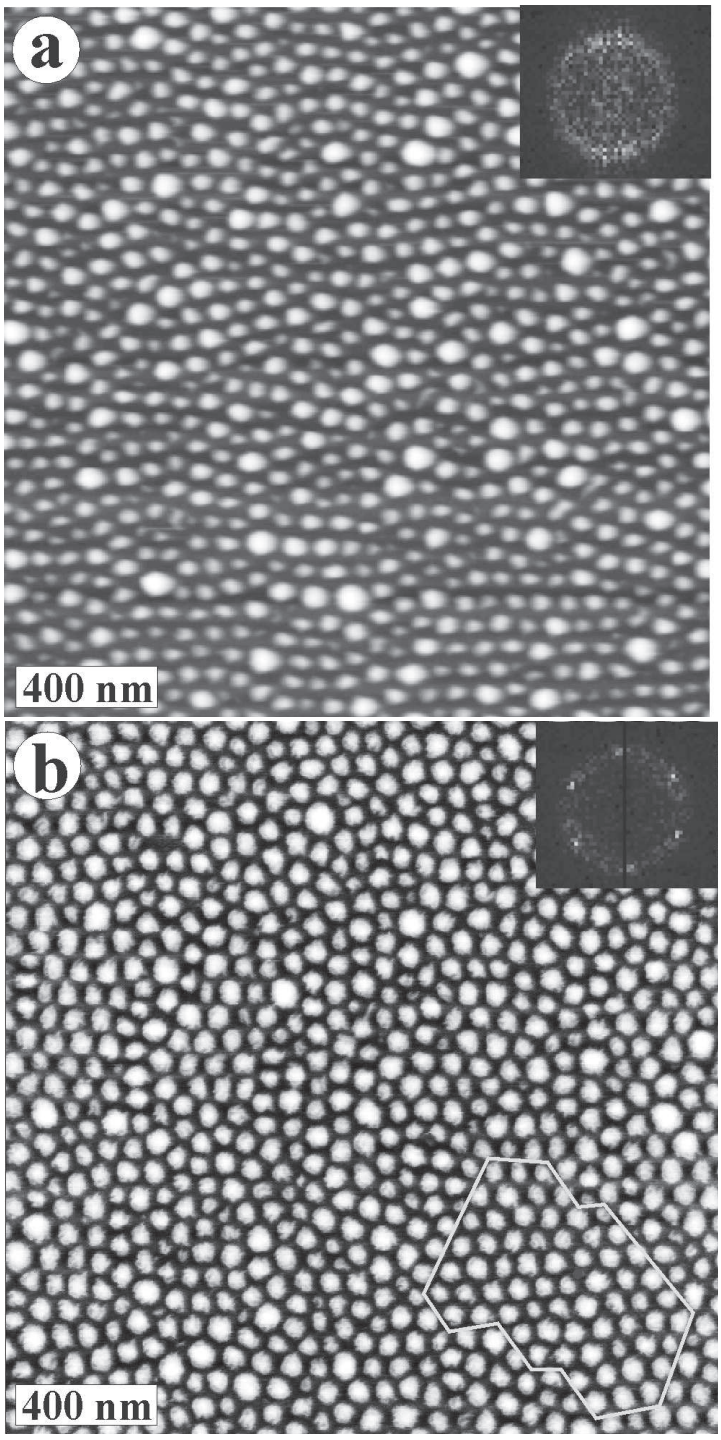

Figure 3.13: Height images of the compressed linear brush (a) and four-arm brush (b). The highlighted area in part b shows a domain with nearly perfect hexagonal order. The insets show 2D power spectral density measured for $1 \times 1 \mu m^2$ areas of the monolayers. Six peaks are clearly visible in the four-arm PSD, indicating the presence of hexagonal order in the system.

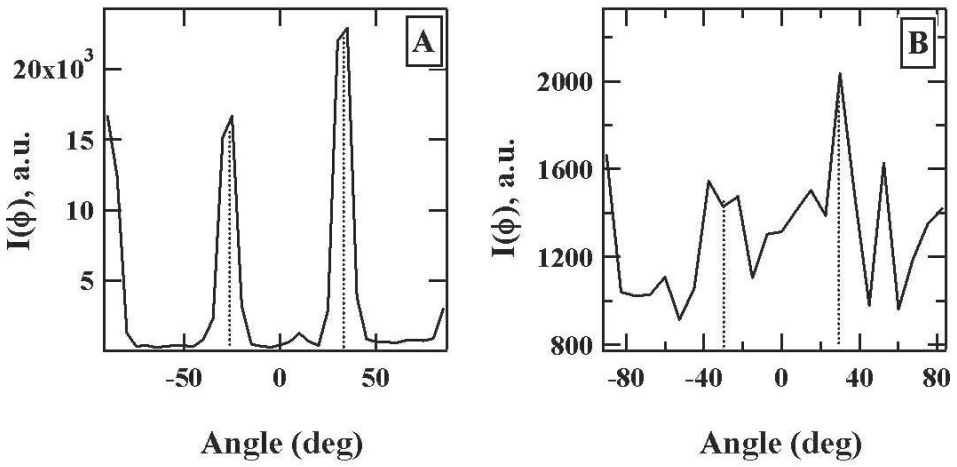

Figure 3.14: Angular dependence of the 2D power spectral density function $P_2(s)$ calculated according to eq 3.16. Parts A and B correspond to AFM images of the four-arm brushes with sizes of 1×1 and $5 \times 5 \mu m^2$, respectively. The presence of the characteristic hexagonal pattern, which is very clear for the smaller image, can still be detected for the larger-scale image.

where the integration is performed in the range of s corresponding to the first-order diffraction peak (see insets in Figure 3.13). The smaller areas clearly show distinct peaks separated by 60° (Figure 3.14a). However, even for the larger area, one can distinguish peaks located 60° apart (Figure 3.14b).

To characterize quantitatively the degree of order, one has to analyze the translational and orientational correlations of AFM images and calculate the corresponding correlation lengths. The radial translational correlation function $C(R)$ was obtained from the 2D scattering function as described in ref. [91].

Although the radial correlation function in Figure 3.15a shows 5-6 secondary maxima, the translational correlation length (ξ_T) was determined to be only about 76 nm, or one intermolecular distance, for the four-arm brush and 72 nm for the linear brush. This indicates that both the four-arm and linear molecules are fairly disordered. The obtained result seems counterintuitive becauseAFM images in Figures 3.12d and 3.13b reveal local hexagonal packing of the four-arm molecules. The relatively rapid decay of the correlation function can be explained not only by translational disorder of the molecules but also by the distribution of their sizes

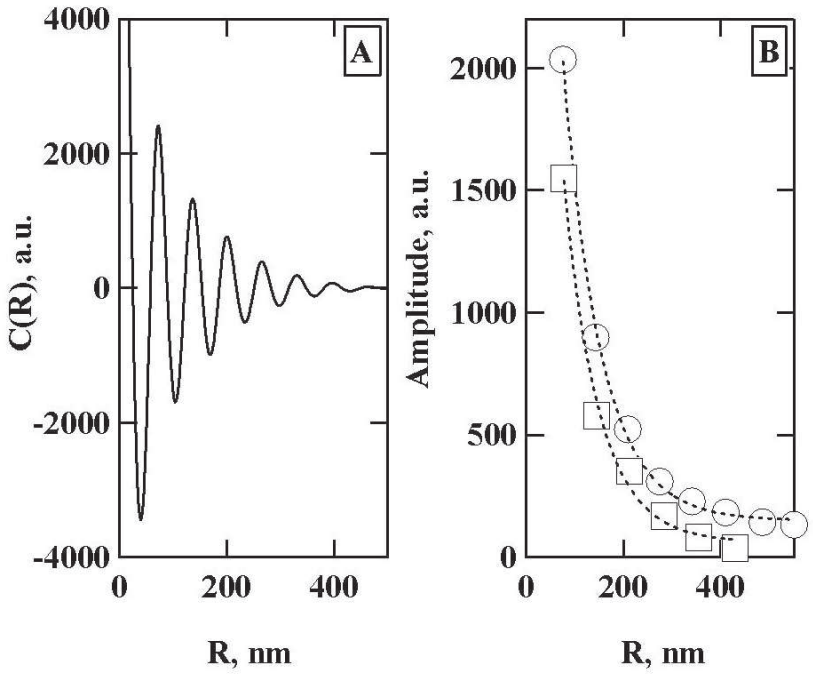

Figure 3.15: (A) Radial correlation function exemplified for the case of the four-arm brush molecule ($1 \times 1 \mu m^2$ image). (B) The decays of the amplitude of the secondary maxima of $C(R)$ as a function of distance for four-arm (circles) and linear brushes (squares) were fitted by an exponential function to obtain the translational correlation lengths $\xi_T = 76$ and 72 nm for the four-arm and linear brush, respectively.

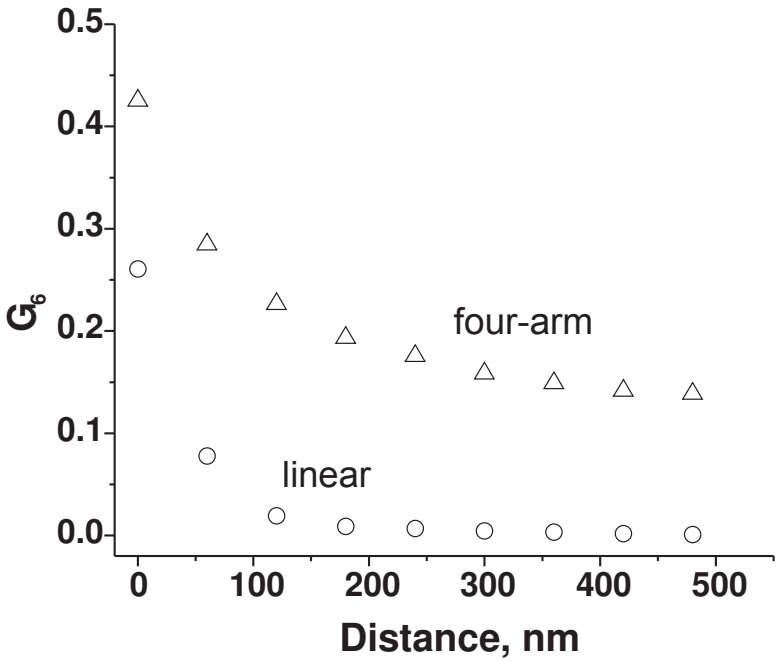

Figure 3.16: The orientational correlation function decays exponentially to a finite number on a short-range scale for the four-arm brush but decays to zero for the linear brush. For larger AFM images, both functions tend to zero at large distances.

and irregularity of their shape. Therefore, in such cases of partially disordered 2D systems, an in-depth analysis of orientational correlations between the molecular centers of mass would be more relevant. For example, hexatic crystals demonstrate perfect hexagonal order despite local defects that result in low ξ_T.

Figure 3.16 shows orientational correlation functions recovered from $1 \times 1 \mu m^2$ AFM images of linear and four-arm brush molecules. In contrast to the translational correlations, the orientational correlations were analyzed in real space. The data points in Figure 3.16 were obtained by first recording the positions of the center of mass of individual molecules and then correlating angles between nearest-neighbor bonds and the x-axis. A detailed description of the analysis can be found in research papers and textbooks [92–94]. The plots in Figure 3.15 demonstrate exponential decay of orientational order which tends to zero at large distances. By

fitting the data points with the orientational correlation function for an amorphous phase,

$$\lim_{r\to\infty} G_6(r) \sim \exp\frac{-r}{\xi_6} \tag{3.17}$$

one can determine the orientational correlation length (ξ_6), which measures the long-range correlation of the orientation of local hexagonal axes. ξ_6 was determined to be approximately 740nm,which is about 10 intermolecular distances. In contrast, the linear compressed brush has a correlation length of only 130 nm, or 2 intermolecular distances.

The increase in ordering from the linear brush to the four-arm brush is consistent with the decrease in polydispersity, the linear brush having a PDI of 1.15 and the four-arm brush having a PDI of 1.04. One can define polydispersity as the relative standard deviation of the mass distribution which can be calculated from the PDI as

$$\mathrm{RSD}_m = \sqrt{\mathrm{PDI}-1}\times 100\% \tag{3.18}$$

For hard spheres, various computer simulations show that a terminal size RSD, above which no crystallization can occur, is in the range of 5-15% of the average sphere diameter. For hard disks, this terminal value for 2D crystallization is 8% of the average disk radius [95–97] Since the mass of a sphere is proportional to its radius cubed ($m \sim r^3$) and the mass of a disk is proportional to the square of its radius ($m \sim r^2$), the relative standard deviation for the radius (RSD_r) can be calculated as $0.33\,\mathrm{RSD}_m$ and $0.5\,\mathrm{RSD}_m$, for the spherical and disklike conformations, respectively. Therefore, for the compressed linear brush (PDI$=1.15$, $\mathrm{RSD}_m = 39\%$) one obtains $\mathrm{RSD}_r = 13\%$, whereas the disklike conformation of the four-arm brush (PDI $= 1.04$, $\mathrm{RSD}_m = 20\%$) gives $\mathrm{RSD}_r = 10\%$. Since both values are higher than the 8% terminal RSD, one should not observe long-range hexagonal order for either linear or four-arm brushes. Although the ordering theories lend insight into the reason for increased orientational ordering with the four-arm brushes, the compressed polymer molecules cannot be regarded as hard objects. The

ordering behavior of the soft brushlike objects needs further in-depth investigation.

Conclusions

AFM combined with LB proves a useful technique for the determination of molecular weights and polydispersities of polymers with complicated architecture, such as multiarm brush polymers. The technique also makes it possible to observe and quantitatively analyze the ordering of brush monolayers. Lateral compression of the starlike brushes caused a transition from an extended dendritic-like conformation to a compact disklike conformation. Once the molecules transform from an extended to a disklike conformation, they also gain local hexagonal order stabilized by steric repulsion of adsorbed side chains. The orientational order of starlike brush molecules in a compressed monolayer increases with decreasing polydispersity as predicted by theory.

3.3.4 Adsorption induced scission of carbon-carbon bonds

Covalent carbon-carbon bonds are hard to break. Their strength is evident in the hardness of diamonds [98, 99] and tensile strength of polymeric fibres [100–103]; on the single-molecule level, it manifests itself in the need for forces of several nanonewtons to extend and mechanically rupture one bond. Such forces have been generated using extensional flow [104–106], ultrasonic irradiation [107], receding meniscus [108] and by directly stretching a single molecule with nanoprobes [109–113]. Here we show that simple adsorption of brush-like macromolecules with long side chains on a substrate can induce not only conformational deformations [114], but also spontaneous rupture of covalent bonds in the macromolecular backbone. We attribute this behaviour to the fact that the attractive interaction between the side chains and the substrate is maximized by the spreading of the side chains, which in turn induces tension along the polymer backbone. Provided the side-chain densities and substrate interaction are sufficiently high, the tension generated will be strong enough to rupture covalent

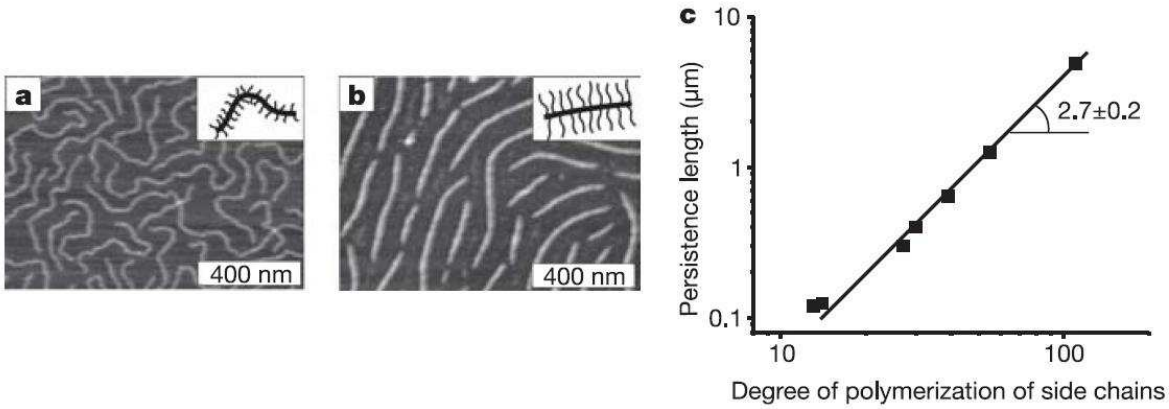

Figure 3.17: Conformational response of pBA brush-like macromolecules to adsorption on mica. The conformation of the macromolecules is visualized by AFM, with the light threads in the height images shown in a and b corresponding to the backbones. The areas between threads are covered by side chains, which cannot be visualized at this scale. With increasing sidechain length, molecules change from a fairly flexible conformation for $n = 12$ (shown in a) to a rod-like conformation for $n = 130$ (shown in b). c, The persistence length l_p of the adsorbed macromolecules was determined from the statistical analysis of the backbone curvature. It is found to increase with the side chain length as $l_p \propto n^{2.7}$.

carbon-carbon bonds. We expect similar adsorption-induced backbone scission to occur for all macromolecules with highly branched architectures, such as brushes and dendrimers. This behaviour needs to be considered when designing surface-targeted macromolecules of this type either to avoid undesired degradation, or to ensure rupture at predetermined macromolecular sites.

A series of brush-like macromolecules with the same number average degree of polymerization of a poly(2-hydroxyethyl methacrylate) backbone, $N_n = 2,150 \pm 100$, and different degrees of polymerization of poly(*n*-butyl acrylate) (pBA) side chains ranging from $n = 12 \pm 1$ to $n = 140 \pm 12$ were synthesized by atom transfer radical polymerization (see Polymer Characterization in the Methods) [72]. Owing to the high grafting density, the side chains repel each other and thereby stretch the backbone into an extended conformation. Placing these macromolecules on a surface enhances the steric repulsion between the side chains, which results in both an extension of the polymer backbone and an increase of the persistence length.

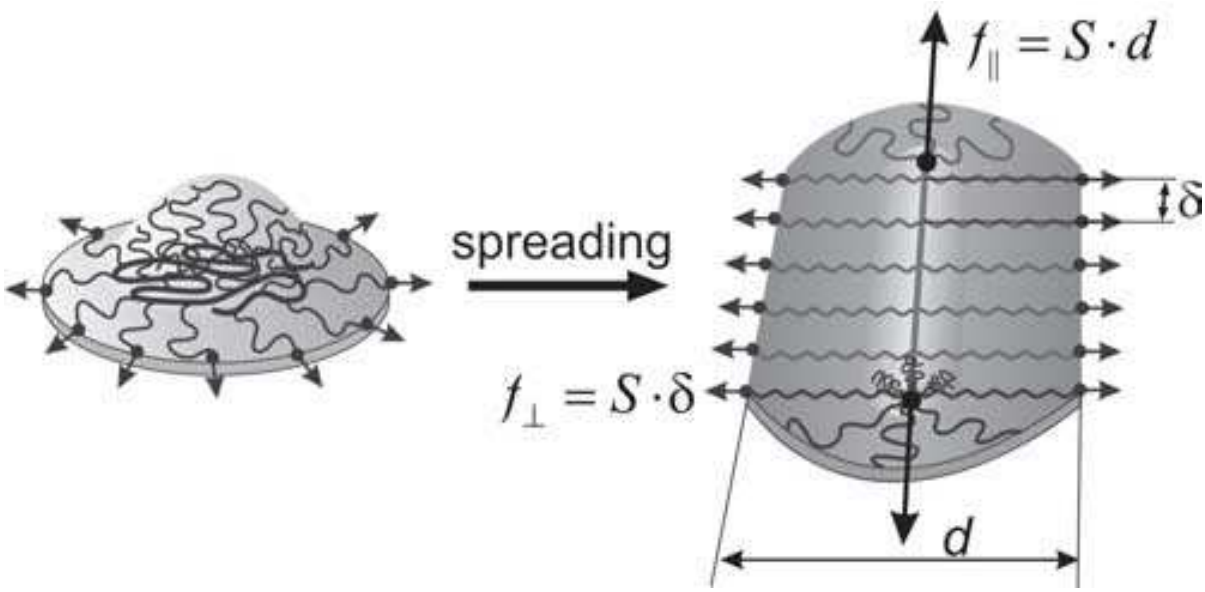

Figure 3.18: Schematic of the spreading of a brush-like macromolecule on an attractive substrate. After adsorption, the macromolecule spreads to increase the number of monomeric contacts with the substrate. The brushlike architecture imposes constraints on the spreading process making it anisotropic and leading to extension of the backbone. Along the brush axis, the wetting-induced tensile force $f \cong S \cdot d$ is supported almost entirely by the covalently linked backbone, where S is the spreading coefficient and d is the brush width. In the direction perpendicular to the backbone, the force is evenly distributed over many side chains, each bearing a $f \cong S \cdot \delta$ tensile force, where δ is the distance between the neighbouring side chains.

The effect is illustrated in Fig. 3.17, which shows atomic force microscopy (AFM) micrographs of monolayers of pBA brushes with short (Fig. 3.17a) and long side chains (Fig. 3.17b). Measurements on both types of molecules yielded a number average contour length per monomeric unit of the backbone of $l = L_n/N_n = 0.23 \pm 0.02nm$ (see Atomic Force Microscopy in Methods), which is close to $l_0 = 0.25nm$, the length of the tetrahedral C–C–C section. This means that even for short side chains ($n = 12$), the backbone is already fully extended and adopts an all-*trans* conformation. As the side chains become longer, we observe global straightening of the backbone reflected in the increase of the persistence length (Fig. 3.17c).

Chain extension requires a substantial amount of force, which we estimate using simple spreading arguments (Fig. 3.18). Just as in normal liquids, the polymeric side chains spread to

cover the higher-energy substrate and thus stretch the macromolecule in all directions.Unlike conventional liquids, however, the spreading of the side chains is constrained by their connection to the backbone. To maximize the number of side chains that adsorb to the substrate, the backbone needs to extend; but even when it is fully elongated, about 50% of the side chains are still not fully in contact with the substrate. In this situation, the attraction of the side chains for the surface causes the polymer backbone to extend beyond its physical limit. Here it is important that the tension imposed by the surface attraction is unevenly distributed over the covalent bonds of the molecular skeleton.

As shown in Fig. 3.18, along the brush axis, a major fraction of the wetting-induced tensile force is carried by the backbone; while in the perpendicular direction, the tension is evenly distributed over many side chains. The force at the backbone is estimated as $f \cong S \cdot d$; where S is the spreading coefficient and d is the width of adsorbed brush macromolecules (Fig. 3.18). Here, we consider only the dominant term in S: that is, the difference between the surface free energies of substrate-gas, liquid-gas, and substrate-liquid-gas interfaces ($S = \gamma_s - \gamma_l - \gamma_{sl}$): Previous measurements for the substrates that were used in this study found $S \cong 20\,mN\,m^{-1}$ on graphite [70] and water/alcohol mixtures [114]. Therefore, a brush macromolecule with short side chains ($n = 12$) and a width of $d = 11nm$ (ref. [115]), is capable of generating a force of approximately $220pN$ on either of these two substrates. This exceeds the typical range of tensile forces of $10 - -100pN$ reported for stretching of individual polymer chains [116].

According to these arguments, the force value is proportional to the molecules width and also depends on the surface energy of the substrate. We therefore synthesized pBA brushes with longer side chains ($n = 140$) that would lead to a width of $d = 130nm$ (refs [52, 115]; this should result in a tensile force of about $2.6nN$ and allow us to challenge the carbon–carbon bonds in the backbone [106]. The molecules were adsorbed on the surface of mica, graphite, silicon wafers and a range of water/propanol mixtures. Whereas molecules on solid substrates could be directly imaged by AFM, the liquid-supported films were first transferred onto a solid

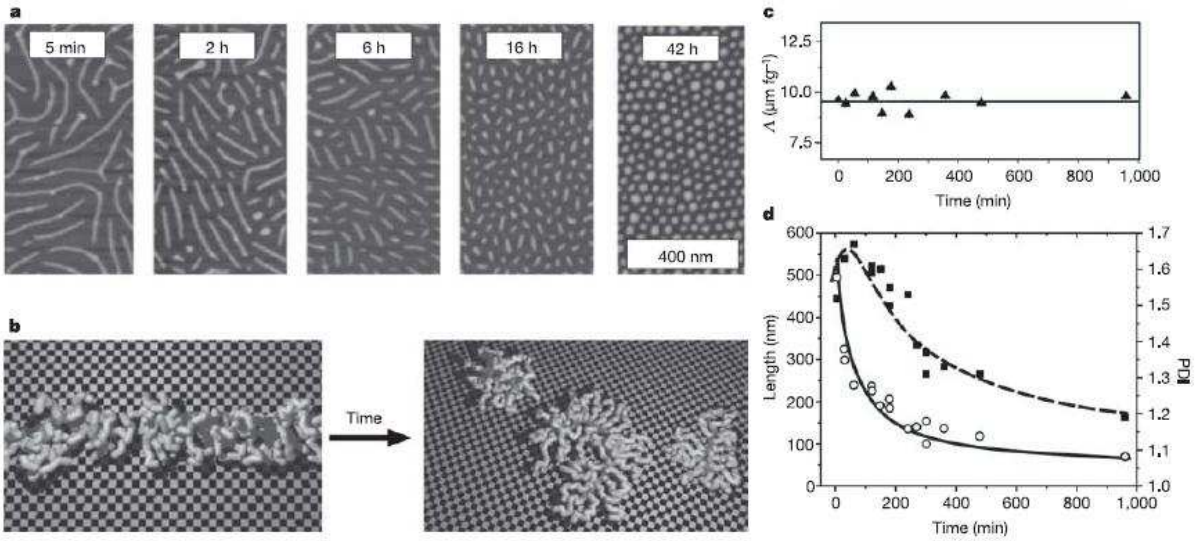

Figure 3.19: Adsorption-induced degradation of macromolecules. a, The molecular degradation of brush-like macromolecules with long side chains ($n = 140$) on mica was monitored using AFM height imaging after each sample was exposed for different time periods (as indicated in the images) to a water/propanol (99.8/0.2wt/wt%) substrate. b, Schematics of an adsorbed macromolecule (left) which undergoes spontaneous scission of the covalent backbone (right). Side chains are shown in light grey, the backbone in dark grey. c, The cumulative length per unit mass, measured within an area of $A = 25\mu m^2$ at a constant mass density of $\sigma = 0.08\mu g cm^{-2}$, was found to stay at an approximately constant value of $\Lambda = 9.6 \pm 0.5 \mu m fg{-}1$ throughout the scission process. d, The number average contour lengths measured after different exposure times t (white circles) are fitted according to $\frac{1}{L-L_\infty} = \frac{1}{L-L_0} + \frac{kt}{L_\infty}$, using experimental values for L_0 and L_1 and a fitted value for k of $2.3 \times 10^5 s^{-1}$ (solid line). The experimentally determined polydispersity index PDI = L_w/L_n (black squares) shows good agreement with the computer simulation results of Fig. 3.20 (dashed line).

substrate using the Langmuir-Blodget technique and then scanned by AFM (see Methods).

Figure 3.19a shows a series of AFM images obtained for different incubation times on the water/propanol (99.8/0.2 wt/wt%) substrate, which has a surface energy of $\gamma_s = 69 \pm 1 mN m^{-1}$ and a spreading parameter of $S = 21 \pm 2 mN m^{-1}$; where the experimental errors are determined by the precision of the Wilhelmy plate method (see Langmuir-Blodget monolayers in the Methods). As the time spent on the substrate increases, the molecules get progressively shorter while their number density (number of molecules per unit area) correspondingly increases; this suggests scission of the backbone (Fig. 3.19b). The cumulative length of molecules per unit mass

of the material was measured as $\Lambda = \frac{\sum L_i \cdot n_i}{\sigma \cdot A}$, where n_i is the number of molecules of length L_i within a substrate area A and σ is the Langmuir-Blodget-controlled mass per unit area of the monolayer. As shown in Fig. 3.19c, the cumulative length remains approximately constant for different exposure times, supporting the idea that chain scission occurs. Similar observations were made on other substrates (Fig. 3.21). However, we focused on experiments using liquid substrates because they allow gradual variation of the surface energy simply by mixing two different liquids, and because they facilitate rapid equilibration of the monolayer structure. Both factors ensure reproducibility of the kinetics study discussed below.

Figure 3.19d shows the characteristic decay of the average molecular length with increasing exposure time of the macromolecules to the water/propanol substrate. To analyse the kinetics of the scission process we assume that the bond scission occurs as a first-order reaction: $B = B_0 e^{-kt}$, where B is the total number of covalent bonds in all backbones within a unit area of the substrate, B_0 is the initial number of bonds at $t = 0$, and k is the rate constant. Because the cumulative length is conserved, we can obtain the number average contour length L from $\frac{1}{L-L_\infty} = \frac{1}{L-L_0} + \frac{kt}{L_\infty}$, where $L_0 = 496 \pm 18nm$ is the initial contour length measured by AFM at $t = 0$ and $L\infty = 40 \pm 3nm$ is the length of the shortest molecule observed during the scission process (see Atomic Force Microscopy in the Methods). Fitting the experimental data to this equation using k as a fitting parameter yielded $k = 2.3 \times 10^{-5} s^{-1}$. That we did not observe molecules shorter than 40nm even at very long exposure times is because the brush molecules with short backbones adopted star-like morphologies. This ensures that the side chains have more space to spread out and eases tension at the backbone. The reduction of tension prevents further scission, so the above rate equations are applied only at $L \geq L_\infty$.

The scission process seems random, which suggests a uniform distribution of tension along the backbone. We probe this assumption by analysing the length distribution of the system throughout the scission process. As shown in Fig. 3.19d, the polydispersity index, PDI = L_w/L_n; initially increases and then decays, where L_w and L_n are the weight and number aver-

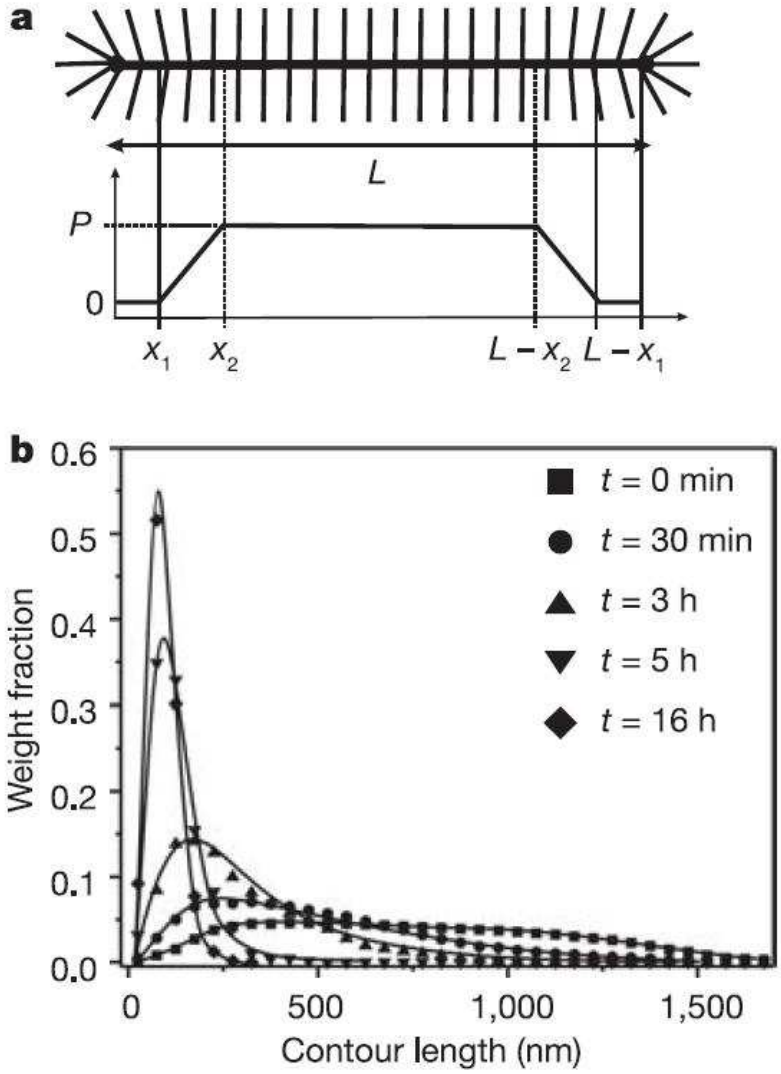

Figure 3.20: Computer simulation of the scission process. a, The computer model assumes a constant scission probability P along most of the backbone; at the ends, P decays linearly to zero from $x_2 = 120$nm to $x_1 = 40$nm. This ensures the scission process stops at the experimentally observed $L_\infty = 40$nm. b, Length distributions obtained by computer simulation for different time intervals t of the scission process (solid lines). The simulated distributions show good agreement with the distributions (data points) obtained by AFM on the same polymer/substrate system as used to obtain the images shown in Fig. 3.19a. The distributions are presented as the weight fraction of polymer chains of a certain number average contour length-with a resolution (bin size) of 50 nm. The initial distribution function exactly corresponds to a realistic ensemble of 2,450 molecules acquired by AFM at $t = 0$ with $L_n = 496$nm and PDI = 1.52.

age lengths of adsorbed macromolecules, respectively. This is consistent with random cleavage of backbone C–C bonds, which initially increases the length polydispersity and then results in an almost monodisperse system as the macromolecules gradually convert into short brush molecules that can no longer undergo scission. This behaviour can be simulated using a simple model wherein the probability P of bond scission occurring at any point along the backbone, except at the ends, is the same (Fig. 3.20a). Solid lines in Fig. 3.20b depict length distributions obtained at different durations of the computer-simulated scission process compare favourably with the corresponding length distributions measured by AFM (data points in Fig. 3.20b), giving good agreement between the modelled and experimentally measured polydispersity index. The simulated scission process eventually stops when all molecules become shorter than 80 nm, that is, in the range from $x_1 = 40nm$ and $2x_1 = 80nm$.

Experiments are also being conducted to verify the effects of the substrate surface energy and the side-chain length on scission. As might be expected, preliminary findings show that backbone scission is very sensitive to small variations in both parameters. If surface energy is decreased to below $60 mN\,m^{-1}$ by adding more propanol to the water/propanol mixture used as substrate, molecules with long side chains ($n = 140$) that readily break on a 99.8/0.2 wt/wt% water/propanol surface ($\gamma = 69\,mN\,m^{-1}$) remain intact. Sharp retardation of the scission process was also observed upon shortening of the side chains: when using the same substrate (that is, a 99.8/0.2 wt/wt% water/propanol mixture) but pBA brush-like molecules with $n = 130$ ($d = 120$) instead of $n = 140$ does not lead to any noticeable shortening within reasonable experimental times (for example, days). However, we found that these molecules break on graphite, which has a slightly higher surface energy and a spreading parameter (Supplementary Fig. 3.21).

The essential feature of the bond scission observed here is that it occurs spontaneously upon adsorption onto a substrate. Linear and weakly branched polymer chains are obviously not at risk of chemical degradation upon surface adsorption; but all highly branched macromolecules

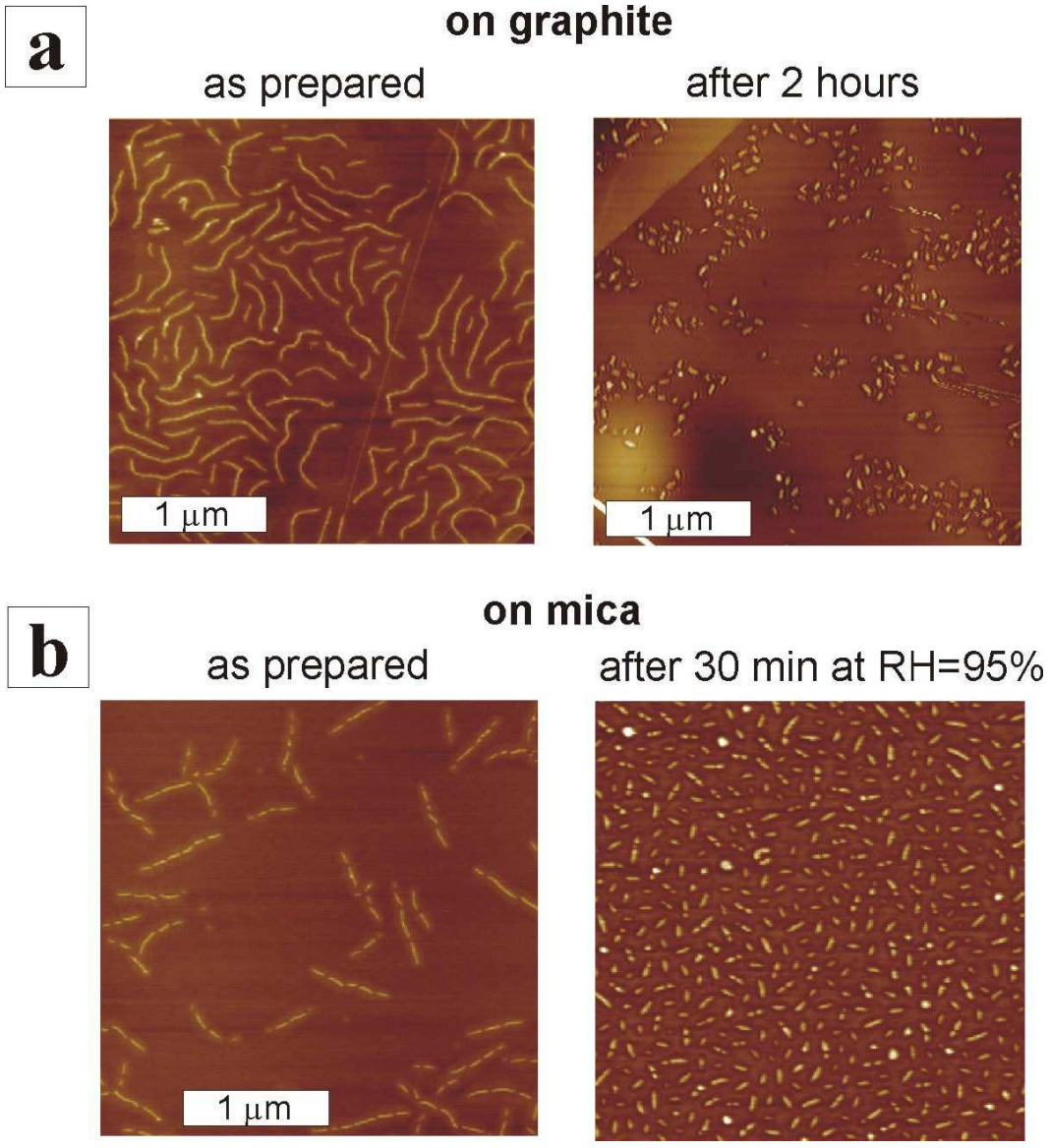

Figure 3.21: (a) On the surface of highly-oriented pyrolytic graphite, PBA brush-like macromolecules with long side chains (n=130) were found to slowly break with time at ambient conditions. The graphite has a surface energy of $\gamma_s = 80 \pm 10 mJ/m^2$ and a spreading parameter of $S = 23 \pm 3 mN/m$, where the uncertainties encompass the literature data. (b) PBA brush-like macromolecules with slightly longer side chains (n=140) break instantaneously on mica. The scission-caused undulations are clearly seen in the as-prepared sample (left). However, one needs to expose the sample to water vapour to reduce friction at the substrate and allow the sliding of the scission products away from each other (right). Since in both experiments we do not control the surface coverage, the cumulative length per unit mass of the material can not be compared.

that physically cannot allow all their monomeric units to interact with a substrate will be susceptible. In such cases, the load imposed by the adsorption forces is unevenly distributed over different structural elements of the molecular architecture according to the branching topology. In the system we studied, tension is concentrated along the backbone of molecular brushes and can be enough to break covalent carbon-carbon bonds. In the case of regular dendrimers, tension will focus at the covalent bonds near the principal branching centre of the dendrimers and, if the adsorption forces are strong enough, can cause the dendrimers to break. This essentially geometric effect is closely related to the observation that dendrimer polymerization stops above a certain generation, owing to the overcrowded molecular volume [117]. These steric constraints can be eased by increasing the length of the spacer between branches in dendrimers, and between side chains in cylindrical brushes.

However, these structural modifications that make the branched structure looser also increase the footprint of the adsorbed macromolecule, which in turn leads to a greater tensile force. Thus, with the current pursuit of new macro- and supramolecular materials that are specifically tailored for various surface applications, the surfaceinduced scission of covalent bonds will need to be considered carefully when designing complex molecular architectures. But in addition to emphasizing the need for designing stress-free macromolecules for some applications, the phenomenon described here also opens up intriguing opportunities for deliberately designing architectures that break at pre-defined sites.

Methods

Polymer characterization. Average molecular weights and molecular weight distribution of brush-like macromolecules were measured by gel permeation chromatography (GPC) equipped with Waters microstyragel columns (pore sizes 10^5, 10^4 and 10^3 Å) and three detection systems: a differential refractometer (Waters Model 410), multi-angle laser light-scattering (MALLS) detector (Wyatt, DAWN EOS), and a differential viscometer (WGE Dr. Bures, η-

1001). In addition, we used a newly developed approach based on a combination of AFM and Langmuir-Blodget techniques [53]. This combination of methods ensured relative experimental errors in determining the polymerization degrees of the backbone and side chains below 5% and 10%, respectively.

Langmuir-Blodget monolayers. To study the kinetics of the scission process, brush-like macromolecules with pBA side chains were adsorbed onto a surface of a water/propanol (99.8/0.2 wt/wt%) substrate. Propanol was chosen for its low surface energy and because its vapour pressure is nearly equivalent to that of water. This was necessary for long incubation times so that any subphase evaporation would lead to a minimal change in the surface energy. The evaporation of the subphase was closely monitored and controlled in an environmental chamber. ForAFManalysis, the monolayer films were transferred onto a mica substrate at a controlled transfer ratio of 0.98, using the Langmuir- Blodget technique. The surface tension of the substrate and the corresponding spreading parameter were measured by the Wilhelmy plate method.

Atomic force microscopy. Topographic images of individual molecules were collected using an atomic force microscope (VeecoMetrology Group) in tapping mode. We used silicon cantilevers (Mikromasch-USA) with a resonance frequency of about 140 kHz and a spring constant of about 5Nm. The radius of the probe was less than 10 nm. The analysis of digital images was performed using a custom software program (PEN) developed in-house and available from S.S.S. The program identifies the molecular contour and is capable of determining the contour length, the end-to-end distance, and the curvature distribution, all required for evaluation of the persistence length. For every sample, about ten images of about 300 molecules, that is, a total of 3,000 molecules were measured to ensure a relative standard error below 4% and an experimental error below 5% of the persistence length (Fig. 3.17), contour length, and polydispersity index (Fig. 3.19) measurements.

3.3.5 Molecular motion in a spreading precursor film

Quite often we see a liquid drop spreading on a solid surface to give a thin film of finite thickness. This everyday phenomenon plays a key role in many important processes, such as oil recovery, lubrication, painting, and mass transport through the lung airways. The macroscopic behavior of spreading drops is well understood [118, 119] yet our understanding of the molecular mechanism of spreading remains incomplete and controversial [120–122]. This lack of microscopic knowledge is now an urgent problem limiting development in microfluidic devices and nanoscale machines, whose characteristic time and length scales are approaching those of individual molecules. Here we report on molecular visualization of the spreading process of polymer-melt drops. For the first time, it is possible to measure simultaneously the displacement of the contact line and displacements of individual molecules within the precursor film. The masstransport mechanism was clearly identified as plug flow, i.e., collective sliding of polymer chains with an insignificant contribution from the molecular diffusion.

The spreading of a drop begins with the formation of a thin precursor film [123] [Fig. 3.22(a)]. This is then followed by a macroscopic drop which has a terraced foot assigned to concurrent sliding of monolayers stacked on top of one another [124, 125]. Unlike the drop radius, which follows the Hoffman-Tanner relation $R(t) \sim t^{1/10}$, the precursor-film length obeys the diffusionlike law $L(t) \sim \sqrt{t}$. Both the precursor film and the molecular terraces belong to the generic features of spreading observed by ellipsometry for different types of fluids [125–128]. However, because of low resolution ($\sim 30\mu m$) ellipsometry fails to resolve questions on the mechanisms of mass transport and energy dissipation in the liquid layers. The unique advantage of atomic force microcopy (AFM) is that it allows visualization of molecules [52, 56, 129, 130]. Although this advantage was immediately recognized, the first AFM measurements of spreading drops did not attain molecular resolution [131, 132]. Investigation of the molecular motion requires visualization of molecules both in space and in time. We solved this problem through the use of model brush molecules [Fig. 3.22(b)].

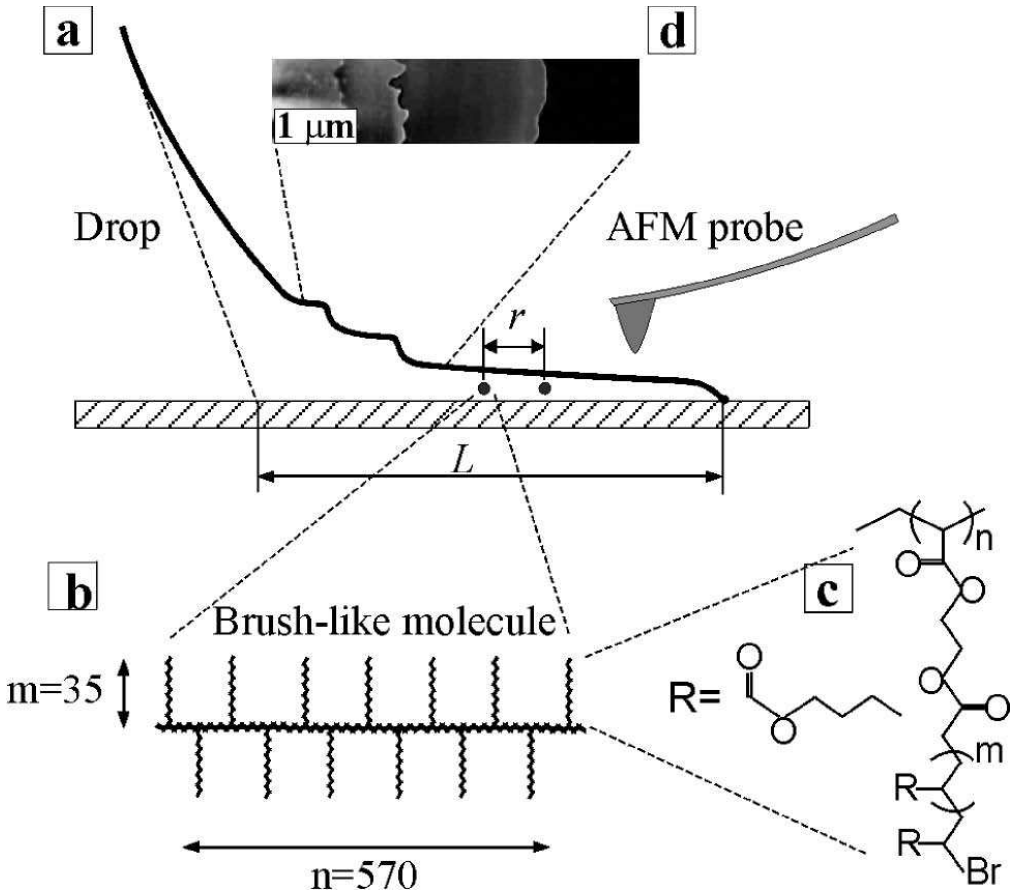

Figure 3.22: (a) A microscopic drop of a polymer-melt (volume $\sim 1nl$, radius $\sim 100\mu m$ was scanned by AFM to measure the displacement L of the precursor-film edge and the distance r between the molecules within the film. The polymer melt is composed of (b) cylindrical brush molecules with (c) poly(*n*-butyl acrylate) side chains. (d) At later stages of spreading on mica one observed monolayer terraces at the foot of the drop with a thickness of $5\,nm$.

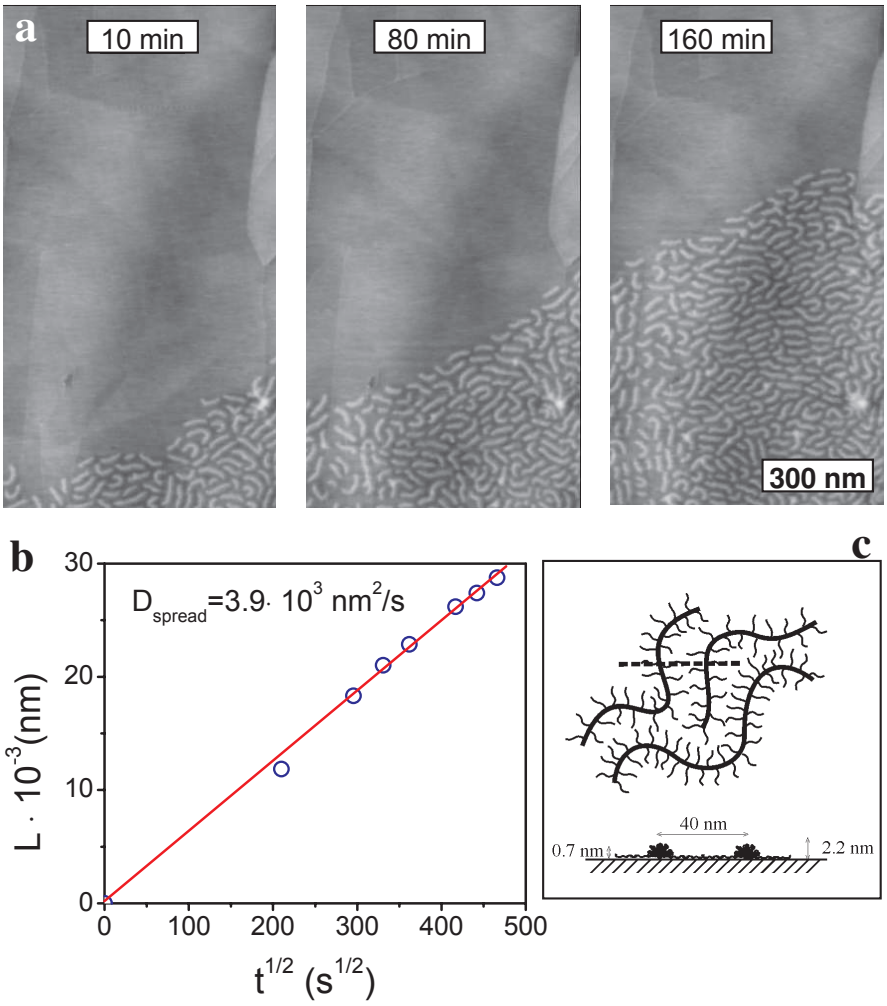

Figure 3.23: (a) AFM monitors sliding of the precursor monolayer of PBA brushes on the HOPG surface. The images were captured at different spreading times: 10, 80, and 160 min. (b) Mean displacement of the film edge gives the spreading rate $D_{spread} = (3.9 \pm 0.2) \times 10^3 nm^2/s$. (c) The cartoon shows organization of brush molecules within the monolayer. Backbones with a ridge of desorbed side chains provide height contrast, while the spacing between the molecules is determined by adsorbed side chains.

The model properties of cylindrical brushes are associated with densely grafted side chains that aid in the visualization process in four ways. First, adsorbed side chains separate the molecular backbones. Depending on the side-chain length and the grafting density, the intermolecular distance varies from 5 to 60 nm [52]. Second, because of the high grafting density there is a fraction of side chains that aggregate along the backbone above the substrate plane [54] [Fig. 3.23(c)]. The ridge of the desorbed side chains provides height contrast. Third, the repulsion of the adsorbed side chains increases the stiffness of the backbone. Depending on the side-chain length, the apparent persistence length ranges from 10–500 nm [52] enabling measurements of molecular curvature. Fourth, the number of monomeric contacts with the substrate (per unit length of the backbone) increases with the side-chain length and the grafting density. This depresses mobility of adsorbed molecules and facilitates their temporal resolution.

In this work we studied brush molecules with a polymethacrylate backbone and of poly(*n*-butyl acrylate) (PBA) side chains [Fig. 3.22(c)] prepared by atom transfer radical polymerization [72]. The number of the average degree of polymerization of the backbone is $n = 570 \pm 50$, the side chains have a degree of polymerization of $m = 35 \pm 5$, and the grafting density is 1; i.e., every monomeric unit of the backbone contains one side-chain. A drop of PBA brushes (volume $\sim 1nl$, radius $\sim 100\mu m$) was deposited on the surface of highly oriented pyrolytic graphite (HOPG) at a controlled relative humidity of 25% and a temperature of $25^{\circ}C$. At room temperature, the material is liquid ($T_g = -50^{\circ}C$) with a zero-shear viscosity $\eta_0 = 8340 Pa \cdot s$. Once the drop touched the substrate, a thin precursor film was observed growing from the foot of the drop. In addition, monomolecular terraces developed at the foot of the drop [Fig. 3.22(d)]; as many as 6 terraces were detected consistent with the terraced droplet model [124]. The motion of the terraces is the subject of ongoing research, while this work is focused on the precursor film.

The motion of the precursor film was monitored by AFM in different regions of the pre-

cursor film located along different radial directions with respect to the drop center. In total, ten drops were studied to ensure reproducibility and accurate data averaging. Figure 3.23(a) shows three snapshots captured at the edge of the growing film. The important outcome of this experiment is the simultaneous observation of both the displacement of the film edge and the motion of individual molecules within the film. The time dependence of the film length in Fig. 3.23(b) obeys the diffusionlike law $L(t) = \sqrt{D_{spread}t}$ at a spreading rate of $D = (3.9 \pm 0.2) \times 10^3 nm^2/s$.

In addition to the film displacement, the AFM images provide information on the molecular structure of the precursor film. Each brush molecule is visualized as a flat wormlike object with a thickness of $h = 0.7 - 2.2nm$ and a width of $d = 40 \pm 3nm$ [Fig. 3.23(c)]. The $0.7 \pm 0.1nm$ thickness corresponds to the area between the backbones which is covered by adsorbed side chains, while the $2.2 \pm 0.2nm$ thickness is measured at the ridge of desorbed side chains. By analyzing an ensemble of 300 molecules, we determined a number average contour length of $L_n = 105 \pm 5nm$ and a polydispersity index of $L_w/L_n = 1.17$. From the backbone curvature [56] we determined a persistence length of $l_p = 112 \pm 10nm$. Since $l_p \cong L_n$,one deals here with wormlike molecules.

Through use of AFM we also were able to monitor temporal changes in position, orientation, and conformation of individual molecules [Fig. 3.24(a)]. We monitored a group of 100 molecules to record the coordinates of the center of mass of the group $R_{cm}(t)$ along with the coordinates of the individual molecules $R_i(t)$ and $r_i(t) = R_i(t) - R_{cm}(t)$ relative to the substrate and to the center of mass, respectively. Figure 3.24(b) depicts the trajectory of the center of mass and the trajectories of three molecules from the group. In the frame of the substrate, the trajectories demonstrate a convective flow along the spreading direction. However, in the frame of the precursor-film molecules move in a random-walk fashion which will be later identified as flow-induced diffusion. Figure 3.24(c) depicts the time dependence of the mean-square displacement $\langle r^2(t) \rangle = 4D_{induced}(t)$ with a diffusion coefficient of $D_{induced} = 1.3 \pm 0.1 nm^2/s$, which is 3 orders of magnitude lower than the spreading rate D_{spread} of the film edge. In

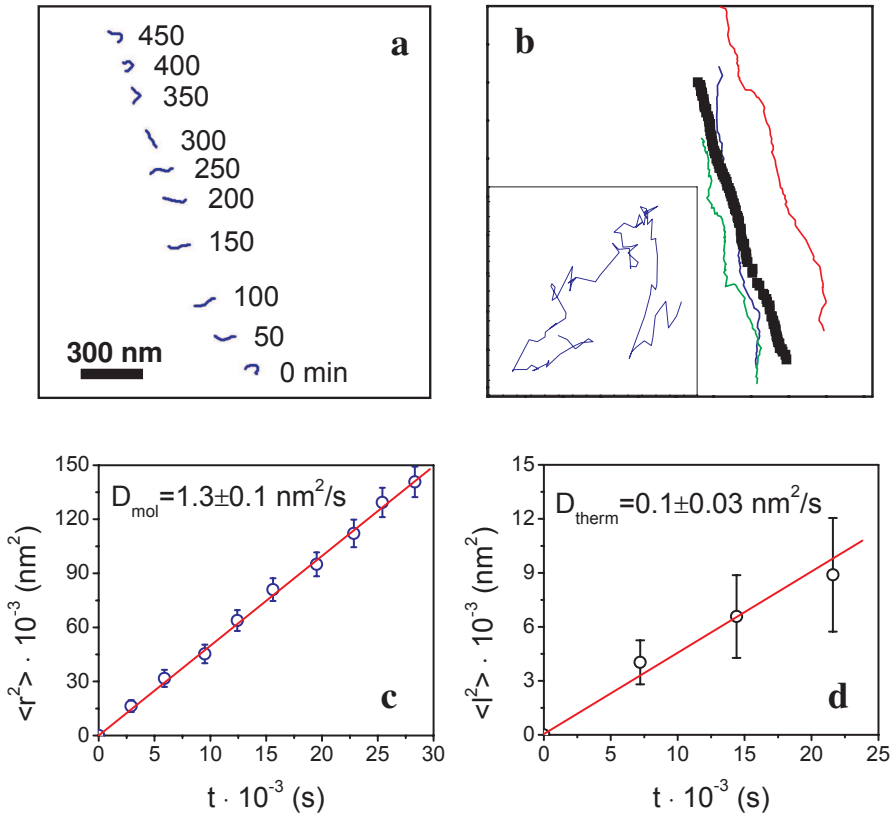

Figure 3.24: (a) Animation of one of the spreading molecules demonstrates different modes of the molecular motion including translation of the center of mass, chain rotation, and fluctuations in the backbone curvature. The numbers indicate the observation time during the spreading process. (b) The trajectories of the center of mass of a group of 100 molecules (bold line) along with individual trajectories of three molecules (thin lines). The inset shows the path of one of the molecules in the frame of the precursor film by plotting the molecular trajectory relative to the center of mass of the group. (c) Mean-square intermolecular displacement $\langle r^2 \rangle = 4D_{induced}t$ was averaged for 100 molecules to determine the molecular diffusion coefficient $D_{induced} = 1.3 \pm 0.1 nm^2/s$. (d) Translational diffusion of 80 single brush molecules was monitored by AFM via interruptive scanning to determine two diffusion coefficients $D_{therm} = 0.61 \pm 0.08 nm^2/s$ and $D_{therm} = 0.10 \pm 0.03 nm^2/s$ at 10-minute (□) and 2-hour (◯) intervals between the consecutive scans, respectively.

other words, during ∼1h individual molecules separate by a distance of 100nm (1 molecular size) as the film moves a distance of $\sim 3\mu m$ (30 molecular sizes). As such, the mass transport is identified as plug flow with insignificant contribution from the diffusive motion. Brush molecules also demonstrated rotational motion. The time correlation function of the end-to-end vector $u(t)$ follows the exponential decay $\langle u(t)u(0)\rangle \propto \exp(-t/\tau_r)$ with a rotational relaxation time of $\tau_r = 5.3\times 10^4$sec (∼10 h). Therefore, both the translation and rotation of brush molecules in the frame of the precursor film are much slower than the plug flow. The diffusive motions are consistent with the fluid nature of the precursor film; however, they cannot be ascribed to thermally induced self-diffusion. The weak contribution of the thermal diffusion to the spreading process became evident from the Brownian motion of single molecules prepared by adsorption from a dilute solution (HOPG-substrate, 25°C, 25% RH). In order to minimize the perturbations due to the AFM tip, the sample was scanned in the interruptive fashion over the course of several days, i.e., after capturing an image the scanning process was halted until it was time to capture the next image. Every subsequent frame was readjusted relative to stationary surface defects such as terraces and pits to eliminate the 100 nm/h thermal drift of the sample. A complete study of the molecular diffusion by AFM will be presented elsewhere. Here, Fig. 3.24(d) demonstrates two time dependences of the mean-square displacement $\langle r_0^2(t)\rangle = 4D_{therm}(t)$ measured at 10-minute and 2-hour intervals and resulted in two diffusion coefficients $D_{therm}t = 0.61\pm 0.08nm^2/s$ and $D_{therm} = 0.10\pm 0.03nm^2/s$, respectively. Since the interruptive scanning does not exclude the tip effect completely, the lower value is considered as an upper limit of the diffusion coefficient. In other words, without the tip-induced perturbations, molecules would move even slower ($D_{therm} \leq 0.10\pm 0.03nm^2/s$). The upper limit of the diffusion coefficient is relevant for the spreading kinetics as it gives a lower limit for the friction coefficient of a single PBA-brush molecule against the HOPG substrate as $\zeta_1 \geq (k_BT/D_{therm}) \cong 0.041\pm 0.013(Ns/m)$. This value can be used to verify the plug flow wherein the friction at the substrate is the dominant dissipation mechanism. For linear

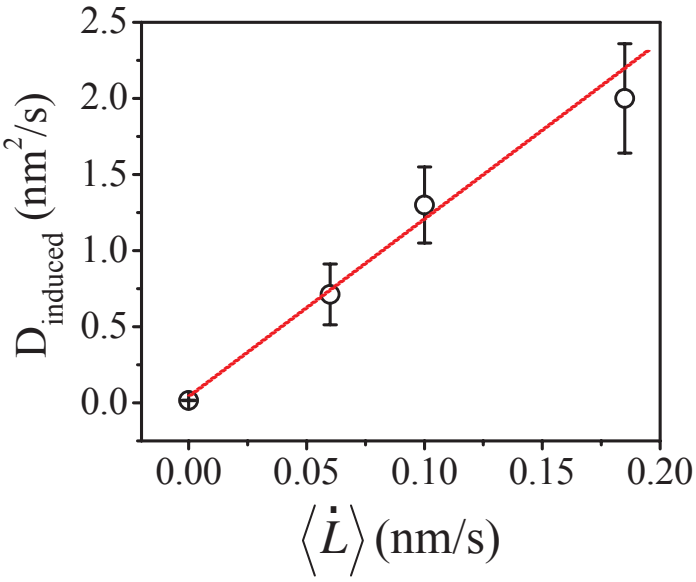

Figure 3.25: The translational diffusion coefficient $D_{induced}$ in the precursor film increases with the velocity of the film. This evidences the mechanically induced random-walk of molecules within the sliding film.

spreading*, one writes the energy balance as $L \cdot \dot{L} \cdot \zeta_1 \cong S_0 \Sigma$, where the left side represents the energy loss due to friction and the right side gives the energy gain due to spreading. Here, S_0 is the microscopic spreading parameter $\Sigma = 7500 \pm 200 nm^2$ is the averaged area per molecule, and $2L \cdot \dot{L} = D_{spread}$. For monolayers, S_0 depends on the film thickness and other molecular details that hinder its accurate evaluation [120]. For estimation purposes, we considered only the dominant term, i.e., the macroscopic spreading parameter S and set $S_0 \cong S$. Since mainly dispersion forces are involved in the interaction between the hydrocarbon polymer and the nonpolar substrate, $S \cong 2(\sqrt{\gamma_l^d \gamma_s^d} - \gamma_l)$ [133], where γ_l and γ_l^d are the surface energy and its dispersion component of PBA, and γ_s^d is the dispersion surface energy of HOPG. For the known $\gamma_l \cong 33 mJ/m^2$, $\gamma_l^d \cong 23 mJ/m^2$, and $\gamma_s^d \cong 80 \pm 10 mJ/m^2$, one obtains $S \cong 20 \pm 6 mJ/m^2$. This gives the molecular friction coefficient $\zeta_1 \cong (2S\Sigma D_{spread}) = 0.08 \pm 0.03 (Ns/m)$, which is consistent with the lower limit $\zeta_1 \geq 0.041 \pm 0.013 Ns/m$.

As was noted above, the upper limit of the selfdiffusion coefficient $D_{therm} < 0.10 \pm 0.03 nm^2/s$

*For radial spreading, one has to add a logarithmic prefactor.

is noticeably lower than $D_{induced} = 1.3 \pm 0.1 nm^2/s$ measured in the moving precursor film. This indicates that the diffusive motion in the precursor film has a different nature than the thermal diffusion of surface confined molecules and it is more likely induced by flow. This was verified by measuring the diffusion rate $D_{induced}$ as a function of film velocity at different stages of the spreading process. Figure 3.25 shows that the molecular diffusion coefficient increases linearly with the film velocity, i.e., $D_{induced} \sim \dot{L}$. The origin of the molecular motion in the precursor film is still a subject for debates. We believe that the random walk has its origin in random collisions of neighboring molecules as the dense monolayer is dragged over a solid substrate. This is reminiscent to the flow behavior of granular fluids for which an effective temperature can be calculated from the mechanically induced diffusion of particles [134–136]. Another explanation can be found in the heterogeneous structure of the substrate. Inevitable variations of the friction coefficient perturb the velocity field and thus cause collisions of spreading molecules leading to their diffusion. In order to check the effect of surface heterogeneities, we studied spreading on two HOPG substrates with different degrees of disordering due to the mosaic of monocrystal grains slightly disoriented with respect to each other: HOPG grade A with a mosaic spread of $0.4^\circ \pm 0.1^\circ$ and HOPG grade B with a mosaic spread $0.8^\circ \pm 0.2^\circ$. The diffusion coefficient on the more uniform HOPG-A was found to be significantly lower ($D_{induced} = 0.6 nm^2/s$ than on the HOPG-B with larger density of defects $D_{induced} = 1.3 nm^2/s$. This suggests that the substrate heterogeneity influences the diffusive motion of molecules in sliding monolayers.

In summary, this study shows that the mass transport in the precursor film is due to the plug flow of polymer chains on a solid substrate with minor contribution from molecular diffusion. The slow diffusion does not contradict with the liquid state of the studied polymer [137]. It merely shows that the spreading proceeds faster than the thermal diffusion of brush molecules. The fluid nature of the sliding monolayer was confirmed with the translational and rotational diffusion of molecules within the precursor film. However, this diffusion is not a spontaneous

one; it is induced by the sliding of a dense monolayer over a heterogeneous substrate.

3.3.6 Flow-enhanced epitaxial ordering

Thin films possessing long-range structural order on sub-100 nm length scales are vital for many technological applications such as magnetic recording [138] and optoelectronic [139] devices, molecular separation media [140], and liquid crystal displays [141]. Ordered structures can be prepared using lithographic techniques [142, 143] and external fields [144]. Ordering can also occur spontaneously upon adsorption of designed macromolecules (e.g., block copolymers) [145–150] and colloidal particles [151–153]. Self-organization of molecular and colloidal species can be further enhanced by specific interactions of the species with the underlying substrate through graphoepitaxy [154–158] and surface epitaxy [159–165] mechanisms. Yet, the short-range order of the self-organized films precludes them from many applications because their domain size is usually no more than hundreds of nanometers. Ordering of molecules and colloidal particles on a surface is retarded by the 2D confinement and friction against the substrate. This particularly impacts larger species that experience severe steric hindrance and stronger interaction with the substrate. Such behavior is disadvantageous, since large macromolecules and particles are very attractive building blocks due to their native sub-100 nm size and a well-defined shape. Therefore, researchers are continuously looking for new mechanisms that would increase the degree of order in thin films. Here we report on the significant enhancement of epitaxial alignment of brush-like macromolecules achieved during spreading of the monolayer film on the surface of highly oriented-pyrolytic-graphite (HOPG). Unlike conventional flow-induced orientation of anisometric objects such as rodlike particles, liquid crystal molecules, and semi-flexible polymer chains [166, 167], the observed molecular orientation is not coupled with the direction of flow. The role of the flow is merely to enhance diffusion and thus facilitate epitaxial ordering of the large macromolecules. These results were obtained using atomic force microscopy (AFM) which enabled real-time monitoring of the

spreading process on the molecular scale [70, 71].

Molecular tiles

Brush-like molecular architectures provide a powerful platform for construction of nanoscopic building blocks and devices [84, 86, 129, 168–173]. The size, shape, and physical properties of molecular brushes are well controlled by varying the length and grafting density of side chains [52]. Additional structure-control mechanisms emerge upon adsorption of brush molecules on the surface. Figure 3.26a shows a schematic structure of a brush-like macromolecule adsorbed on a flat substrate, which divides the side chains into two fractions: adsorbed side chains and desorbed ones. One can view this as a miniature rectangular shaped tile with a ridge of desorbed side chains along the longitudinal axes of the tile (Figure 3.26b). The side chains play three important roles in controlling the shape and packing of these molecular tiles on surfaces. First, the steric repulsion between the adsorbed side chains stretches the backbone. Through variation of the side chain length and grafting density, one can tune the two-dimensional persistence length from 10 to 5000 nm. This length is from 0.2 to 100 times larger than the persistence length of DNA ($\sim 50nm$) and approaches that of F-actin ($\sim 10\mu m$) measured in solution. Second, adsorbed side chains separate the molecules backbones. Depending on the side-chain length and the grafting density, the lateral size of the tile along with the intermolecular distance varies from 10 to 200 nm. Third, epitaxial adsorption of side chains onto a crystalline substrate causes alignment of the backbone and thus results in remarkable enhancement of the ordering length-scale. As shown in Figure 3.26b, the surface-mediated alignment of the relatively short side chains induces orientational order of much longer polymer backbones. There is also a fourth role which is vital to our experiments. The ridge of the desorbed side chains provides the height contrast that allows identification and visualization of individual molecules by AFM [54].

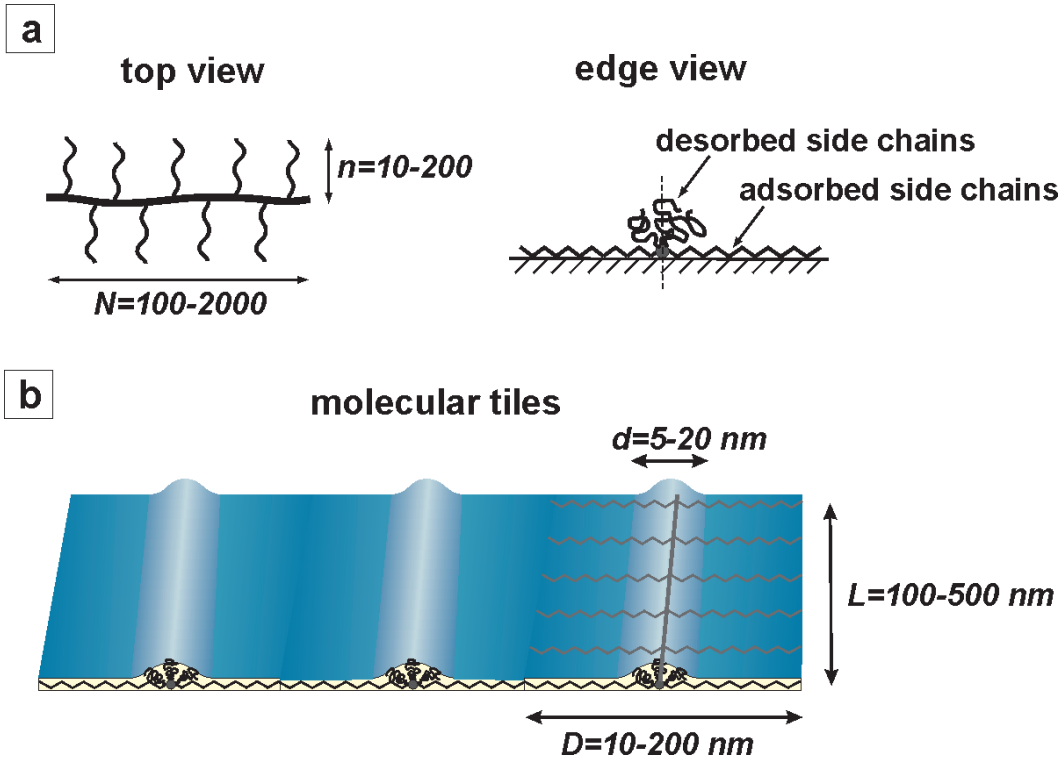

Figure 3.26: (a) Adsorption of brush-like macromolecules on surface results in partitioning of the side chains into two fractions: adsorbed and desorbed chains. Atom transfer radical polymerization allows precise control of the degree of polymerization of the backbone (N) and side chains (n) in a range of $N = 100 - 2000$ and $n = 10 - 200$, respectively. (b) The adsorbed molecular brushes can be viewed as miniature molecular tiles of a well-defined rectangular shape. Depending on the molecular dimensions, the length and width vary in a range of $L = 100 - 500$ nm and $D = 10 - 200$ nm, respectively, whereas the ridge of desorbed side chains is about 5-20 nm in width and 1-5 nm in height.

Materials and methods

Brush-like macromolecules consisting of polymethacrylate backbones and poly(*n*-butylacrylate) side chains were prepared by atomtransfer radical polymerization [72,85]. This polymerization technique allows precise control of the degree of polymerization of the backbone (N) and side chains (n) in ranges of $N = 100 - 2000$ and $n = 10 - 200$, respectively (Figure 3.26a). In this work, we studied brushes with $N = 570 \pm 50$, $n = 50 \pm 5$. At room temperature, the polymer is a viscous liquid with a zero-shear viscosity $\eta \approx 8340 Pa \cdot s$ and a glass transition temperature of $T_g \approx -50^{\circ}C$. The liquid nature of the material is essential as it allows for spontaneous spreading and molecular diffusion on surfaces.

We used three types of substrates: mica and two different grades of highly oriented pyrolytic graphite (HOPG). It is known that graphite induces epitaxial crystallization of alkanes and their derivatives due to close matching of the C-C-C length $l = 0.251nm$ and the crystallographic spacing of the HOPG lattice $a = 0.245nm$ [174]. Depending on the preparation conditions [175], HOPG substrates may contain different types of surface defects including dislocations, grain boundaries, folds, and terraces. To examine the effect of the surface heterogeneity on the molecular ordering, we used two grades HOPG with different degrees of disorientation of the *c*-axis of monocrystalline mosaic blocks (Figure 3.27a): grade A with a mosaic spread of $0.4^{\circ} \pm 0.1^{\circ}$ and grade B with a mosaic spread $0.8^{\circ} \pm 0.2^{\circ}$. As such, HOPG grade A is a more oriented substrate with less defects per unit surface area.

Monomolecular films of the polymers were prepared on mica and graphite using two techniques: (i) spincasting from solution and (ii) spontaneous spreading of polymer melt. In the latter case, small drops of PBA brushes (volume $\sim 1nl$, radius $\sim 100\mu m$) were deposited onto the substrate and allowed to spread for several hours under a controlled environment (air, $T = 25^{\circ}C$, RH = 50%). For the spreading experiments on mica, an environmental chamber was used to maintain high relative humidity (RH) ranging from 90 to 99%. The prepared films were imaged by tapping mode AFM (Multimode Nanoscope IIIa, Veeco Metrology Group)

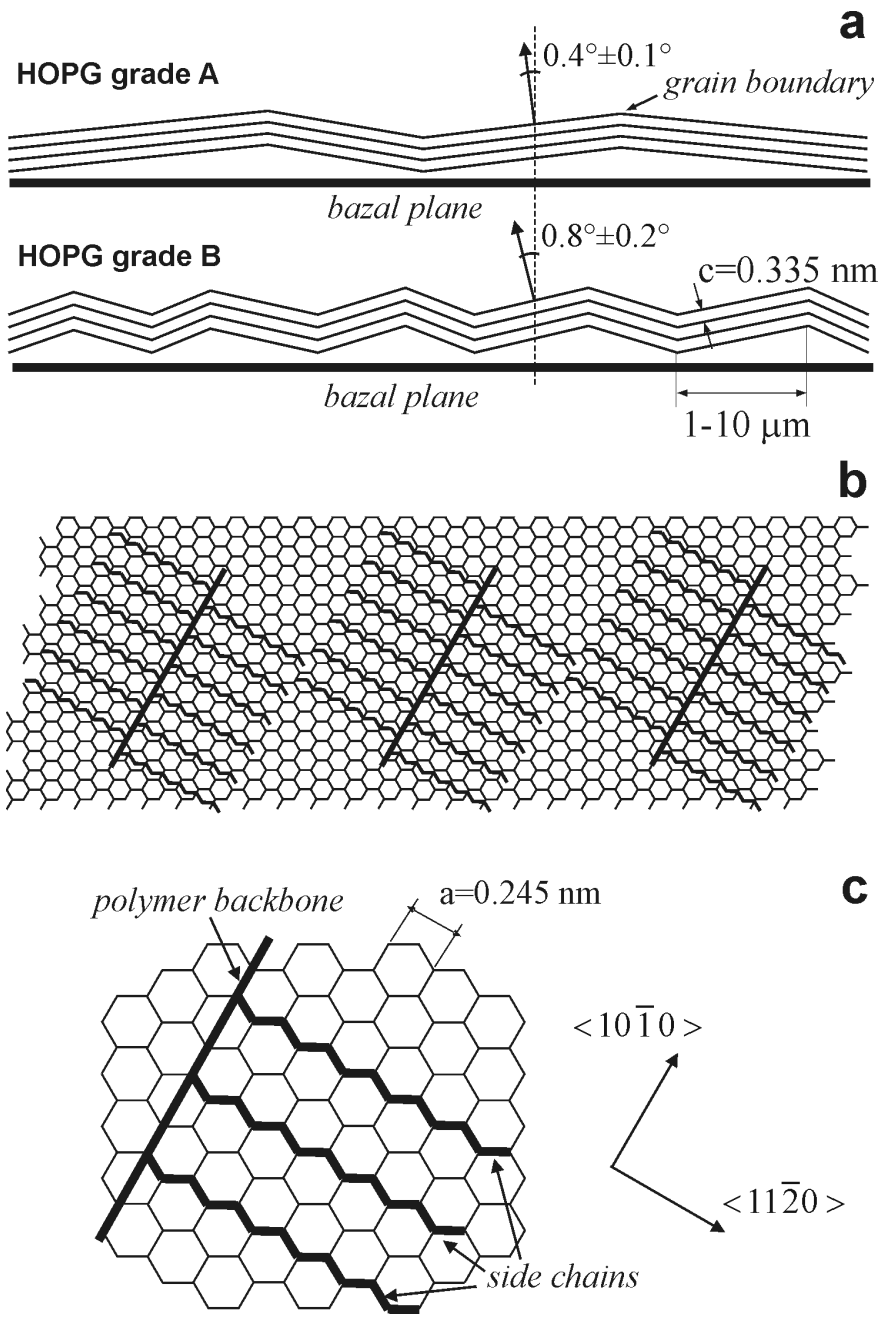

Figure 3.27: Schematic of the epitaxial adsorption of comblike molecules on graphite substrate: (a)HOPG substrates have a mosaic structure slightly disoriented mosaic blocks with a spread of the $\langle 0001 \rangle c$ axis of $0.4 \pm 0.1^\circ$ in grade A and $0.8 \pm 0.2^\circ$ in grade B; (b) Epitaxial adsorption of side chains leads to uniaxial alignment of polymer backbones along a particular crystallographic axis within the (0001) plane; (c) For example, if the side chains orient along the $\langle 11\bar{2}0 \rangle$ axis of the graphite lattice, this causes the backbone to orient along the $\langle 1\bar{1}0 \rangle$ axis.

using Si cantilevers (Mikromasch-USA) with a resonance frequency of about 140 kHz and a spring constant of about 5 N/m. The radius of the probe was measured to be less than 10 nm using a calibration standard [176].

Results and discussion

Molecular Ordering. Panels a and b of Figure 3.28 show molecular organization of the films prepared by spincasting on graphite and mica, respectively. The AFM height images show dense monolayers of wormlike macromolecules wherein the white threads correspond to the brush backbone and the area between the threads is covered by adsorbed side chains. Both on mica and graphite, the backbones of the adsorbed molecular brushes are almost fully extended showing the same value for a number average contour length $L_n = 125 \pm 8nm$. This gives the average length per monomeric unit $l = L_n/N_n = 0.23 \pm 0.02nm$ which is close to the monomer length $l_0 \cong 0.25nm$ in the fully extended all-trans conformation of the aliphatic backbone. In these images, one can also see small domains of uniaxially aligned molecules highlighted by dashed circles. The lateral size of the domains ranges from 100 to 600 nm with no visible indications of longrange molecular order. However, closer examination of the film structure on graphite (Figure 3.28a) reveals preferential orientation of the molecules along three axes as demonstrated by three distinct peaks in the angle distribution of molecular orientation (Figure 3.28c). The angle difference between the three peaks is approximately 120°, which is consistent with the 3-fold symmetry of the graphite (0001) surface [177]. In contrast, crystalline mica does not show any particular orientation (Figure 3.28b) resulting in random distribution of the angles (Figure 3.28d).

The orientational order of the brush-like macromolecules on the graphite drawn in Figure 3.27b is attributed to the well-known epitaxial adsorption of alkyl side chains on graphite along one of the three crystallographic axes of the (0001) surface [165, 178]. For example, this leads to alignment of the side chains along the $\langle 11\bar{2}0 \rangle$ axis of the graphite lattice which in

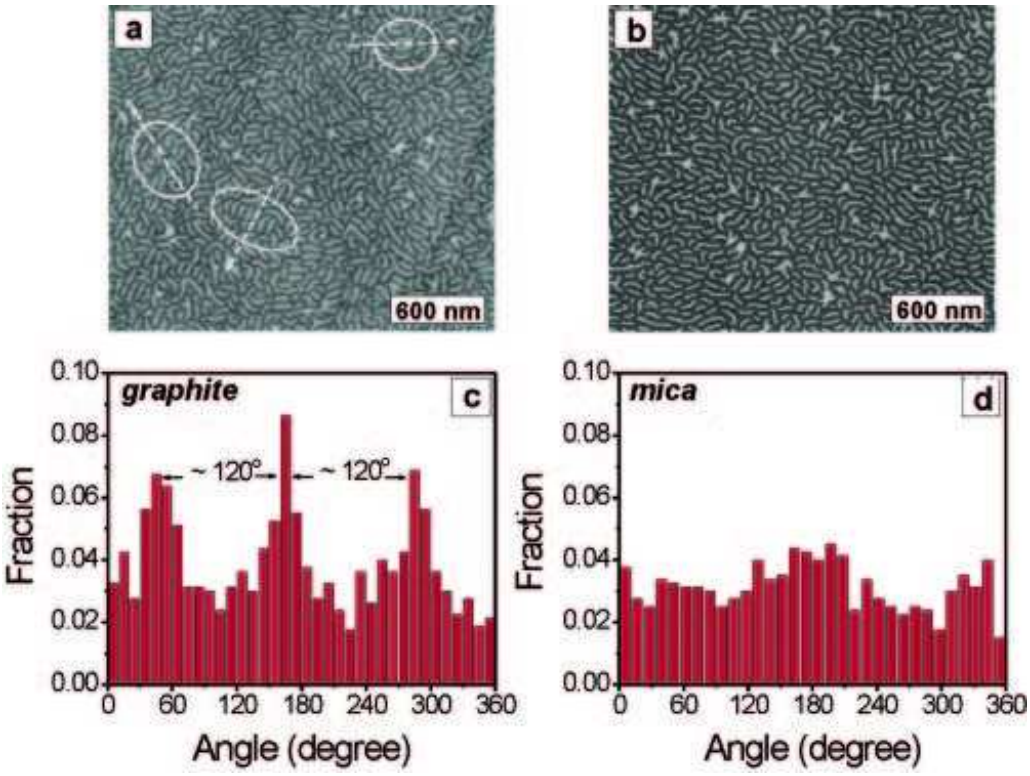

Figure 3.28: AFM was used to obtain height images showing molecular organization of spin-cast films of brush-like macromolecules on (a) graphite (grade A) and (b) mica substrates. The dashed circles and arrows in (a) highlight the ordered domains and their orientations; (c, d) angle distribution of molecules relative to the horizontal axis of the AFM images was measured on graphite and mica, respectively.

turns causes the backbone to orient along the $\langle 10\bar{1}0 \rangle$ axis (Figure 3.27c). The lack of such ordering on the mica surface is ascribed to a spatial mismatch between the mica lattice and molecular architecture. The disordered structure on mica could also be attributed to the thin layer of water that condensed from the surrounding atmosphere onto the hydrophilic surface of mica. [179] The water layer distorts epitaxial interactions between the crystalline mica and pBA side chains. Note that changing preparation conditions, such as annealing time, temperature, and solution concentration, did not improve molecular ordering either on graphite or mica substrates. Seemingly, thermal diffusion of the large macromolecules within dense monolayers is prohibitively slow and hinders the ordering process.

To enhance molecular motion, thin films were prepared by a different method: spreading

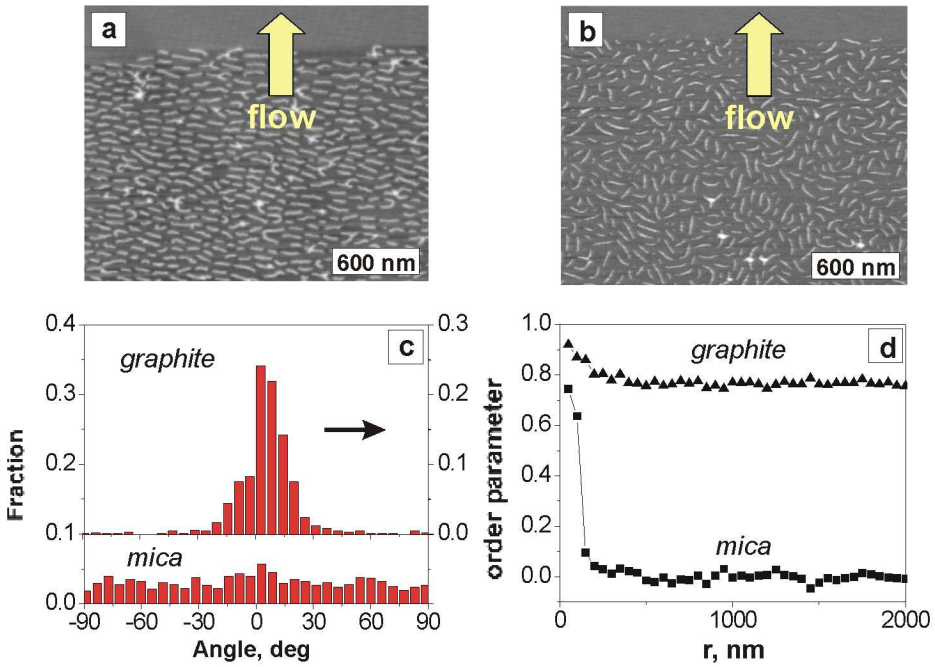

Figure 3.29: Precursor films prepared from spontaneous spreading of the comblike molecules on (a) graphite (grade A) and (b) mica. (c) On graphite, molecules show a narrow angle distribution measured relative to the horizontal axis. In contrast, molecules on mica reveal a broad (isotropic) angle distribution. (d) While the two-dimensional orientational order parameter $S = 2\langle\cos^2\theta\rangle - 1$ levels of on graphite at $S = 0.75$; it rapidly drops to zero on mica.

of a polymer melt on a solid substrate. For this purpose, we deposited a drop of the pBA brush melt to a solid substrate (mica or graphite) and monitored the spreading process by AFM. Both substrates cause spontaneous spreading of the melt resulting in a monolayer-thick precursor film which advances ahead of the macroscopic drop [118, 123, 180]. The spreading rate depends on the substrate type due to the friction between the monolayer and substrate, which in turn directly affects the length of the precursor film. It took about 10 h for the film spreading on graphite to achieve a sizable length of 10 μm while the same length on mica at a relative humidity of 95% was achieved within 10 min. The relatively slow motion on graphite allowed in situ observation of the molecular structure of the precursor film [70], whereas on mica, we performed ex-situ measurements after the spreading process was halted by reducing the relative humidity from 95% to 50%.

Figure 3.29 shows typical images of precursor films obtained on mica and graphite (grade A) surfaces, respectively. The contrast between the two images is significant. On graphite, the molecules are all aligned along a single direction (Figure 3.29a) as evidenced by a narrow angle distribution (Figure 3.29c). In stark contrast, the molecules on mica (Figure 3.29b) are completely disordered resulting in a broad distribution of angles (Figure 3.29c). The degree of order was analyzed using the orientational order parameter $S = 2\langle cos^2\theta \rangle - 1$ for two-dimensional systems, where θ is defined as the angle between each molecule and a certain director (horizontal axis in this case). As shown in Figure 3.29d, the film on graphite is characterized by a slight decay of the order parameter at short $S \approx 0.75$. In contrast, the order parameter on mica rapidly drops to $S \approx 0$ already at 100 nm, i.e., intermolecular distance, indicating a complete lack of correlation between orientations of neighboring molecules.

Next, we show that the molecular orientation does not depend on the flow direction. Figure 3.30 shows two large-scale images that give an overview of the molecular arrangement in the spreading film. Depending on the structure (perfection) of the substrate, one can either observe a large domain of molecules aligned along a single direction (Figure 3.30a) or a mosaic of smaller domains with differently oriented molecules (Figure 3.30b). Figure 3.31a-c shows three higher resolution images that are captured in different areas of the precursor film in order to demonstrate different orientations of the molecules with respect to the flow direction. The domains are visibly confined by terraces and other surface defects of the HOPG substrate. For example, the AFM image in Figure 3.31d reveals three different molecular orientations in an area of the HOPG substrate that contains several monomolecular terraces of graphite next to each other. The monomolecular origin of the terraces was confirmed with the cross-sectional profile in Figure 3.31e giving a step height of $0.32 \pm 0.05nm$ which matches with the AB interlayer spacing $c = 0.335nm$ of HOPG [177]. Note that the terraces in Figure 3.31d form native trenches or flow channels wherein molecules demonstrate different flow rates. However, we do not have enough evidences to explain the difference in flow rates, which may be due

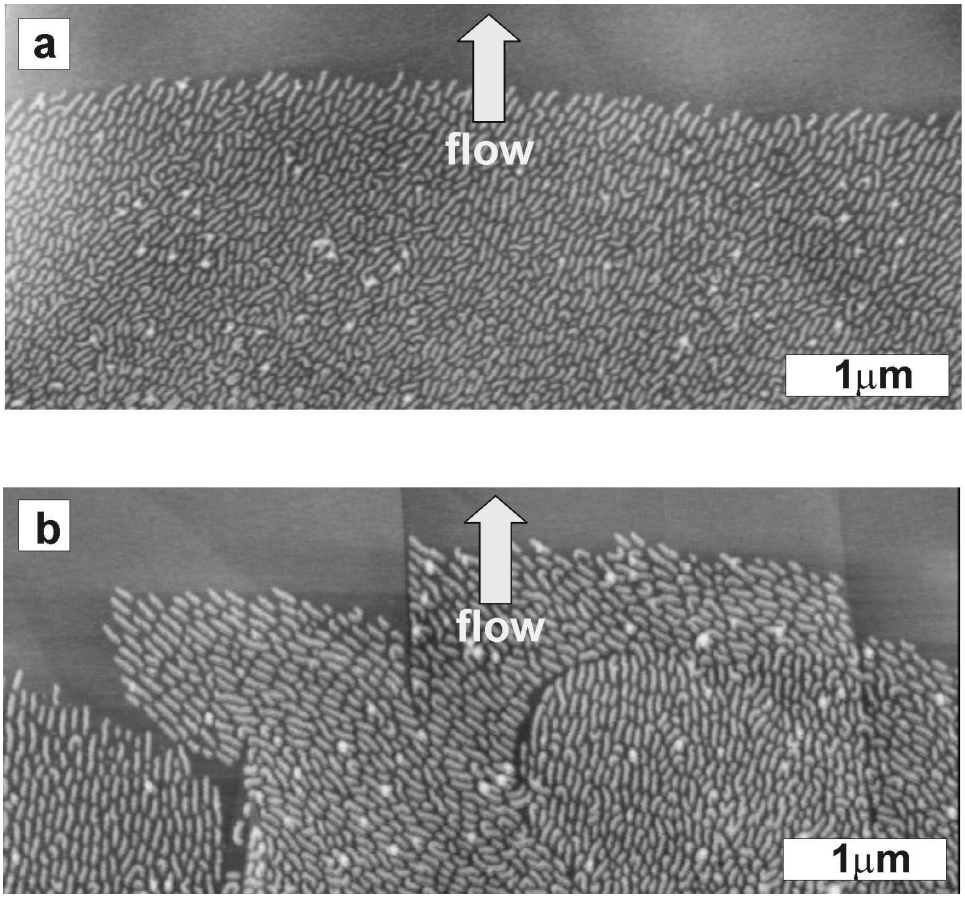

Figure 3.30: Two large-scale AFM height images demonstrate examples of different molecular organization within the flowing precursor film on graphite (grade A). Panel a shows a large domain of uniaxially oriented molecules, whereas panel b reveals a multidomain structure.

to channel confinement or to variation in friction at the substrate as expected from differently oriented molecules. This unusual flow behavior is currently under investigation.

From the AFM images one can conclude that the alignment of brush molecules is solely determined by the crystallographic lattice of the underlying substrate and independent of the flow direction. The substrate-controlled molecular orientation was confirmed by in situ monitoring of the flow process on HOPG where molecules change their orientation upon displacement over a grain boundary (Figure 3.32). The boundary, clearly seen in the phase image in Figure 3.32a (marked by the white arrow), is undetectable in the topographic image in Figure 3.32b suggesting that there is virtually no height difference between the two monocrystalline grains or mosaic blocks (see schematics in Figure 3.27a). The in situ monitoring of the flow process in this area by AFM enabled unique observation of how individual molecules abruptly shift their orientation, one molecule at a time, after crossing the grain boundary to join a new domain with a 120°- turned molecular orientation. The sharp interface between the two domains of differently oriented brush molecules exactly coincides with the grain boundary of the substrate marked by the dashed line in Figure 3.32c-f.

Flow Enhanced Molecular Diffusion The lack of correlation between the flow direction and the molecular orientation is consistent with the recently confirmed plug-flow mechanism of the mass transport in spreading monolayers of polymer brushes [70]. Unlike shear-flow, the plug-flow mechanism [181] assumes that all species move with the same velocity, i.e., with no velocity gradient which is typically responsible for the orientation of anisometric molecules and particles. Therefore, there must be another mechanism of epitaxial ordering of brushlike macromolecules associated with the flow.

Molecular epitaxy is a thermodynamic process wherein the molecules arrange themselves on the substrate lattice in order to minimize the free energy of the system [174]. Typically, in-plane diffusive translational and rotational motions facilitate molecular ordering in monomolec-

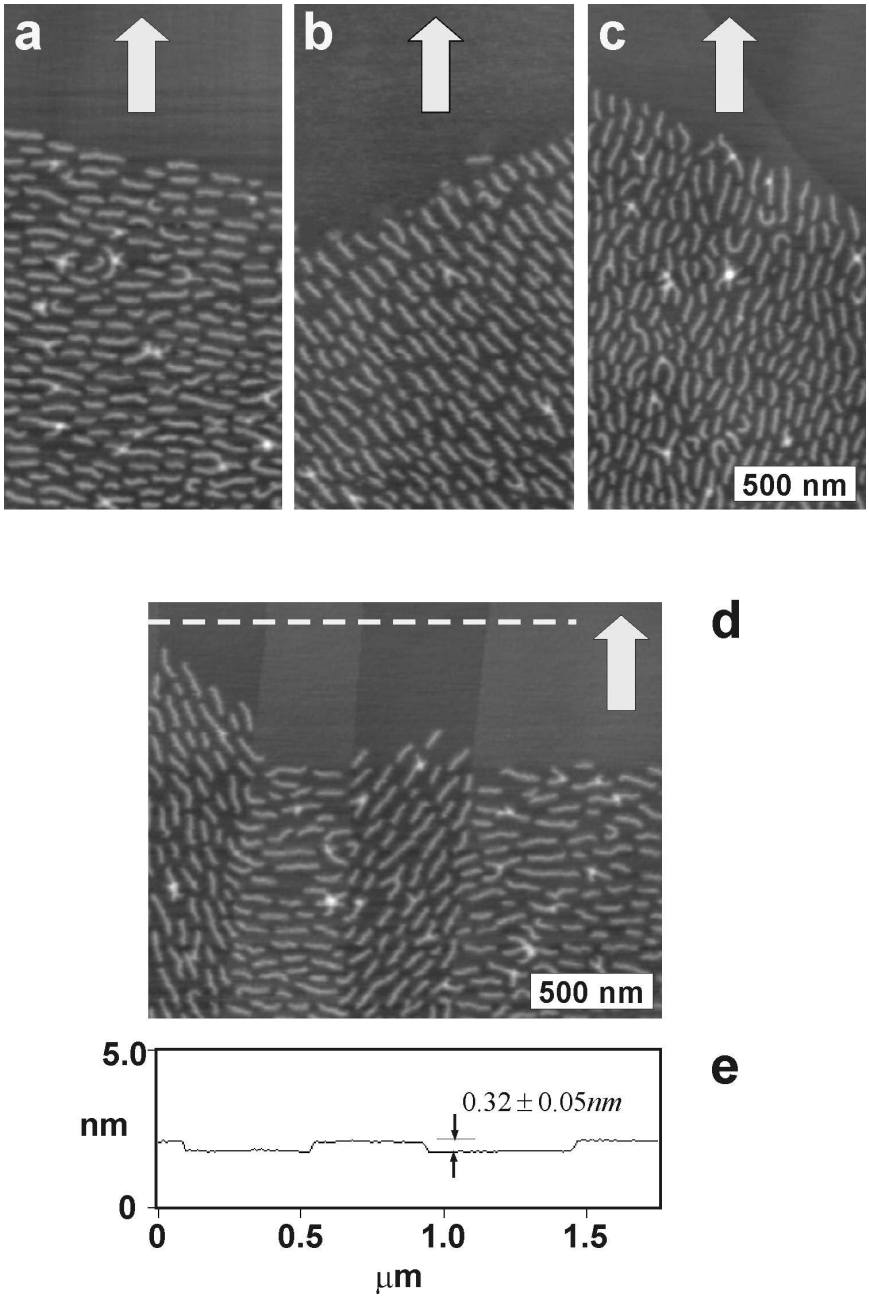

Figure 3.31: (a-d) Higher magnification height images were measured in different areas of the precursor film on graphite. The images reveal a lack of correlation between the flow direction and orientation of the flowing molecules. This behavior is clearly seen in (d) showing differently oriented domains in the same area of the precursor film. (e) From the cross-sectional profile along the dashed line in (d), one determines a terrace thickness of 0.32 ± 0.05 nm which matches with the AB interlayer spacing $c = 0.335$ nm of HOPG (see Figure 3.27a).

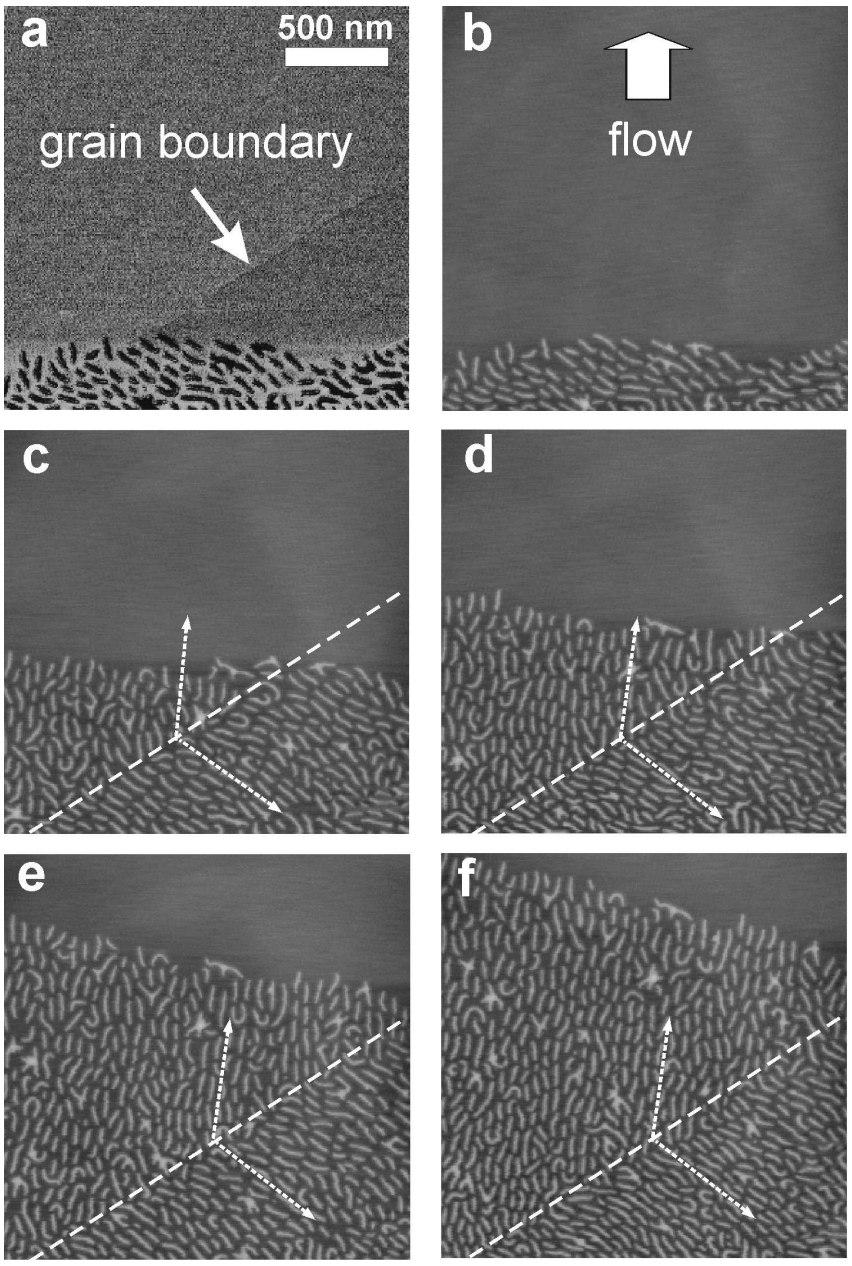

Figure 3.32: AFM was used for real-time imaging of the shift in molecular orientation upon crossing a grain boundary during spreading of pBA brushes on graphite (grade A). The micrographs (a) and (b) represent phase and height AFM images that are taken from the same sample area in order to visualize the grain boundary between two mosaic blocks (Figure 3.27a). The grain boundary shows no height contrast and becomes visible only in the phase image (white arrow). Then white dashed lines were used to highlight the grain boundary in the subsequent height images from (b) to (f). The dotted lines in images (b-f) indicate the average molecular orientation within the two domains. The angle between the directors was measured to be about 120°.

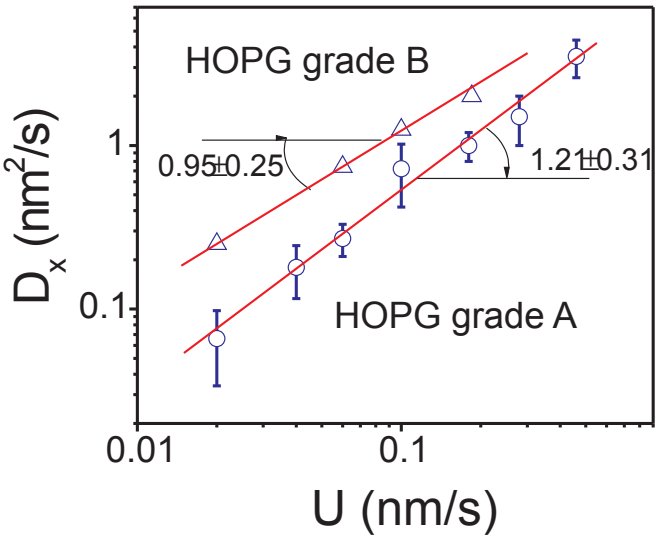

Figure 3.33: Diffusion coefficients were measured on two HOPG substrates (grade A and grade B) as a function of film spreading rate. Only the x-component of the diffusion coefficient (D_x), i.e., the diffusion in perpendicular to the flow direction, was considered to rule out the possible effects of convective diffusion. Both substrates show nearly linear increase of the diffusion coefficient with spreading rate. The lesser oriented HOPG grade B substrate shows greater diffusion than of the more oriented HOPG grade A.

ular films. However, the thermal energy is usually weak compared to the strong molecule-substrate interactions of about kT per contact between monomeric unit and substrate. Therefore, long-range ordering may not be easily achieved or takes an extremely long time. This was evidenced by the lack of long-range order in the spincast films (Figure 3.28a) even after 20 h annealing at $T = 95^{\circ}C$ which is $150^{\circ}C$ above the bulk glass transition temperature of pBA. However, mobility of surface-confined molecules may be enhanced by flow. Figure 3.33 shows that the diffusion coefficient of brush-like macromolecules within the flowing monolayer increases linearly with the flow rate. This observation on the HOPG-grade A surface confirms the previously reported linear increase of molecular diffusion on the HOPG-grade B substrate [70]. Unlike the thermal diffusion in static films, the diffusion in spreading monolayers is attributed to the flow-induced molecular diffusion. The enhanced diffusion leads to an increase in the effective kinetic energy of the molecules and thus explains why the epitaxial ordering of brush molecules was drastically expedited despite the strong molecule-substrate interactions. This

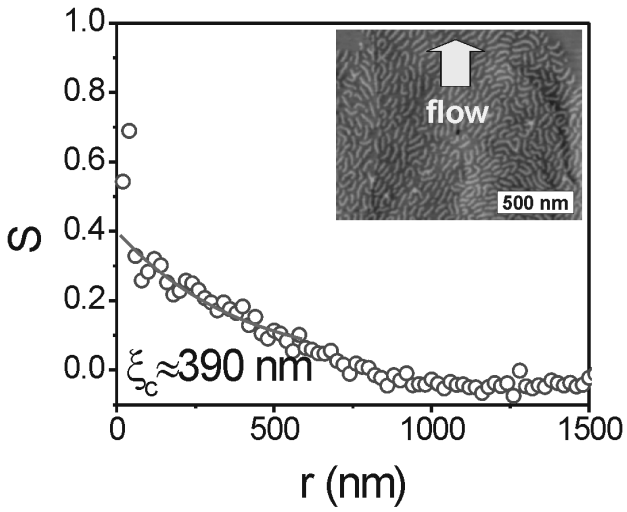

Figure 3.34: Orientation order parameter $S = 2\langle cos^2\theta\rangle - 1$ was measured as a function of intermolecular distance for a spreading monolayer of pBA brushes on HOPG grade B substrate. The inset shows a typical AFM height image of a spreading monolayer on a HOPG grade B substrate. The order parameter demonstrates an exponential decay with a correlation length of 390 nm.

is analogous to effective temperature for granular materials [182], which could be up to 100 times higher than ambient temperature.

Effect of HOPG Quality (Grade A versus Grade B) Here we compare molecular ordering and dynamics within spreading monolayers on two types of graphite substrates with different degrees of mosaic disordering. As discussed above, spreading monolayer on HOPG grade A substrate demonstrates an order parameter of 0.75 which persists over long distances beyond $10\mu m$ (Figure 3.29d). A different behavior was observed on the HOPG grade B substrate. As shown in Figure 3.34, the orientation order parameter rapidly decays to zero at a low correlation length of 390 nm (about 8 intermolecular distances). In addition, the film on the more uniform HOPG grade A was shown to spread almost two times faster than on the HOPG grade B. The difference in spreading rate can be attributed to the difference in concentration of surface defects and to the more coherent motion of molecules due to long-range ordering. As shown

in Figure 3.33, the molecular diffusion coefficient is noticeably smaller on HOPG-A than on HOPG-B [70].

Conclusions

In summary, we have demonstrated that flow facilitated the epitaxial ordering of brush-like macromolecules on graphite, resulting in a long-range orientational order. The brush-like architecture leads to a length-scale enhancement effect as the epitaxial adsorption of the short side chains causes alignment of giant macromolecules. The increase in the degree of orientational order is attributed to the flow-enhanced diffusion of molecules, which enables them to find an energetically favorable arrangement. Our findings suggest that convective flow is more efficient than thermal motion in improving ordering of large molecular and colloidal species. This may result in new techniques for fabricating long-range ordered structures on surface.

Bibliography

[1] H. Staudinger, *Die hochmolekularen organischen Verbindugen*, Springer Verlag, Berlin, 1932.

[2] J. P. Flory, *Statistical mechanics of Chain Molecules*, Interscience, New York, 1969.

[3] J. P. Flory, J. Chem. Phys. **17**, 303 (1949).

[4] S. F. Edwards, Proc. Phys. Soc. **85**, 613 (1964).

[5] M. A. Moore, J. Phys. A **10**, 305 (1977).

[6] O. B. Ptitsyn and Y. E. Eizner, Biofizika **10**, 3 (1965).

[7] P. G. de Gennes, Journalle de Physique (Paris) Lett. **36**, L55 (1975).

[8] I. M. Lifshitz, A. Y. Grosberg, and A. R. Khokhlov, Rev. Mod. Phys. **50**, 683 (1978).

[9] T. M. Birshtein and V. Pryamitsyn, Vysokomol. Soedin. **29**, 1858 (1987).

[10] H. Yamakawa, *Modern Theory of Polymer Solutions*, Harpers Chemistry Series, Harper and Row, New York, 1971.

[11] J. des Cloizeaux and G. Jannink, *Polymers in Solution*, Clarendon press, Oxford, 1990.

[12] A. L. Kholodenko and K. F. Freed, J. Chem. Phys. **80**, 900 (1984).

[13] B. J. Cherayil, J. F. Douglas, and K. F. Freed, J. Chem. Phys. **8**, 5293 (1985).

[14] B. Duplantier, J. Chem. Phys. **86**, 4233 (1987).

[15] A. Brulet, F. Boue, and J. P. Cotton, Journal de Physique II **6**, 885 (1996).

[16] A. V. Dobrynin, Macromolecules **38**, 9304 (2005).

[17] S. Lecommandoux, F. Checot, R. Borsali, M. Schappacher, A. Deffieux, A. Brulet, and J. P. Cotton, Macromolecules **35**, 8878 (2002).

[18] C. Rivetti, C. Walker, and C. Bustamante, Journal of Molecular Biology **280**, 41 (1998).

[19] S. S. Sheiko, F. C. Sun, A. Randall, D. Shirvanyants, M. Rubinstein, H.-i. Lee, and K. Matyjaszewski, Nature **440**, 191 (2006).

[20] J. P. Wittmer, H. Meyer, J. Baschnagel, A. Johner, S. Obukhov, L. Mattioni, M. Muller, and A. N. Semenov, Phys. Rev. Lett. **93**, 147801 (2004).

[21] P. G. de Gennes, *Scaling concepts in polymer physics*, Cornell University, Ithaka, 1979.

[22] G. Allegra, Macromolecules **16**, 555 (1983).

[23] A. R. Khokhlov, Polymer **19**, 1387 (1978).

[24] Zimm, Stockmayer, and Fixman, J. Chem. Phys. **21**, 1716 (1953).

[25] H. Yamakawa, A. Aoki, and G. Tanaka, J. Chem. Phys. **45**, 1938 (1966).

[26] I. M. Withers, A. V. Dobrynin, M. L. Berkowitz, and M. Rubinstein, J. Chem. Phys. **118**, 4721 (2003).

[27] J. Shimada and H. Yamakawa, Macromolecules **17**, 689 (1984).

[28] A. Dua and B. J. Cherayil, J. Chem. Phys. **117**, 7765 (2002).

[29] J.-F. Allemand, S. Cocco, N. Douarche, and G. Lia, Eur. Phys. J. E **19**, 293 (2006).

[30] L. Landau and E. Lifshitz, *Theory of elasticity*, Oxford [Oxfordshire], Pergamon Press, New York, 3rd english ed. edition, 1986.

[31] T. Odijk, Macromolecules **12**, 688 (1979).

[32] A. V. Dobrynin, R. H. Colby, and M. Rubinstein, Macromolecules **28**, 1859 (1995).

[33] L. Qi, A. V. Dobrynin, and M. Rubinstein, Macromolecules **36**, 3386 (2003).

[34] I. Webman, J. L. Lebowitz, and M. H. Kalos, Macromolecules **14**, 1495 (1981).

[35] K. Kremer, A. Baumgartner, and K. Binder, J. Phys. A **15**, 2879 (1982).

[36] H. Meirovitch and H. A. Lim, J. Chem. Phys. **91**, 2544 (1989).

[37] H. Meirovitch and H. A. Lim, J. Chem. Phys. **92**, 5144 (1990).

[38] X.-F. Yuan and A. J. Masters, J. Chem. Phys. **94**, 6908 (1991).

[39] A. Rey, J. J. Freire, M. Bishop, and J. H. R. Clarke, Macromolecules **25**, 1311 (1992).

[40] A. M. Rubio, J. J. Freire, J. H. R. Clarke, C. W. Yong, and M. Bishop, J. Chem. Phys. **102**, 2277 (1995).

[41] M. Wittkop, S. Kreitmeier, and D. Goritz, J. Chem. Phys. **104**, 3373 (1996).

[42] M. Rubinstein and R. H. Colby, *Polymer physics*, Oxford University Press, New York, 2003.

[43] W. L. Mattice, C. A. Helfer, and A. P. Sokolov, Macromolecules **36**, 9924 (2003).

[44] T. Konishi, T. Yoshizaki, T. Saito, Y. Einaga, and H. Yamakawa, Macromolecules **23**, 290 (1990).

[45] E. Ficarra, L. Benini, E. Macii, and G. Zuccheri, IEEE Transactions on Information Technology in Biomedicine **9**, 508 (2005).

[46] D. B. West, *Introduction to graph theory*, Upper Saddle River, NJ : Prentice Hall, 1996.

[47] T. H. Cormen, C. E. Leiserson, R. L. Rivest, and C. Stein, *Introduction to Algorithms*, MIT Press and McGraw-Hill, 2nd edition, 2001.

[48] E. W. Dijkstra, Numerische Mathematik **1**, 269 (1959).

[49] L. Dorst and A. W. M. Smeulders, Computer Vision Graphics And Image Processing **40**, 311 (1987).

[50] C. Rivetti and S. Codeluppi, Ultramicroscopy **87**, 55 (2001).

[51] W. H. Press, B. P. Flannery, S. A. Teukolsky, and W. T. Vetterling, *Numerical recipes: the art of scientific computing*, Cambridge University Press New York, NY, USA, 1986.

[52] S. S. Sheiko and M. Möller, Chem. Rev. **101**, 4099 (2001).

[53] S. S. Sheiko, M. da Silva, D. Shirvaniants, I. LaRue, S. Prokhorova, M. Moeller, K. Beers, and K. Matyjaszewski, J. Am. Chem. Soc. **125**, 6725 (2003).

[54] S. S. Sheiko, S. A. Prokhorova, K. L. Beers, K. Matyjaszewski, I. I. Potemkin, A. R. Khokhlov, and M. Möller, Macromolecules **34**, 8354 (2001).

[55] H. G. Börner, K. Beers, K. Matyjaszewski, S. S. Sheiko, and M. Möller, Macromolecules **34**, 4375 (2001).

[56] C. Rivetti, M. Guthold, and C. Bustamante, J. Mol. Biol. **264**, 919 (1996).

[57] J. Kumaki, Y. Nishikawa, and T. Hashimoto, J.Am.Chem.Soc. **11**, 3321 (1996).

[58] S. A. Prokhorova, S. S. Sheiko, M. Möller, C.-H. Ahn, and V. Percec, Macromol. Rapid Comm. **19**, 359 (1998).

[59] B. Maier and J. O. Rädler, Phys.Rev.Lett. **82**, 1911 (1999).

[60] T. A. Camesano and K. J. Wilkinson, Biomacromolecules **2**, 1184 (2001).

[61] S. Minko, A. Kiriy, G. Gorodyska, and M. Stamm, J.Am.Chem.Soc. **124**, 3218 (2002).

[62] P. G. De Gennes, Journal Of Polymer Science Part C-Polymer Symposium , 313 (1977).

[63] R. G. Kirste and B. R. Lehnen, Makromolekulare Chemie-Macromolecular Chemistry And Physics **177**, 1137 (1976).

[64] M. R. Landry, Macromolecules **30**, 7500 (1997).

[65] C. Tangari, R. Ullman, J. S. King, and G. D. Wignall, Macromolecules **23**, 5266 (1990).

[66] N. Torikai, N. Takabayashi, I. Noda, J. Suzuki, and Y. Matsushita, Journal Of Physics And Chemistry Of Solids **60**, 1325 (1999).

[67] A. C. Balazs, T. Emrick, and T. P. Russell, Science **314**, 1107 (2006).

[68] M. E. Mackay, A. Tuteja, P. M. Duxbury, C. J. Hawker, B. Van Horn, Z. B. Guan, G. H. Chen, and R. S. Krishnan, Science **311**, 1740 (2006).

[69] S. W. Sides, B. J. Kim, E. J. Kramer, and G. H. Fredrickson, Physical Review Letters **96**, 250601 (2006).

[70] H. Xu, D. Shirvanyants, K. Beers, K. Matyjaszewski, M. Rubinstein, and S. S. Sheiko, Physical Review Letters **93**, 206103 (2004).

[71] H. Xu, D. Shirvanyants, K. L. Beers, K. Matyjaszewski, A. V. Dobrynin, M. Rubinstein, and S. S. Sheiko, Physical Review Letters **94**, 237801 (2005).

[72] K. Matyjaszewski and J. Xia, Chem. Rev. **101**, 2921 (2001).

[73] I. I. Potemkin, Macromolecules **39**, 7178 (2006).

[74] G. R. Newkome, E. He, and C. N. Moorefield, Chem.Rev. **99**, 1689 (1999).

[75] J. M. J. Fréchet, J. Polym. Sci., Polym. Chem. **41**, 3713 (2003).

[76] P. Dvornic and D. Tomalia, Current Opinion In Colloid & Interface Science **1**, 221 (1996).

[77] M. Gauthier and M. Möller, Macromolecules **24**, 4548 (1991).

[78] J.-L. Six and Y. Gnanou, Macromolecular Simposia **95**, 137 (1995).

[79] M. Gauthier, J. Li, and J. Dockendorff, Macromolecules **36**, 2642 (2003).

[80] V. Percec and M. N. Holerca, Biomacromolecules **1**, 6 (2000).

[81] V. Percec et al., J.Am.Chem.Soc. **120**, 8619 (1998).

[82] Y. Tsukahara, K. Tsutsumi, Y. Yamashita, and S. Shimada, Macromolecules **23**, 5201 (1990).

[83] M. W. Neiser, J. Okuda, and M. Schmidt, Macromolecules **36**, 5437 (2003).

[84] G. Cheng, A. Böker, M. Zhang, G. Krausch, and A. H. E. Müller, Macromolecules **34**, 6883 (2001).

[85] K. L. Beers, S. G. Gaynor, K. Matyjaszewski, S. S. Sheiko, and M. Möller, Macromolecules **31**, 9413 (1998).

[86] K. Matyjaszewski, S. H. Qin, J. R. Boyce, D. Shirvanyants, and S. S. Sheiko, Macromolecules **36**, 1843 (2003).

[87] J. R. Boyce, D. Shirvanyants, S. S. Sheiko, D. A. Ivanov, S. Qin, H. Börner, and K. Matyjaszewski, Langmuir **20**, 6005 (2004).

[88] M. Netopilík and P. Kratochvíl, Polymer **44**, 3431 (2003).

[89] G. V. Schulz, Z. physik. Chem. **B43**, 25 (1939).

[90] J. R. Schaefgen and P. J. Flory, Journal of the American Chemical Society **70**, 2709 (1948).

[91] C. Basire and D. A. Ivanov, Phys. Rev. Lett. **85**, 5587 (2000).

[92] D. R. Nelson, M. Rubinstein, and F. Spaepen, Philosophical Magazine A: Physics of Condensed Matter: Structure, Defects and Mechanical Properties **46**, 105 (1982).

[93] M.-C. Cha and H. A. Fertig, Phys. Rev. B **50**, 14368 (1994).

[94] P. Chaikin and T. Lubensky, *Principles of Condensed Matter Physics*, University Press: Cambridge, 1995.

[95] L. Santen and W. Krauth, Los Alamos National Laboratory, Preprint Archive, Condensed Matter , 1 (2001).

[96] D. A. Kofke and P. G. Bolhuis, Phys. Rev. E **59**, 618 (1999).

[97] P. Bartlett, The Journal of Chemical Physics **109**, 10970 (1998).

[98] J. E. Field, Inst. Phys. Conf. Ser. **75**, 181?205 (1986).

[99] A. Derrington, The Financial Times **n33034**, section 3, pWFT2(1) (13/14 July 1996).

[100] P. Smith and P. J. Lemstra, J. Polym. Sci. Polym. Phys. Ed. **19**, 1007 (1981).

[101] T. Porter, R. S. & Kanamoto, Polym. Eng. Sci. **34**, 266?268 (1994).

[102] J.-P. Salvetat, G. A. D. Briggs, J.-M. Bonard, R. R. Bacsa, A. J. Kulik, T. Stöckli, N. A. Burnham, and L. Forró, Phys. Rev. Lett. **82**, 944 (1999).

[103] M.-F. Yu, B. S. Files, S. Arepalli, and R. S. Ruoff, Phys. Rev. Lett. **84**, 5552 (2000).

[104] P. . G. de Gennes, Journal of Chemical Physics **60**, 5030 (1974).

[105] R. E. Harrington and B. H. Zimm, J. Phys. Chem. **69**, 161 (1965).

[106] J. A. Odell, A. Keller, and Y. Rabin, J. Chem. Phys. **88**, 4022?4028 (1988).

[107] A. M. Basedow and K. H. Ebert, Adv. Polym. Sci. **22**, 83 (1977).

[108] A. Bensimon, A. Simon, A. Chiffaudel, V. Croquette, F. Heslot, and D. Bensimon, Science **265**, 2096 (1994).

[109] A. Kishino and T. Yanagida, Nature **334**, 74 (1988).

[110] E. Evans, Annu. Rev. Biophys. Biomol. Struct. **30**, 105 (2001).

[111] S. B. Smith, Y. Cui, and C. Bustamante, Science **271**, 795?799 (1996).

[112] P. Cluzel, A. Lebrun, C. Heller, R. Lavery, J.-L. Viovy, D. Chatenay, and F. Caron, Science **271**, 792 (1996).

[113] A. D. Mehta, M. Rief, J. A. Spudich, D. A. Smith, and R. M. Simmons, Science **283**, 1689?1695 (1999).

[114] F. Sun, S. S. Sheiko, M. Möller, K. Beers, and K. Matyjaszewski, J. Phys. Chem. A **108**, 9682?9686 (2004).

[115] D. Neugebauer, B. S. Sumerlin, K. Matyjaszewski, B. Goodhart, and S. S. Sheiko, Polymer **45**, 8173 (2004).

[116] R. H. Austin, J. P. Brody, E. C. Cox, T. Duke, and W. Volkmuth, Physics Today **50**, 32 (1997).

[117] D. Boris and M. Rubinstein, Macromolecules **29**, 7251 (1996).

[118] P. G. de Gennes, Rev. Mod. Phys. **57**, 827 (1985).

[119] A.-M. Cazabat, Contemporary Physics **28**, 347 (1987).

[120] A. M. Cazabat, N. Fraysse, F. Heslot, and P. Carles, J. Phys. Chem. **94**, 7581 (1990).

[121] M. Voue and J. De Coninck, Acta Materialia **48**, 4405 (2000).

[122] R. Bruinsma, Macromolecules **23**, 276 (1990).

[123] W. B. Hardy, Philosophical Magazine (1798-1977) **38**, 49 (1919).

[124] P. G. de Gennes and A. M. Cazabat, Lecture Notes in Physics **386**, 33 (1991).

[125] F. Heslot, A. M. Cazabat, and P. Levinson, Physical Review Letters **62**, 1286 (1989).

[126] T. E. Karis and G. W. Tyndall, Journal of Non-Newtonian Fluid Mechanics **82**, 287 (1999).

[127] X. Ma, J. Gui, L. Smoliar, K. Grannen, B. Marchon, C. L. Bauer, and M. S. Jhon, Phys. Rev. E **59**, 722 (1999).

[128] D. Ausserré, A. M. Picard, and L. Léger, Phys. Rev. Lett. **57**, 2671 (1986).

[129] V. Percec, C.-H. Ahn, G. Ungar, D. J. P. Yeardley, M. Moller, and S. S. Sheiko, Nature (London) **391**, 161 (1998).

[130] T. Hashimoto, A. Okumura, and D. Tanabe, Macromolecules **36**, 7324 (2003).

[131] S. Villette, M. P. Valignat, A. M. Cazabat, F. A. Schabert, and A. Kalachev, Physica A: Statistical and Theoretical Physics (Amsterdam) **236**, 123 (1997).

[132] D. Glick, P. Thiansathaporn, and R. Superfine, Applied Physics Letters **71**, 3513 (1997).

[133] J. Israelachvili, *Intermolecular and Surface Forces*, Academic Press, San Diego, CA, 2nd edition, 1992.

[134] H. M. Jaeger, S. R. Nagel, and R. P. Behringer, Rev. Mod. Phys. **68**, 1259 (1996).

[135] H. A. Makse and J. Kurchan, Nature (London, United Kingdom) **415**, 614 (2002).

[136] G. D'Anna, P. Mayor, A. Barrat, V. Loreto, and F. Nori, Nature (London, United Kingdom) **424**, 909 (2003).

[137] C. M. Mate and B. Marchon, Phys. Rev. Lett. **85**, 3902 (2000).

[138] S. Y. Chou, M. S. Wei, P. R. Krauss, and P. B. Fischer, The 6th joint magnetism and magnetic materials (MMM)-intermag conference **76**, 6673 (1994).

[139] R. R. Li, P. D. Dapkus, M. E. Thompson, W. G. Jeong, C. Harrison, P. M. Chaikin, R. A. Register, and D. H. Adamson, Applied Physics Letters **76**, 1689 (2000).

[140] W. Volkmuth and R. Austin, Nature **358**, 600 (1992).

[141] M. O'Neill and S. M. Kelly, Journal of Physics D: Applied Physics **33**, R67 (2000).

[142] K. Jain, M. Zemel, and M. Klosner, Proceedings of the IEEE **90**, 1681 (2002).

[143] J. L. Wilbur, A. Kumar, E. Kim, and G. M. Whitesides, Advanced Materials **6**, 600 (1994).

[144] E. Schäffer, T. Thurn-Albrecht, T. Russell, and U. Steiner, Nature **403**, 874 (2000).

[145] T. Morkved, M. Lu, A. Urbas, E. Ehrichs, H. Jaeger, P. Mansky, and T. Russell, Science **273**, 931 (1996).

[146] E. Huang, L. Rockford, T. Russell, and C. Hawker, Nature **395**, 757 (1998).

[147] J. Bodycomb, Y. Funaki, K. Kimishima, and T. Hashimoto, Macromolecules **32**, 2075 (1999).

[148] T. Thurn-Albrecht, J. Schotter, C. Kastle, N. Emley, T. Shibauchi, L. Krusin-Elbaum, K. Guarini, C. Black, M. Tuominen, and T. Russell, Science **290**, 2126 (2000).

[149] C. Harrison, D. Adamson, Z. Cheng, J. Sebastian, S. Sethuraman, D. Huse, R. Register, and P. Chaikin, Science **290**, 1558 (2000).

[150] W. Lopes and H. Jaeger, Nature **414**, 735 (2001).

[151] N. Denkov, O. Velev, P. Kralchevsky, I. Ivanov, H. Yoshimura, and K. Nagayama, Nature **361**, 26 (1993).

[152] R. Micheletto, H. Fukuda, and M. Ohtsu, Langmuir **11**, 3333 (1995).

[153] B. Prevo and O. Velev, Langmuir **20**, 2099 (2004).

[154] R. Segalman, H. Yokoyama, and E. Kramer, Advanced Materials **13**, 1152 (2001).

[155] R. Segalman, A. Hexemer, and E. Kramer, Physical Review Letters **91**, 196101 (2003).

[156] R. Segalman, Materials Science & Engineering R-Reports **48**, 191 (2005).

[157] J. Hahn and S. Webber, Langmuir **20**, 1489 (2004).

[158] D. Sundrani, S. Darling, and S. Sibener, Langmuir **20**, 5091 (2004).

[159] H. Li and W. Huck, Nano Letters **4**, 1633 (2004).

[160] J. Cheng, A. Mayes, and C. Ross, Nature Materials **3**, 823 (2004).

[161] J. W. Matthews, editor, *Epitaxial Growth*, Academic Press: New York,, 1975.

[162] S. O. Kim, H. H. Solak, M. P. Stoykovich, N. J. Ferrier, J. J. de Pablo, and P. F. Nealey, Nature **424**, 411 (2003).

[163] V. A. Shchukin, N. N. Ledentsov, and D. Bimberg, *Epitaxy of nanostructures*, Springer: Berlin, 2004.

[164] C. De Rosa, C. Park, E. L. Thomas, and B. Lotz, Nature **405**, 433 (2000).

[165] N. Severin, J. P. Rabe, and D. G. Kurth, Journal of the American Chemical Society **126**, 3696 (2004).

[166] T. Maruyama, M. Friedenberg, G. G. Fuller, C. W. Frank, C. R. Robertson, A. Ferencz, and G. Wegner, THIN SOLID FILMS **273**, 76 (1996).

[167] X. Michalet, R. Ekong, F. Fougerousse, S. Rousseaux, C. Schurra, N. Hornigold, M. vanSlegtenhorst, J. Wolfe, S. Povey, J. S. Beckmann, and A. Bensimon, Science **277**, 1518 (1997).

[168] R. Djalali, S. Y. Li, and M. Schmidt, Macromolecules **35**, 4282 (2002).

[169] M. Schappacher and A. Deffieux, Macromolecules **33**, 7371 (2000).

[170] O. Ikkala and G. ten Brinke, Chemical Communications , 2131 (2004).

[171] J. Mijović, M. Y. Sun, and S. Pejanović, Macromolecules **36**, 7640 (2003).

[172] S. Jha, S. Dutta, and N. B. Bowden, Macromolecules **37**, 4365 (2004).

[173] A. F. Zhang, J. Barner, I. Goessl, J. P. Rabe, and A. D. Schluter, Angewandte Chemie-International Edition **43**, 5185 (2004).

[174] D. E. Hooks, T. Fritz, and M. D. Ward, Advanced Materials **13**, 227 (2001).

[175] M. Ohler, J. Baruchel, and P. Galez, Journal Of Physics D-Applied Physics **28**, A78 (1995).

[176] S. Sheiko, M. Möller, E. Reuvekamp, and H. Zandbergen, Physical Review B (Condensed Matter) **48**, 5675 (1993).

[177] N. J. Wu and A. Ignatiev, Physical Review B (Condensed Matter) **25**, 2983 (1982).

[178] S. A. Prokhorova, S. S. Sheiko, A. Mourran, R. Azumi, U. Beginn, G. Zipp, C.-H. Ahn, M. N. Holerca, V. Percec, and M. Mller, Langmuir **16**, 6868 (2000).

[179] J. Hu, X.-D. Xiao, D. F. Ogletree, and M. Salmeron, Science **268**, 267 (1995).

[180] F. Heslot, N. Fraysse, and A. M. Cazabat, Nature **338**, 640 (1989).

[181] F. Brochard and P. . G. de Gennes, Journal de Physique Lettres **45**, L597 (1984).

[182] I. Ono, C. O'Hern, D. Durian, S. Langer, A. Liu, and S. R. Nagel, Physical Review Letters **89**, 095703/1 (2002).